Frustration and Disorder: Classical Spin Liquids and Floquet-Anderson Insulators

Dillon T. Liu

Somerville College

University of Oxford

A thesis submitted for the degree of

Doctor of Philosophy

Trinity Term 2017

Abstract

In this thesis, the physics of two systems is investigated, both of which support unconventional phases of matter. We investigate a frustrated system which has a classical spin liquid regime in the paramagnetic phase. We also consider a periodically-driven, disordered system and explore non-equilibrium regimes. Both systems exhibit macroscopic behaviour which differs strongly from the behaviour in standard scenarios.

First, the properties of frustrated magnets and related systems are discussed. We introduce three-dimensional generalisations of a well-studied two-dimensional frustrated system. These generalisations consist of coupled layers of two-dimensional triangular lattice Ising antiferromagnets. We study three stackings that have nearest-neighbour interactions: two frustrated stackings (abc and abab) and the unfrustrated stacking (aaa). We use a combination of methods, including numerics and analytics, to show that these generalisations exhibit a strongly correlated, highly fluctuating regime known as a classical spin liquid. We show this by investigating the structure factor and correlations directly and by describing a mapping to a continuum field theory that gives further clarity about the classical spin liquid regime using a renormalisation group analysis and consideration of low-lying excitations in these systems.

Second, we study the response of a disordered system to a time-periodic driving potential. We start in the context of Mott's work on a.c. conductivity in Anderson insulators and move beyond this to study the Floquet (long-time) regimes beyond linear response. Using Landau-Zener physics, we construct a description of the various regimes which are possible. We also present the results of thorough numerical studies of these systems.

Acknowledgements

I am thankful for everything that my supervisor, John Chalker, has done for me over the past four years. Of course, this includes immense contributions to the research I present in this thesis and all of my work at Oxford. His insights and perspectives on physics and problem solving have set a high bar that I aspire to meet.

I am also grateful for the camaraderie of my fellow students. Thanks to Thomas Veness, Richard Fern, Stefan Groha, Bruno Bertini, Gábor Halász, Fenner Harper, Curt von Keyserlingk, Neil Robinson, Thomas Scaffidi, Amos Chan, Jack Kemp, and Abi Kulshreshtha.

Thanks to other department members, including Adam Nahum, Arijeet Pal, Zohar Ringel, Stefanie Thiem, and especially Dima Kovrizhin for reading a draft of this thesis. Fabian Essler, Paul Fendley, and Steve Simon are due thanks for wise advice. I am also thankful for mentors I had as an undergraduate: Rahul Roy, Tom Intrator, Brian Greene, Max Lipyanskiy, and John DiTusa.

Of course, I deeply appreciate the Marshall Aid Commemoration Commission, Somerville College, and the Department of Theoretical Physics for funding me and the Kavli Institute for Theoretical Physics for hosting me during Autumn 2015.

I am grateful for support I received outside of physics as well. Thanks to SCBC for putting me in a boat and to OULRC for showing me how to move one. Contending with an ocean of separation from friends and family in the US was not always easy, but visits and trips made that bearable. I am also very thankful for the friendships I have forged while in the UK. Finally, I will always owe my siblings and parents for their love and support.

Author Contributions

The work presented in this thesis is based on a publication [1] and a manuscript currently in preparation [2].

The author of this thesis contributed critically to [1] via the extensive Monte Carlo simulations and the development of the self-consistent Gaussian approximation treatment in that work. This included writing the full parallel tempering Metropolis Monte Carlo simulations and carrying out all of the data analysis for the results of those simulations. Additionally, some independent numerical simulations were carried out by L. D. C. Jaubert and used to corroborate results in Chapter 5.

[1] contains work which was principally contributed by F. J. Burnell and J. T. Chalker (see also [3]), but which is included in this thesis in Chapters 6, 7. These results are included in detail in this thesis because they provide essential context for the problem on which Part II focuses.

Part III also contains work from a collaboration with V. Khemani, S. L. Sondhi, and J. T. Chalker [2]. The author of this thesis carried out essentially all the numerical work in this project and made significant contributions to identifying the appropriate physical properties of the systems and their signatures in the numerical simulations.

Contents

Part I

Introduction

Chapter 1

Overview and Outline

The figurative condensed matter physics diaspora, rooted in the study of solids and liquids, is now widely spread across far more exotic matter. The core principle remains understanding how macroscopic properties emerge from simple models. In this thesis, we use statistical physics, electromagnetism, and quantum mechanics to study two examples of exotic matter. The presence of microscopic wrinkles in our simple models gives rise to the distinctive properties of these systems. The wrinkles are, respectively, frustration and disorder. While the colloquial meanings of these words belie the deeper nuances, their usage is in good faith.

In condensed matter physics, a primary focus is developing a framework to distinguish different kinds of matter, or phases. Huge amounts of effort have been spent trying to understand, in a precise way, the manner in which types of matter differ from each other. Symmetry and topology play key roles here and, over the past century, have provided an impressively thorough framework for classifying phases of matter in equilibrium. However, we will see that it is also fruitful to think beyond the usual paradigm and investigate regimes within definite phases of matter or regimes in non-equilibrium situations. In the case of the former, we will see that it is possible to have dramatically different behaviour within a single phase of matter and in the case of the latter, we will see that some systems have distinctive non-equilibrium regimes and crossovers between these regimes.

In the frustrated and disordered systems we study, the essential physics of these regimes is difficult to capture by considering only individual particles. Instead, one must appeal to other methods. Many conceptual and practical developments have

been crucial to any success we have had in describing frustrated or disordered systems. Chief among these are two different approaches that provide insight to increasingly large systems. One of these is the idea of scale invariance and the other is the continued increase in computational power available. The latter is an example of how condensed matter physics is the gift that keeps on giving: solid state and semiconductor physics gave rise to the transistor in the first half of the 20th century and the technological advances that followed have opened vast avenues of research into ever more sophisticated systems. The idea of scaling was developed more recently and provides a theoretical apparatus to describe physics of condensed matter systems at increasing length scales.

Although the work here is theoretical, the importance of experiments in condensed matter physics cannot be understated. A blessing of condensed matter physics is the robust and frequent feedback between theoreticians and experimentalists. While highly sophisticated, the manageable scale of experiments in condensed matter physics means that analytic and numerical progress is mostly anchored in reality.

In Part II, we present a study of three-dimensional geometrically frustrated magnets. We give a brief, broad overview of frustrated magnetism in Chapter 2 to introduce the topic. In the rest of Part II, we specifically study systems of stacked triangular lattice Ising antiferromagnets and unconventional phases of matter that arise therein.

In Part III, we study driven Anderson insulators, or Floquet-Anderson insulators. We begin in Chapter 9 by giving some background about the kind of disordered systems we study and introduce other tools used for studying periodically driven quantum systems. Within the remainder of Part III, we study Anderson insulators in the strongly-localised regime and with periodic, monochromatic drives and the dynamical regimes that develop in these systems.

Part II

Frustration

Chapter 2

Frustrated Magnetism

Frustrated systems are those which cannot minimise, simultaneously, the interaction energy between degrees of freedom; the interactions are said to be competing. Frustration can arise in a number of scenarios, but to start, we consider it in the context of magnetism and degrees of freedom which are magnetic moments or spins.

In the rest of this chapter, we give a broad overview of frustrated magnetism. We discuss two types of frustration which exist, some general properties of frustrated systems, and give a detailed outline of the rest of Part II.

2.1 Types of Frustration

Broadly, frustration can originate in two systematic ways. One of these is through geometrical means and the other is through randomness [4]. In the latter, the couplings between degrees of freedom are random for some reason and this leads to competition. In Fig. 2.1, we show an example of how a particular configuration of couplings can lead to competition between interactions that cannot be resolved. This type of frustration is highly relevant in materials called spin glasses. Spin glasses are an enormous field of study in their own right and we will not consider them here.

The other systematic way in which frustration can arise is through the geometry of a system. This is known as geometrical frustration and the frustration we study in this thesis has geometric origins. We start with two examples of geometric frustration and then explain why we focus on one of them.

For the first example, consider four classical Ising spins on the corners of a square,

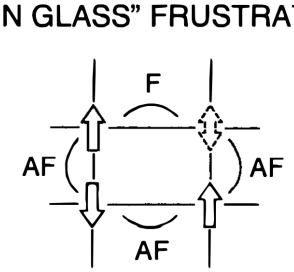

Figure 2.1: Figure from [4]. In the configuration of couplings shown here (F is ferromagnetic, AF is antiferromagnetic), no configuration can satisfy all the interactions.

as seen in Fig. 2.2 [5]. Let these spins interact with an antiferromagnetic nearest-neighbour coupling, J, and a next-nearest-neighbour coupling, J'. When J' is not present, the Néel pattern of spins (shown in Fig. 2.2) is preferred. However, for non-vanishing J', the situation is not as simple. When we move to a square lattice instead of a single square, when $J = 2J'$, the interactions are completely frustrated. Now there are many different configurations which have the same lowest energy. In particular, the Néel pattern of alternating spins has the same energy as any configuration which has net zero spin on the squares. These configurations satisfy the next-nearest-neighbour couplings at the expense of the nearest-neighbour ones. This degeneracy depends on the ratio of J'/J; when $J > 2J'$, the Néel pattern is preferred and when $J < 2J'$, the pattern favouring anti-aligned next-nearest-neighbours is preferred.

The second example is shown on the right in Fig. 2.2. Here we have classical Ising spins interacting with an antiferromagnetic coupling. Obviously when this is the case, there is no way to satisfy all three bonds simultaneously. Consequently, there are six different symmetry-related configurations that have the same energy. The degeneracy in this case is not dependent on the specific values of the couplings, only that they are all equal.

We focus on the second type of geometrically frustrated magnet. One reason for focusing on these is that they are more likely to be relevant for physical systems. Because the $J - J'$ example depends on the ratio J'/J being precisely $\frac{1}{2}$, we might expect the frustration to be more fragile in systems where the interactions cannot

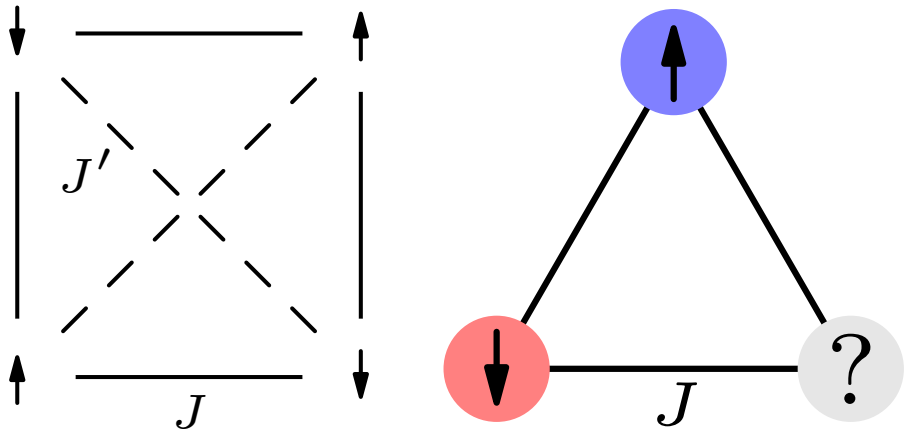

Figure 2.2: (left) Square unit with antiferromagnetic interactions. $J > 0$ are nearest neighbour interactions and $J' > 0$ are next-nearest neighbour interactions. These interactions can be satisfied depending on the ratio J/J'. (right) Triangular unit of classical Ising spins with antiferromagnetic interaction, $J > 0$. All three bonds cannot be satisfied simultaneously.

be controlled carefully. Instead, the triangular lattice is highly frustrated for any nearest-neighbour antiferromagnetic coupling.

2.2 Properties of Frustrated Systems

Before focusing on the triangular lattice Ising antiferromagnet (TLIAFM), we discuss a naïve measure of frustration. We use the susceptibility, which is experimentally accessible, to define a measure of frustration. The Curie-Weiss law gives a form for the high-temperature susceptibility

$$\chi \propto \frac{1}{T - \Theta_{CW}}. \tag{2.1}$$

For materials with antiferromagnetic interactions, Θ_{CW} is negative, but $T_N = |\Theta_{CW}|$ gives a scale which is the Néel temperature [6]. Below this, we expect magnetic ordering. Frustrated systems may show an ordering temperature, T_c, but the hallmark of frustration is that these temperatures are typically much lower than T_N. Thus, we take a large ratio T_N/T_c to be a signature of magnetic frustration [4]. One part of the explanation for this large ratio is related to the degeneracy of the

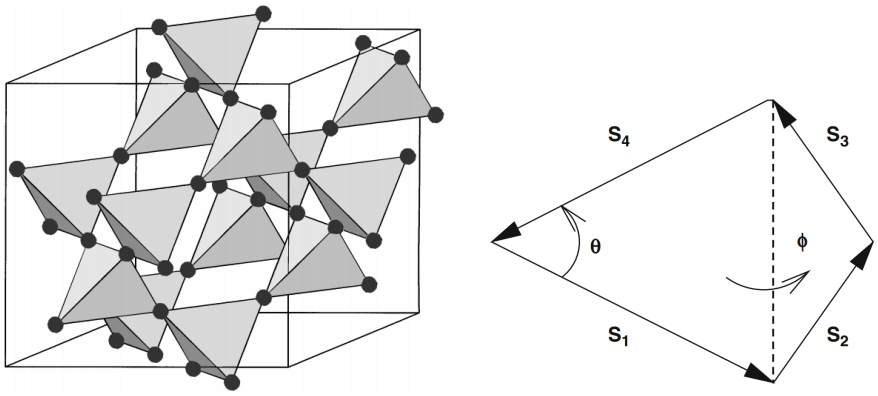

Figure 2.3: (left) Figure from [8]. Pyrochlore lattice composed of corner-sharing tetrahedra. (right) Figure from [6]. Ground state configuration for the classical Heisenberg antiferromagnet on the pyrochlore lattice.

ground-state. To illustrate the degeneracy of the ground-state and to provide another example of a geometrically frustrated system, we introduce the classical Heisenberg antiferromagnet on the pyrochlore lattice [7]. Consider a Hamiltonian of the form

$$H = J \sum_{\langle i,j \rangle} \mathbf{S}_i \cdot \mathbf{S}_j, \tag{2.2}$$

where $\langle i, j \rangle$ are nearest-neighbours, J is antiferromagnetic, and $|\mathbf{S}_i| = 1$. In the pyrochlore lattice, each spin $\mathbf{S}_i$ is coupled to the six nearest neighbours which are part of the two tetrahedra to which $\mathbf{S}_i$ belongs, see Fig. 2.3.

This Hamiltonian can be rewritten in terms of a sum over the tetrahedra, indexed by α, by introducing the sum

$$\mathbf{L}_\alpha = \sum_{i \in \alpha} \mathbf{S}_i, \tag{2.3}$$

$$H = \frac{J}{2} \sum_{\alpha} |\mathbf{L}_\alpha|^2 - JN, \tag{2.4}$$

where N is the number of spins.

For the ground state, we require $\mathbf{L}_\alpha = \mathbf{0}$ for all tetrahedra. This can be satisfied by configurations of vectors with two internal degrees of freedom, as shown in Fig. 2.3. We now analyse the ground-state degeneracy using a Maxwellian counting argument. If we have N Heisenberg spins, each has two degrees of freedom. If we have N_c terms

in the sum over tetrahedra, each one gives three constraints. Since spins are shared between two tetrahedra, there are half as many tetrahedra as spins. Assuming that the constraints are independent and can be satisfied simultaneously, we would expect $2N - 3N/2 = N/2$ degrees of freedom in the ground-state.

This is notable because it is macroscopic in the number of spins in the system. This conclusion gives a strong motivation for why the ordering temperature might be so reduced as mentioned above. The system can fluctuate between many of the degenerate configurations without exiting the ground-state manifold.

We now specialise to the triangular lattice Ising antiferromagnet and will see that the degeneracy of the ground-state plays an important role in the lack of an ordering transition. The Hamiltonian is

$$H = J \sum_{\langle ij \rangle} \sigma_i \sigma_j, \tag{2.5}$$

where $\sigma_i = \pm 1$, $\langle ij \rangle$ indicates nearest-neighbours, and J is antiferromagnetic. The triangular units in this lattice are all frustrated and the ground state simply consists of configurations in which all the triangular units have one spin $+1$, one spin -1 and the third can have either orientation. This lattice is not bipartite and is instead made of three sublattices.

In 1950, Wannier [9] and Houtappel [10] presented exact solutions of the nearest-neighbour triangular lattice Ising antiferromagnet. They computed the partition functions for triangular (and other, including honeycomb) lattices exactly using transfer matrices. We will not review the method they used, but instead make note of some statements from this work that have provided important guiding philosophies for the study of frustrated magnets and related systems. The first relates to the degeneracy of the ground state. Wannier determined that the triangular lattice Ising antiferromagnet retains a finite entropy at zero temperature

$$S_0 \approx 0.33 k_B. \tag{2.6}$$

Wannier points out that while there are ordered states, there are also states with macroscopic numbers of spins which can be flipped. These latter states are ener-

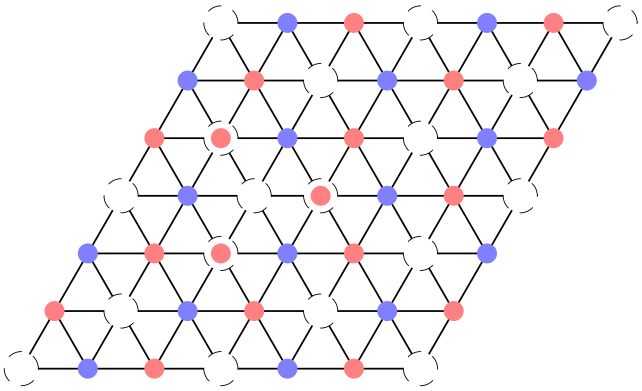

Figure 2.4: A ground-state configuration with finite entropy is shown. Spin states are fixed on two of three sublattices (indicated by different colours) and free to fluctuate on the other (indicated by blank circles). "Contingent freedom" allows for further entropic freedom depending on the free spins.

getically equivalent but have finite entropy. Additionally, within these finite entropy states, there are potentially more possibilities for entropy. Wannier describes this as "contingent freedom" and one of these scenarios is shown in Fig. 2.4. In this scenario, one of the ground states has spin fixed on two of the sublattices and all the spins on the third sublattice are free to fluctuate. If three nearest-neighbour spins from the same fluctuating sublattice have the same spin state, the formerly fixed spin can fluctuate.

Configurations with long-range order may have spin states fixed on the three sublattices. Wannier makes the claim that long-range order cannot exist in this system. In particular, one can have disparate ground-state regions in a system ordered differently from each other but with a transition region that is also in the ground state. Thus there is no energetic reason to favour the long-range order and the entropic considerations of other configurations dominate. The triangular lattice Ising antiferromagnet is highly fluctuating down to zero temperature. Further analytic work [11] has derived a form for the spin-spin correlation function that decays as a power-law in the distance.

The question of experimental realisations is a nuanced one as there are myriad other factors that one must consider. First, dimensionality and the existence of truly

two-dimensional (2D) systems. Usually, when one wants to study the TLIAFM, this will be addressed by working with materials for which there is little interlayer coupling. Additionally, one may wonder whether quantum mechanics will affect the physics at low temperatures. In this work, we will consider the former and not discuss the possibility of the latter. Regardless, experiments have observed both the diminished ordering temperature and signatures of strong correlations in systems that are made up of triangular units or tetrahedra; see [4, 6] for reviews.

The combination, within geometrically frustrated magnets, of strong correlations and large fluctuations has elicited the term "cooperative paramagnetism" [15] or "spin liquid". Spin liquids, both classical and those with quantum degrees of freedom, have been of particular interest in recent years and there has been much experimental and theoretical progress to describe them beyond the context of frustration [16]. We will not attempt to describe the vast range of possibilities for spin liquid behaviour, but instead briefly list some of the more tantalising properties and predictions.

First, there is a class of materials called "spin ice". While the name originates in an analogy to water ice, the low temperature behaviour of these materials can be essentially described by a classical spin liquid. The model is a pyrochlore lattice with spins on the shared sites which either point into or out of each tetrahedron. The remarkable property of this model is that it can be described using an emergent electromagnetic theory which yields power-law correlations and the possibility of magnetic monopoles [17]. Recently, signatures of this physics have been sought in experiments [18–22].

In our study of three-dimensional (3D) geometrically frustrated magnets, we will see the highly fluctuating, strongly correlated behaviour that we have described above can arise in purely classical situations and can still be highly relevant to experiment and real systems. Leveraging extensive Monte Carlo simulations, we will probe a classical spin liquid regime and we will also see that an emergent field theory can provide additional clarity in understanding how this behaviour arises.

2.3 Outline of Part II

The rest of Part II proceeds as follows. First, in Chapter 3, we introduce these systems and provide some background about experiments and previous work. In Chapter 4, we introduce the models that we study and present results from mean-field theory and the self-consistent Gaussian approximation. These results provide a starting point for analysing these systems. Then, in Chapter 5, we describe the numerical simulations used to study these models. The Monte Carlo method employed is described and results for the phase diagram, correlations, and structure factor are shown. Next, in Chapter 6, an emergent field is introduced to provide another means of understanding these systems. Specifically, we introduce the height model formalism and show how it can be used to provide understanding here. Then, in Chapter 7, we carry out a renormalisation group (RG) analysis of the height model and present an argument incorporating anomalously soft modes and vortices to elucidate the spin liquid regime. Lastly, in Chapter 8, the different methods used to study stacked triangular lattice Ising antiferromagnets are compared and the phase diagram is discussed.

Chapter 3

Stacked Triangular Lattice Ising Antiferromagnets

The triangular lattice Ising antiferromagnet (TLIAFM) is arguably the simplest model of a highly frustrated magnet and was probably the earliest such system to be studied in detail [9, 10]. At low temperatures it is both highly fluctuating and strongly correlated; indeed, it remains disordered down to zero temperature and has a macroscopically degenerate ground state. The combination of fluctuations with correlations is typical more generally of highly frustrated magnets, which in this regime have been termed cooperative paramagnets or classical spin-liquids [6].

We consider three-dimensional (3D) Ising antiferromagnets built from triangular layers that are stacked in such a way that nearest-neighbour interlayer interactions are frustrated, and make comparisons with the unfrustrated stacking. We focus on low-temperature behaviour in systems with weak interlayer coupling, where correlations within each layer are necessarily strong but correlations between layers are controlled by a competition between fluctuations and interactions. Using a combination of perturbative and non-perturbative analytical techniques and Monte Carlo simulations, we show that this competition leads to a classical spin-liquid regime, in which strong correlations exist without long range order.

Models for frustrated magnets can be classified at the mean-field level according to the properties of the matrix of exchange interactions. In this approach, the eigenvectors associated with the minimum eigenvalues of the interaction matrix provide candidate ordering patterns. These minimum eigenvalues appear at isolated points

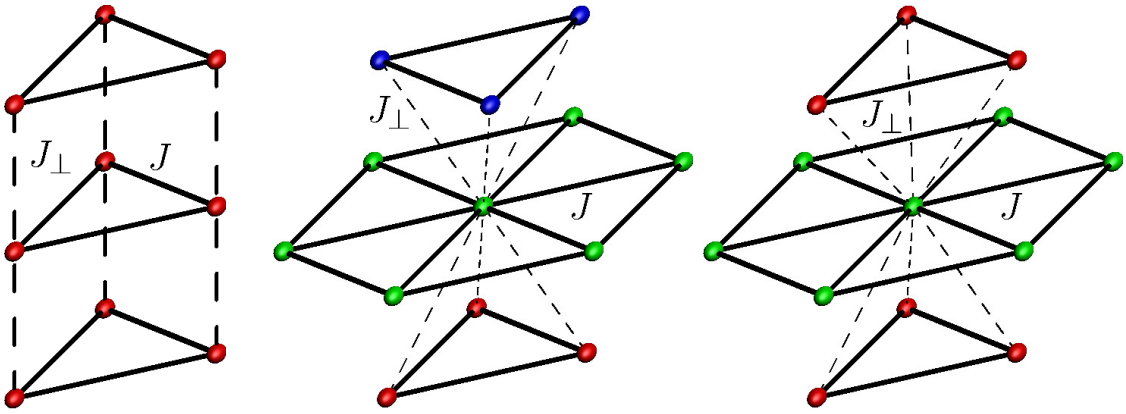

Figure 3.1: The three different ways of stacking triangular lattices that are considered in this work: *aaa*, *abc*, *abab* stacking. In-plane interactions, J, and interlayer interactions, $J_\perp$, are indicated with full and dashed lines, respectively, and are taken to be antiferromagnetic in this work.

in reciprocal space for unfrustrated systems, but may be highly degenerate for frustrated systems. For example, for nearest neighbour interactions on the kagome and pyrochlore lattices, the subspace of minimum eigenvalues forms a flat band that spans the entire Brillouin zone [6, 25, 26]. Other cases display intermediate behaviour: on the diamond lattice with nearest and next-nearest neighbour interactions, the minimum eigenvalues form a two-dimensional surface in the 3D Brillouin zone [27]. The systems we discuss here are distinctive in having minimum eigenvalues that lie on *lines* in the 3D Brillouin zone [28]. One of our central findings is that these systems have a cooperative paramagnetic regime in which they develop strong correlations that are centred near these reciprocal-space lines.

The three different ways of stacking triangular layers that we compare in this work are indicated in standard notation by *aaa*, *abc*, and *abab*: see Fig. 3.1. Of these, the first provides a reference model without interlayer frustration, while the *abc* stacking yields minimum eigenvalues along helices in the Brillouin zone, and the *abab* stacking gives minimum eigenvalues on a ring around the Brillouin zone corner. With equal in-plane and interlayer interactions, the *abc* stacking is equivalent to a nearest-neighbour model on the face-centred-cubic (fcc) lattice, while the *abab* stacking forms the hexagonal-close-packed (hcp) lattice.

Moving beyond a mean-field classification, the theoretical understanding of stacked triangular lattice Ising antiferromagnets (TLIAFMs) that we develop here is based on the height model description of low-temperature states for a single layer [29, 30]. This long-established model represents ground states of a layer in terms of an emergent height field, with a simple effective Hamiltonian that captures the entropy of fluctuations. A spin-flip excitation fractionalises into an unbound vortex-antivortex excitation pair in the height field, and the vortex separation sets the correlation length at finite temperature in the single-layer model. In the following we derive and study height models for weakly coupled multilayer systems, showing how the interplay of interlayer coupling and vortex excitations allows strong correlations to develop between layers, without long-range order. We also use the results of extensive Monte Carlo simulations to test these conclusions and to examine behaviour when interlayer coupling is not weak. In the rest of this chapter, we outline some of the key experimental results that serve partly as motivation for this study, and also some of the previous work on these, and related, systems.

3.1 Experiments and Previous Work

Although no real materials are known to exist with magnetic degrees of freedom and structure that are in our systems, there are physical systems that embody the physics of the stacked triangular lattice Ising antiferromagnets. These systems are found in the transition metal family $R\mathrm{Fe_2O_4}$.

In $R\mathrm{Fe_2O_4}$, R is a rare-earth element: Y, Dy, Ho, Er, Tm, Yb, Lu, Sc, In. Part of the crystal structure is stacked triangular lattices. Although the overall structure is more complicated than the stackings we consider, one component of the structure is layers of iron. We will neglect layers of other atoms and details such as a bilayer spacing between iron layers. These layers of iron contain the necessary ingredients for the models we will consider. The iron ions are a mixture (within each layer) of Fe^{2+} and Fe^{3+}. The triangular geometry leads to frustration in these charge degrees of freedom.

Experimental reports have proposed diverse physics across a wide range of temperatures in these materials. The complex interplay between magnetism and charge-ordering has led to discussion of the material as a multi-ferroic and a complete understanding of the systems as a whole remains out of reach for a variety of reasons. These reasons include the theoretical complexity of treating all degrees of freedom in light of the highly frustrated geometry, practical constraints due to the sensitivity of the materials' properties on chemistry, and difficulties in conclusive experimental characterisation of some properties. The gist of the experimental observations we will be concerned with is that, within the charge degrees of freedom, there is a low-temperature $3D$ ordered regime, a broad regime of partial ordering, and a high-temperature disordered state. A precise description of the regimes observed in these experiments has remained unclear.

One of the specific set of experimental studies that serves as partial motivation for our work is observations [31, 32] of charge-ordering in the materials $LuFe_2O_4$ and $YbFe_2O_4$. The charge states (rather than the magnetic states) of Fe^{2+} and Fe^{3+} ions in these systems can be represented using Ising pseudospins, with antiferromagnetic coupling between pseudospins arising from screened Coulomb interactions [31, 33]. The pseudospins occupy the sites of an *abc*-stacked triangular lattice, though with a bilayer spacing that we have mentioned above and will not include for the model we study. The coupling between the layers in these materials is generally weaker than the coupling within the layers. This is a useful feature as one of the analytic approaches that we employ relies on weak interlayer coupling as a starting point for perturbative analysis.

Experimental studies [31, 32, 34], in particular of $YbFe_2O_4$ [32], find helices of scattering intensity in a temperature range above a three-dimensional charge-ordering transition, see Fig. 3.2. These helices mirror in their reciprocal space location the positions of minimum eigenvalues of the interaction matrix discussed above. While an accurate description of these materials requires treating additional (magnetic) degrees of freedom [34], the results we present in this paper demonstrate how strong interlayer

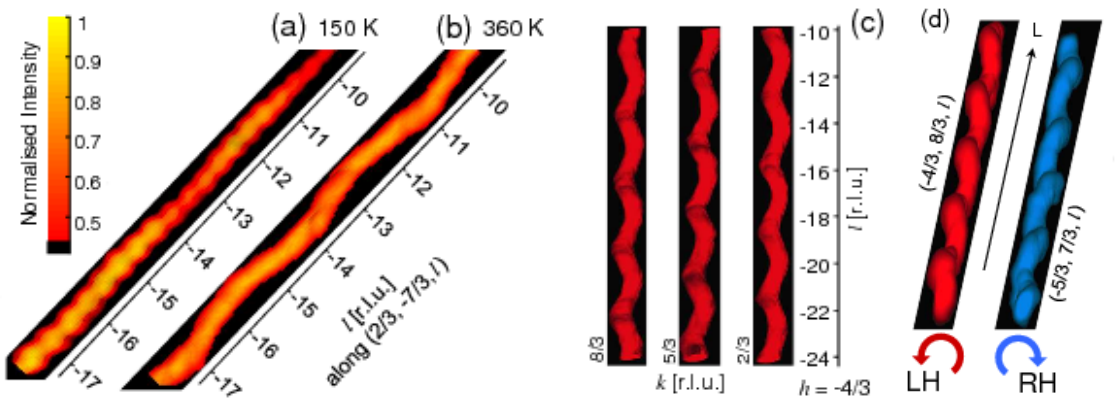

Figure 3.2: (Picture taken from [32]) Helices of scattering intensity from x-ray diffraction experiments. (a) and (b) show the helices below and above the onset of $3D$ charge-ordering at $T \approx 320\,K$. (c) demonstrates that the Brillouin zone corner on which a given helix is centred determines the phase, but not the pitch of the helices. (d) shows the different parity of helices centred on adjacent corners in the Brillouin zone.

correlations can arise over an extended temperature range without long-range order.

Past theoretical work on charge-ordering in these materials has included quite detailed mean-field treatments [31, 33] and Monte Carlo simulations of a bilayer model [35], but has not made use of the understanding of single-layer TLIAFMs provided by height models, nor used simulations to study correlations in the paramagnetic phase with the detail we present here. The prior Monte Carlo simulations used systems of size $6 \times 6 \times 2$ [35] and attempted to analyse both charge and spin ordering structures.

Prior mean-field studies of the charge-ordering demonstrate that coupling between sites two layers apart is needed to break the macroscopic degeneracy of the predicted ordering pattern. Harris and Yildirim [33] study charge and magnetic degrees of freedom within a mean-field picture and focus on the development of various orders and the transitions between them. Fig. 3.3 shows some of the further neighbour couplings that those studies have included. Further neighbour couplings will be excluded from our numerical work, but play an important role in the analytic arguments that we will present.

TLIAFMs with other stackings have been examined previously in a variety of

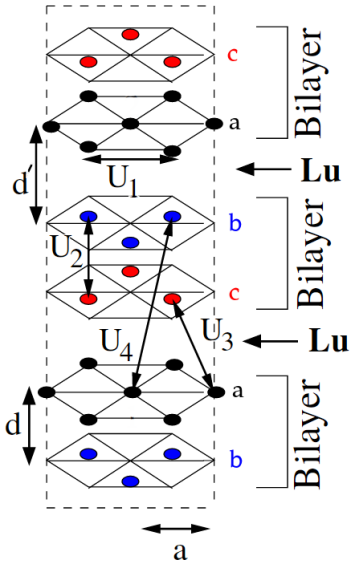

Figure 3.3: Figure adapted from [33]. In this work, couplings analogous to U_1 are considered via J and U_2, U_3 via $J_\perp$.

contexts. Treatments of the *abab* case include mean-field theory, a low temperature expansion, and Monte Carlo simulations [36–38]. That work has probed the ordering transition, but without examining the limit of weakly coupled layers or correlations in the paramagnetic phase. Most of that work centres on a regime with strong interlayer coupling (larger than the in-plane coupling) in which there is an exact solution along a line in parameter space. Those studies have investigated the possible presence of a Lifshitz point along this line. It is also observed that there is a ferromagnetic phase boundary that appears to coincide with this line; low-temperature expansions and Monte Carlo simulations have been used to investigate this possibility in particular.

TLIAFMs with unfrustrated (*aaa*) stacking have been of long-standing interest [39]. They display a continuous phase transition that, strikingly, is in the 3D XY universality class despite the absence of a microscopic continuous symmetry [40, 41]. The two components of the order parameter represent ordering at the two inequivalent Brillouin zone corners, and the XY symmetry is broken in the ordered phase by dangerously irrelevant six-fold anisotropies. This model and transition are also important as an imaginary time representation of the quantum dimer model on the

hexagonal lattice [42].

Regarding experiments on other stackings, there are materials that realise the *aaa* stacking with magnetic degrees of freedom [43], but these have non-Ising degrees of freedom and dominant interlayer, rather than in-plane, interactions.

It is primarily the charge-ordering materials of the *abc* stacking that we discussed above which provide motivation for our work on the STLIAFM. In particular, the regime with strongly coupled layers but without disorder has resisted a clear explanation and characterisation. We aim to provide understanding via thorough numerics starting from the simplest bare model and conceptual clarity via analytical tools that permit a more precise description of the classical spin-liquid regime.

Chapter 4

Model and Mean-field Results

In this chapter, we use mean-field theory and the self-consistent Gaussian approximation to investigate the nearest-neighbour Ising antiferromagnet on stacked triangular layers with anisotropic couplings. We will introduce these methods and examine their predictions for the three stackings mentioned in Chapter 3. The *aaa*, or simple, stacking gives a starting point for generalising to 3D without including interlayer frustration. The latter two stackings, *abc* and *abab*, introduce frustration beyond the in-plane frustration of the triangular lattice.

Our models will be defined as followed. The spins are coupled to each of the six neighbours in-plane with antiferromagnetic exchange coupling $J > 0$. Each spin is also coupled to the nearest spins in the adjacent layers with exchange coupling $J_\perp$. The number of couplings between spins in adjacent layers will depend on the stacking; see Fig. 3.1. The Hamiltonian is

$$H = J \sum_{\langle ij \rangle, z} \sigma_{i,z} \sigma_{j,z} + J_\perp \sum_{\{ij\}, z} \sigma_{i,z} \sigma_{j,z+1}, \tag{4.1}$$

where $\sigma_{i,z} = \pm 1$, $\langle ij \rangle$ indicates nearest-neighbours within a layer, and $\{ij\}$ indicates nearest-neighbours in adjacent layers. It is also possible to consider further-neighbour terms in the Hamiltonian, which may be present in a physical system or generated through renormalisation. $J_\perp$ is assumed to be positive as it can be switched via the transformation $\sigma_{i,z} \to \sigma'_{i,z} = (-1)^z \, \sigma_{i,z}$.

4.1 Mean-field Theory

Mean-field theory is a long-established method for solving problems in statistical physics. It relies on a simplified picture of interactions between degrees of freedom that typically assumes fluctuations can be ignored and degrees of freedom are independent. One starts by decomposing the system into two components. Usually one component is tractable and refers to single degrees of freedom and the second component includes interactions.

We start by writing $\mathcal{H}(\{\sigma\}) = \mathcal{H}_0(\{\sigma\}) + \mathcal{H}_1(\{\sigma\})$, where $\mathcal{H}_0$ is simple enough so that we can evaluate the following quantities

$$\langle \dots \rangle_0 = \frac{\sum_{\{\sigma\}} \dots e^{-\beta \mathcal{H}_0}}{\mathcal{Z}_0}, \tag{4.2}$$

where the sum is over configurations and $\mathcal{Z}_0$ is the partition function for $\mathcal{H}_0$. From here, one recalls the Bogoliubov identity

$$F \leq \langle \mathcal{H} \rangle_0 - TS_0. \tag{4.3}$$

By considering a tractable $\mathcal{H}_0$, we can evaluate $\langle \mathcal{H} \rangle_0$ and S_0 to obtain a parametrisation of the free energy. Minimising this free energy provides expressions for order parameters dependent on the temperature.

The usual example is a nearest-neighbour Ising model. Using a mean-field approach, one can make qualitative and quantitative predictions about the phase diagram for this system. For example, mean-field theory predicts a phase transition, the transition temperature, and the critical exponents. However, even for that simple model, there are caveats. Namely, it predicts a transition in one dimension which does not occur. Additionally, it greatly over-estimates the transition temperature in two dimensions. Qualitatively, we might expect that mean-field approaches overestimate transition temperatures because they often neglect fluctuations which are not actually negligible. The predictions for critical exponents reveal another flaw in this mean-field theory. Within mean-field theory, the number of spin components in the degrees of freedom (e.g. whether one has Ising or Heisenberg spins) does not affect the values of critical exponents.

Despite these flaws, in the case of frustrated systems, mean-field theory can provide some insight. However, the insight is limited by dramatic shortcomings with respect to crucial questions, such as ordering transitions and patterns. The variational free energy for a nearest-neighbour Ising model is given by

$$\langle \mathcal{H} \rangle_0 - TS_0 = \sum_{\langle i,j \rangle} J_{ij} m_i m_j + \frac{k_B T}{2} \sum_i m_i^2, \tag{4.4}$$

where m_i are the on-site magnetisations. In the mean-field picture, the ordering pattern is predicted by the eigenvectors of $\mathbf{J}$ associated with the minimum eigenvalues. The ordering temperature is obtained from the minimum eigenvalues, ϵ. For example, systems with Ising degrees of freedom have an ordering temperature $T_c = -2\epsilon$. This formalism immediately fails when applied to the single-layer TLIAFM: mean-field theory predicts an ordering temperature $T_c = \frac{3}{2}J$ when there is not, in fact, any transition down to zero temperature.

Despite the failings with respect to the prediction of the ordering temperature, the mean-field formalism can still be leveraged to gain some understanding of the stacked systems that we consider. For example, the eigenvalues of the interaction matrix for the stacked systems yield minima with macroscopic degeneracy – a paradigmatic signature of frustrated magnetism. Let us now consider some of these candidate patterns.

4.1.1 Mean-field Predictions

We now present the results of applying mean-field theory to the stacked triangular lattice systems we have introduced. Before starting, we introduce the following coordinate choices. We fix the origin at one of the sites and define $\hat{x}$ parallel to any one of the triangle sides. We then pick $\hat{y}$ perpendicular to $\hat{x}$ and in-plane. We choose $\hat{z}$ perpendicular to the triangular layers. The in-plane lattice vectors chosen are

$$\mathbf{a}_1 = (1, 0, 0) \tag{4.5}$$

$$\mathbf{a}_2 = (1/2, \sqrt{3}/2, 0). \tag{4.6}$$

There is unit spacing between layers for the *aaa* and *abc* stackings and unit spacing between a layers in the *abab* stacking. The *abab* stacking has two sites per primitive unit cell. Using $\boldsymbol{\delta}$ for the separation between neighbouring sites in adjacent layers, $\boldsymbol{\delta} = (0, 0, 1)$, $\left(\frac{1}{2}, \frac{1}{2\sqrt{3}}, 1\right)$ and $\left(\frac{1}{2}, \frac{1}{2\sqrt{3}}, \frac{1}{2}\right)$ for the *aaa*, *abc* and *abab* stackings, respectively.

The in-plane reciprocal lattice vectors are

$$\mathbf{A}_1 = 2\pi(1, -1/\sqrt{3}, 0); \tag{4.7}$$

$$\mathbf{A}_2 = 2\pi(0, 2/\sqrt{3}, 0). \tag{4.8}$$

For a single triangular layer, in reciprocal space the interaction matrix becomes diagonal with values given by

$$\mathbf{J}_{2D}\left(\mathbf{q}\right) = J\left[\cos\left(q_x\right) + 2\cos\left(\frac{q_x}{2}\right)\cos\left(\frac{\sqrt{3}q_y}{2}\right)\right]. \tag{4.9}$$

Thus the minima in the triangular-lattice Brillouin zone for in-plane interactions are

$$\mathbf{K} = \left(\frac{4\pi}{3}, 0\right); \tag{4.10}$$

$$\mathbf{K}' = \left(\frac{2\pi}{3}, \frac{2\pi}{\sqrt{3}}\right). \tag{4.11}$$

For the *aaa* stacking, the minima are still isolated points in reciprocal space. The combined interaction matrix in reciprocal space is now given by $\mathbf{J}(\mathbf{q}) \equiv \mathbf{J}_{2D}(\mathbf{q}) + \mathbf{J}_{\perp}(\mathbf{q})$, where $\mathbf{J}_{\perp}(\mathbf{q}) = J_{\perp}\cos q_z$. In this case, they occur at $\left(\frac{4\pi}{3}, 0, \pi\right)$ and $\left(\frac{2\pi}{3}, \frac{2\pi}{\sqrt{3}}, \pi\right)$.

However, for the two frustrated stackings, the minima are no longer single points or discrete sets of degenerate points. Instead the minima of the interaction matrix are highly degenerate, continuous lines in 3D. To see this, first introduce the notation $\zeta = 1 + e^{i\mathbf{q}\cdot\mathbf{a}_1} + e^{i\mathbf{q}\cdot\mathbf{a}_2}$.

For the *abc* stacking, the interaction matrix in reciprocal space is now given by $\mathbf{J}(\mathbf{q}) = \mathbf{J}_{2D}(\mathbf{q}) + \mathbf{J}_{\perp}(\mathbf{q})$, where

$$\mathbf{J}_{\perp}(\mathbf{q}) = J_{\perp}(\zeta e^{-i\mathbf{q}\cdot\boldsymbol{\delta}} + \text{c.c.})/2, \tag{4.12}$$

and c.c. stands for complex conjugate. Using the ζ notation, $\mathbf{J}_{2D}$ can be written as $J\left(|\zeta|^2 - 3\right)/2$. The combined interaction matrix for the *abc* stacking is

$$\mathbf{J}(\mathbf{q}) = \frac{J}{2}\left|\zeta e^{-i\mathbf{q}\cdot\boldsymbol{\delta}} + J_{\perp}/J\right|^2 - \frac{3J}{2} - \frac{J_{\perp}^2}{2J}. \tag{4.13}$$

The minima of this expression clearly occur when $\zeta = -(J_\perp/J)e^{i\mathbf{q}\cdot\boldsymbol{\delta}}$. This condition defines a continuous line of minima in reciprocal space when $J_\perp/J$ is small enough. When $J_\perp \ll J$, one can more easily understand the structure of these minima by expanding $\mathbf{J}(\mathbf{q})$ to second order around one of the minima for a single triangular layer, e.g. $\mathbf{k} = \mathbf{K}$. This expansion gives

$$\mathbf{J}(\mathbf{q}) \approx -3J - \sqrt{3}J_\perp \left(\tilde{q}_x \cos q_z - q_y \sin q_z\right) + \frac{3J}{4}\left(\tilde{q}_x^2 + q_y^2\right) + J_\perp \left(\left(\tilde{q}_x - q_y^2\right)\cos q_z\right), \tag{4.14}$$

where $\tilde{q}_x = q_x - 4\pi/3$. Minimising this expression, to lowest order in $J_\perp$, we obtain a helix given by

$$\tilde{q}_x \approx \frac{2J_\perp}{\sqrt{3}J}\cos\left(q_z\right), \tag{4.15}$$

$$q_y \approx -\frac{2J_\perp}{\sqrt{3}J}\sin\left(q_z\right). \tag{4.16}$$

The general form of the minima can be written with reference to the two minima in the triangular lattice Brillouin zone. Concretely, if $\mathbf{k} = \mathbf{K} + n_1\mathbf{A}_1 + n_2\mathbf{A}_2 + \mathbf{q}$, the line is

$$q_x \approx \frac{2J_\perp}{\sqrt{3}J}\cos\left(q_z + \frac{2\pi}{3}p\right), \tag{4.17}$$

$$q_y \approx -\frac{2J_\perp}{\sqrt{3}J}\sin\left(q_z + \frac{2\pi}{3}p\right) \tag{4.18}$$

where $p = n_1 + n_2$. For $\mathbf{k} = \mathbf{K}' + n_1\mathbf{A}_1 + n_2\mathbf{A}_2 + \mathbf{q}$ the line is

$$q_x \approx -\frac{2J_\perp}{\sqrt{3}J}\cos\left(q_z + \frac{2\pi}{3}p'\right), \tag{4.19}$$

$$q_y \approx -\frac{2J_\perp}{\sqrt{3}J}\sin\left(q_z + \frac{2\pi}{3}p'\right), \tag{4.20}$$

where $p' = 2 + n_1 + n_2$. The difference between helices around $\mathbf{K}$ and $\mathbf{K}'$ is that one is a left-handed helix and the other is right-handed. Varying p, p' gives variation in the phase of the helices.

We note that higher-order corrections to Eq. 4.14 will deform the helix to have a more triangular projection in the $x - y$ plane, but they do not lift the degeneracy of the minima in the interaction matrix.

For the *abab* stacking, the interaction matrix is more complicated because there are two sites per unit cell. The combined interaction is given by a block matrix

$$\mathbf{J}(\mathbf{q}) = \begin{pmatrix} \mathbf{J}_{2D}(\mathbf{q}) & \mathbf{J}_{\perp}^{ab}(\mathbf{q}) \\ \mathbf{J}_{\perp}^{ba}(\mathbf{q}) & \mathbf{J}_{2D}(\mathbf{q}) \end{pmatrix} \tag{4.21}$$

with $\mathbf{J}_{\perp}^{ab}(\mathbf{q}) = J_{\perp}\zeta\cos(q_z/2)e^{i\mathbf{q}\cdot\boldsymbol{\delta}}$ and $\mathbf{J}_{\perp}^{ba}(\mathbf{q}) = [\mathbf{J}_{\perp}^{ab}(\mathbf{q})]^*$. The eigenvalues are

$$\epsilon_{\mathbf{q}}^{\pm} = \frac{J}{2}(|\zeta|^2 - 3) \pm J_{\perp}\cos\left(q_z/2\right)|\zeta|. \tag{4.22}$$

Minima lie on the line

$$q_z = 0, |\zeta| = J_{\perp}/J. \tag{4.23}$$

For $J_{\perp} \ll J$ they form circles around $\mathbf{K}, \mathbf{K}'$ in the triangular-lattice Brillouin zone.

The mean-field approach for these systems has thus predicted degenerate ordering patterns along continuous lines in reciprocal space. We can extract more understanding from the spectrum of the interaction matrix by allowing for fluctuations in the spin degrees of freedom.

4.2 Self-consistent Gaussian Approximation

The self-consistent Gaussian approximation is closely related to the mean-field approach. In fact, it presents another method of approximating the partition function. One can understand it as a means of going beyond mean-field theory and accounting for some of the fluctuations of the spins [44]. However, one can also imagine it as a way of taking the constraint on the spin-length into account when computing the partition function. The partition function for our systems is formally

$$\mathcal{Z} = \int \prod_i d\left\{\sigma_i\right\} \delta\left(|\sigma_i| - 1\right) e^{-\beta\mathcal{H}}. \tag{4.24}$$

However, computing this exactly is difficult for finite-size systems and unsolved for infinite systems. Using a Hubbard-Stratonovich transformation[45], we can express the partition function using a continuous auxiliary field. Upon carrying out the sum over σ_i configurations exactly, the partition function is

$$\int \prod_i d\{\phi_i\} e^{-\mathcal{L}(\phi_i)} e^{-\beta\mathcal{H}(\phi_i)}, \tag{4.25}$$

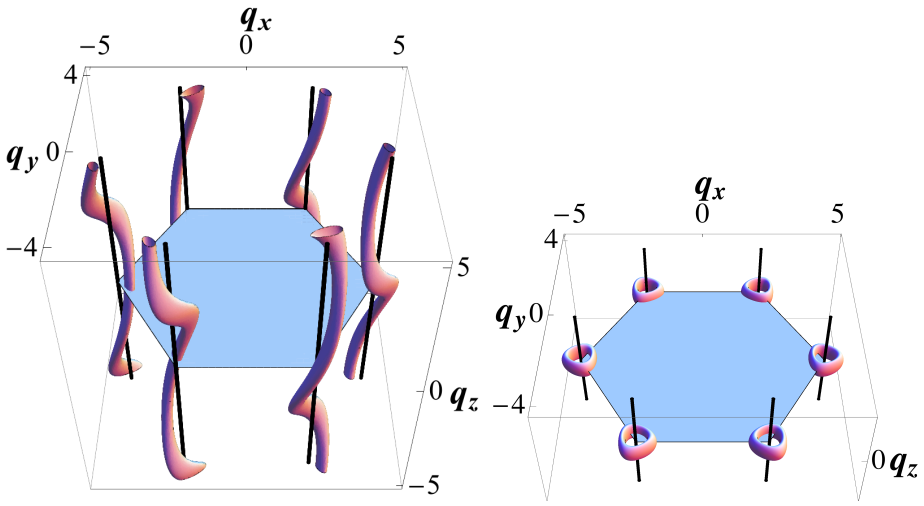

Figure 4.1: Surfaces of equal, near-minimal eigenvalues of the interaction matrix for (left) the *abc* stacking, and (right) the *abab* stacking, at $J_\perp/J = 0.2$.

where $\mathcal{L}(\phi_i)$ is an effective potential which can be approximated quadratically to recover a Gaussian theory. The two-point function, $\langle\phi_i\phi_j\rangle$, under the Gaussian approximation, is equivalent to $\langle\sigma_i\sigma_j\rangle$ up to normalisation. We retain the notation σ_i, but where σ_i are understood to be continuous variables. Our partition function is

$$\int \prod_i d\{\sigma_i\} e^{-\lambda\sigma_i^2} e^{-\beta\mathcal{H}}, \tag{4.26}$$

where λ is fixed by the requirement $\langle|\sigma_i|^2\rangle = 1$. This constraint implies that the average spin-length is preserved. Within the framework of the SCGA, we can now easily evaluate expectations by calculating Gaussian functional integrals.

$$\langle O\rangle = \frac{1}{\mathcal{Z}} \int d\{\sigma_i\} O e^{-\frac{1}{2}\sum_{\langle i,j\rangle}\sigma_i(\beta J_{ij}+\lambda\delta_{ij})\sigma_j}. \tag{4.27}$$

We will use the spin-spin correlation function often. Within the SCGA, it is

$$\langle\sigma_i\sigma_j\rangle = \left[(\beta\mathbf{J}+\lambda\mathbf{I})^{-1}\right]_{ij}. \tag{4.28}$$

From this expression, we can write the self-consistency constraint

$$\langle|\sigma_i|^2\rangle = \left[(\beta\mathbf{J}+\lambda\mathbf{I})^{-1}\right]_{ii} = 1. \tag{4.29}$$

There are, however, caveats for the SCGA. For instance, one recovers exact results for n-component spins in the limit where $n \to \infty$. Nonetheless, the SCGA has proven useful as an improvement to mean-field theory. It has been used to give an indication of likely behaviour in geometrically frustrated magnets with Ising spins, despite the concerns that $n = 1$ is far from the limit where we expect this approximation to be exact. In particular, the correlations and structure factor predicted by the SCGA for classical Ising pyrochlore antiferromagnets are remarkably accurate when compared with Monte Carlo results[46].

The most striking predictions we use from the SCGA are those for the structure factor. We can compute the structure factor within the SCGA by taking the Fourier transform of the spin-spin correlation function. Then we write the spectral decomposition of $\mathbf{J}$ in terms of its eigenvalues $\epsilon^l_{\mathbf{q}}$ and eigenvectors $u^l_{\mathbf{q}}(\alpha)$, where α labels sites within a unit cell and l labels the bands of $\mathbf{J}$.

$$S(\mathbf{q}) = \frac{1}{N} \sum_{i,j} \left[(\beta \mathbf{J} + \lambda \mathbf{I})^{-1} \right]_{ij} e^{i\mathbf{q}\cdot(\mathbf{r}_i - \mathbf{r}_j)} \tag{4.30}$$

$$= \sum_{l,\alpha,\alpha'} \frac{u^{l*}_{\mathbf{q}}(\alpha)\, u^l_{\mathbf{q}}(\alpha')}{\beta \epsilon^l_{\mathbf{q}} + \lambda}. \tag{4.31}$$

From this it is apparent (barring cancellations in the sum $\sum_{\alpha,\alpha'} u^{l*}_{\mathbf{q}}(\alpha)\, u^l_{\mathbf{q}}(\alpha')$) that maxima in $S(\mathbf{q})$ arise from minima in $\epsilon^l_{\mathbf{q}}$.

We can apply the SCGA to the systems we are interested in and study the correlations. In Fig. 4.1, we have predictions for surfaces of near-minimal eigenvalues of the interaction matrix. These can be used to predict the intensity of the structure factor for the *abc* and *abab* stackings. These predictions clearly indicate degeneracy along lines (helices and rings) in the 3D Brillouin zone which we expect. In Chapter 5, we introduce Monte Carlo simulations to probe these systems. We will see how these compare with the SCGA in detail with respect to the structure factor and correlations, and qualitatively in terms of providing access to ordering transitions.

Chapter 5

Numerical Results

Monte Carlo techniques have been used since the 19th century to solve problems in physics. In the context of statistical physics problems, one can use Monte Carlo, or sampling, methods to approximately compute the partition function and to sample from the Boltzmann distribution of the problem. There are technical and practical requirements that constrain the mode of sampling and we discuss these now.

We will be primarily concerned with computing expectation values of observables, such as energy or magnetisation. We define these as

$$\langle O \rangle = \frac{\sum_\mu O_\mu e^{-\beta E_\mu}}{\sum_\mu e^{-\beta E_\mu}}, \tag{5.1}$$

where μ is a state of the system, E_μ is the energy of the system in state μ, O_μ is the value of observable O in state μ, and $\beta = \frac{1}{k_B T}$ is the inverse temperature (we work with $k_B = 1$).

Computing these exactly is only tractable for systems with very few states (usually this means extremely small or extremely simple systems). Assume instead, that we consider the Monte Carlo method for estimating these quantities, and suppose we sample the states of the system with some distribution p_μ. Then, the estimate of our expectation, given that we have M samples, is

$$O_M = \frac{\sum_{i=1}^{M} O_{\mu_i} p_{\mu_i}^{-1} e^{-\beta E_{\mu_i}}}{\sum_{j=1}^{M} p_{\mu_j}^{-1} e^{-\beta E_{\mu_j}}}. \tag{5.2}$$

As $M \to \infty$, the estimate approaches the exact value, $O_M \to \langle O \rangle$. However, the rate of convergence is highly dependent on the distribution, p_μ, of sampling the states of the system. This is often due to the fact that the sums involved are dominated

by very few states, e.g. the ground state when the system is at low-temperatures. In fact, by picking states uniformly at random for an Ising system with 1000 spins, O_M is unlikely to accurately compute $\langle O \rangle$ even after several hours on a modern desktop computer.

However, a choice for the sampling distribution exists which allows much more efficient computation of observables. This choice is to insist that the sample states are drawn according to their Boltzmann distribution weight. In physical systems, states are dictated by Boltzmann weights and so sampling according to these weights is natural in a reasonable sense. Using this choice, $p_\mu = Z^{-1} e^{-\beta E_\mu}$, the estimate is

$$O_M = \frac{1}{M} \sum_{i=1}^{M} O_{\mu_i}. \tag{5.3}$$

If one is given a black box to draw sample states from in such a manner, the computation of observables is reduced to simple averaging and the error is bounded only by one's patience. Now we consider the processes used to generate samples from such distributions.

5.1 Monte Carlo Algorithms

In this context, Markov processes are stochastic processes which generate a new state, ν, given a starting state μ. The transition probability, $P(\mu \to \nu)$, determines the distribution of states generated. For the process to be Markovian, the transition probabilities do not depend on the previous history of the system and only depend on the states μ, ν. When a Markov process is equipped with two properties, ergodicity and detailed balance, we can ensure that the states generated by the Markov process, after many transitions, are distributed according to a chosen distribution.

Ergodicity is the requirement that all states be accessible via the process. This can be contrasted with the requirement that every state is accessible from every other state. Instead, it will often be the case that states are inaccessible from most states, but that there exists a sequence of transitions between a state and any other state.

Detailed balance is a more subtle requirement that ensures that the states gener-

ated by the Markov process are the ones desired. Detailed balance is explicitly the condition that

$$p_\mu P(\mu \to \nu) = p_\nu P(\nu \to \mu). \tag{5.4}$$

Detailed balance implies that the system comes to equilibrium with states distributed according to p_μ. In particular, we can use detailed balance to show that the system makes transitions equally into and out of any state at the same rate

$$\sum_\nu p_\mu P(\mu \to \nu) = \sum_\nu p_\nu P(\nu \to \mu). \tag{5.5}$$

In order for the states from the Markov process to be distributed according to the Boltzmann distribution, detailed balance implies that we must have

$$\frac{P(\mu \to \nu)}{P(\nu \to \mu)} = e^{-\beta(E_\nu - E_\mu)}. \tag{5.6}$$

The last nuance of using Markov processes to generate states according to the Boltzmann distribution is the choice of transition probabilities. To account for this, we introduce selection and acceptance probabilities. Specifically, we write $P(\mu \to \nu) = g(\mu \to \nu) A(\mu \to \nu)$. $g(\mu \to \nu)$ is the selection probability of ν, given a state μ. $A(\mu \to \nu)$ is the proportion of the transitions from $\mu \to \nu$ that should be accepted. The motivation for this factorisation is the freedom to select states using a convenient process and to accept them with as high a rate as possible while maintaining the constraint from detailed balance and the desired Boltzmann distribution.

The details of the selection and acceptance for our simulations are now presented. These choices are known as the Metropolis algorithm and it is the most widely used and famous of Monte Carlo methods. This algorithm is a single-spin-flip algorithm. The Markov process considers states, μ, ν, which differ by flipping a single spin. The selection probability and acceptance probabilities are

$$g(\mu \to \nu) = \frac{1}{N}, \tag{5.7}$$

$$A(\mu \to \nu) = \begin{cases} e^{-\beta(E_\nu - E_\mu)} & E_\nu - E_\mu > 0 \\ 1 & \text{otherwise.} \end{cases} \tag{5.8}$$

These choices are physically very intuitive. First, we select a spin uniformly at random to be flipped. Then, if the state after the spin-flip, ν, has a lower energy than the current state, μ, the flip should be accepted with probability 1. If the new state has a higher energy, it is accepted with a probability set by the Boltzmann distribution. This discourages transitions to states with lower Boltzmann weights. We refer to this process as a step and will measure time in the Monte Carlo simulation by sweeps, which are N steps where N is the number of spins in the system.

Further caveats when utilising Monte Carlo simulations include the details of equilibration and measurements of observables. There are two timescales that one can consider for these issues. First, equilibration time refers to the number of sweeps necessary to ensure that the system has equilibrated at a given temperature. A common technique for estimating this time scale is comparing the time-series for various observables given different initial conditions. Correlation time refers to the number of sweeps necessary to ensure that samples of system states, for the purposes of computing expectation values, are independent. This is often measured by the exponential decay of the nutocorrelation of an observable.

These two issues are generally challenging for frustrated systems like the ones we consider in this work. Equilibration and decorrelation can be difficult because the energy landscape of a frustrated system is fraught with local minima and energy barriers that prevent adequate exploration of state space. This hinders the accurate computation of observables. To address these challenges, we adopt a technique called parallel tempering.

5.1.1 Parallel Tempering

Parallel tempering involves simultaneous simulation of identical systems at different fixed temperatures. At regular intervals, we allow two systems at different temperatures to exchange their spin configurations. The exchange protocol is chosen so that the ergodicity and detailed balance conditions are preserved [47]. The result of the swaps is that systems can exit local minima by swapping to higher temperatures.

This achieves the improvements to equilibration and decorrelation that we desire.

If we have two systems at different temperatures, $T_i < T_j$, the proposed swap of the configurations has acceptance probability

$$A(\mu \to \nu) = \begin{cases} e^{-(\beta_i - \beta_j)(E_j - E_i)} & E_j - E_i > 0 \\ 1 & \text{otherwise.} \end{cases} \tag{5.9}$$

The selection probability will be set by another convention. In our simulations, we require an even number of temperatures and alternate between proposed swaps with higher and lower temperature-adjacent systems. At step k, we select temperature pairs $(T_0, T_1), (T_2, T_3), \ldots$ to swap. At step, $k+1$, we select $(T_0, T_1), (T_2, T_3), \ldots$ to swap. These proposals occur between single-spin flip Monte Carlo simulations in each system, the number of which depends on the temperature of the system.

The choices of the number of systems, N_r, to simulate and the temperatures, $\{T_i\}$, used are again dictated by heuristics and, to some degree, trial and error. One general argument for the spacing of the temperatures can be given. The probability of a parallel tempering swap move between temperature-adjacent systems being accepted is $e^{-(\beta_i - \beta_{i+1})(E_{i+1} - E_i)}$. Using the definition of the heat capacity, $C_v = \frac{dE}{dT}$, we can approximate

$$(E_{i+1} - E_i) \approx (T_{i+1} - T_i) C_v, \tag{5.10}$$

$$(\beta_i - \beta_{i+1})(E_{i+1} - E_i) \approx \left(\frac{T_{i+1} - T_i}{T_i T_{i+1}} \right) (T_{i+1} - T_i) C_v, \tag{5.11}$$

$$\approx \left(\frac{(T_{i+1} - T_i)^2}{T_i^2} \right) C_v. \tag{5.12}$$

If we demand an acceptance probability, e^{-a}, and use the fact that $C_v \propto bN$, then we can rearrange the above to obtain

$$a \approx \left(\frac{(T_{i+1} - T_i)^2}{T_i^2} \right) C_v, \tag{5.13}$$

$$\frac{T_{i+1}}{T_i} \approx 1 + \sqrt{\frac{a}{bN}} = 1 + \frac{\alpha}{\sqrt{N}}. \tag{5.14}$$

This indicates that we should space the temperatures by geometric progression. We can adjust the constant $\alpha = \sqrt{\frac{a}{b}}$ to tune the acceptance probability. We find that this

scheme is a good guideline, but not perfect for our purposes. We must also take into account the need for finely spaced temperatures to detect phase transitions and the inclusion of temperatures which are high enough to be fully in the conventional paramagnetic regime. Details about our simulations in particular and their equilibration will be presented below.

5.2 Implementation and Equilibration

We will now discuss some details of how the stacked triangular lattice Ising antiferromagnets are simulated using the Monte Carlo method described above. The simulations were carried out on Theoretical Physics' computing cluster, Hydra. The code was written in `C++` and Open MPI was used for parallelisation. Other packages used include Gnuplot and FFTW.

A system consists of L_z rhombic layers, each of size $L \times L$ lattice constants, with periodic boundary conditions in all directions. A typical simulation treats $N \approx 10^5$ sites ($L = 72-200, L_z = 12-48$) using 10^5 sweeps. The parallel tempering parameters are adjusted from the rough considerations above to ensure equilibration. Generally, we include $N_r = 40-200$ copies of the system at different temperatures. The primary observables computed are the energy E, specific heat C, and the structure factor $S(\mathbf{q})$, which is obtained from the Fourier transform of magnetisation

$$\tilde{\sigma}(\mathbf{q}) = \sum_i e^{i\mathbf{q}\cdot\mathbf{r}_i}\sigma_i \tag{5.15}$$

as

$$S(\mathbf{q}) = \frac{1}{L^2 L_z}\langle|\tilde{\sigma}(\mathbf{q})|^2\rangle. \tag{5.16}$$

We monitor the overlap of energy distributions at adjacent temperatures in the parallel tempering scheme, as substantial overlap is a requirement for effective exchange of replicas. In Fig. 5.1, we see that the distributions overlap significantly which implies that configurations will efficiently transit from low- to high-temperature simulations. However, depending on the spacing of temperatures and the presence of first-order transitions, it is possible that a configuration will not be able to visit all of the tem-

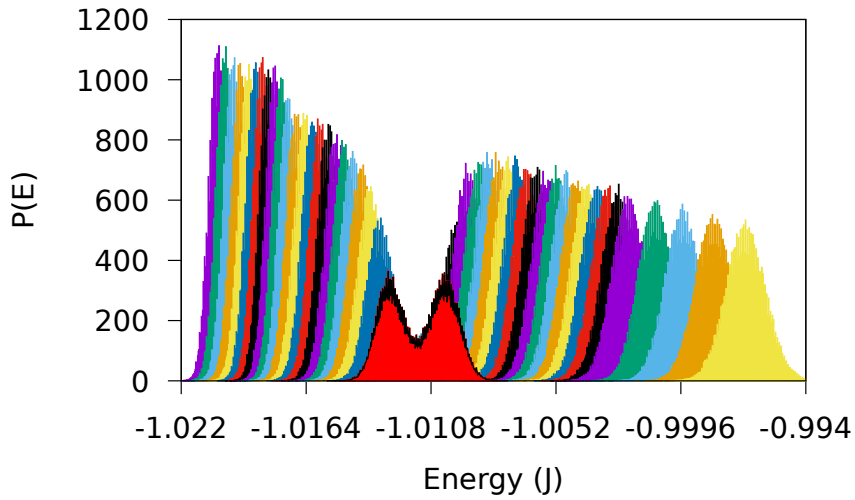

Figure 5.1: Energy distributions for the *abc* stacking with $J_\perp = 0.1J$. Temperatures in the range $0.4J \leq T \leq 0.65J$. Different colours represent different temperatures. The bimodal distribution centred near $E = -1.012$ is a signature of a first-order phase transition.

peratures, $\{T_i\}$. If the spacing of temperatures is too coarse, then we might expect difficulty equilibrating in the presence of transitions with latent heat. This behaviour can be seen in Fig. 5.2, in particular, one of the systems is briefly "stuck" in the ordered phase, before being swapped into the disordered phase by a parallel tempering swap. The temperature at which this barrier appears would correspond with the separation of the energy distributions and indicates the transition.

The movement in temperature space can also be characterised by the average time it takes a system to travel through the entire range of temperatures. In Table 5.1 below, we see the average trip time, τ_R, between temperatures just above the critical temperature and the upper temperatures in the parallel tempering ensemble. The process is expected to be roughly diffusive and, therefore, proportional to the number of temperatures squared. A caveat to this estimation is that systems can get "stuck," as previously mentioned, in the ordered state, thereby distorting the traversal times. This timescale is additionally relevant for determining independence of measurements of observables. It is reasonable, albeit conservative, to assume that once a system has reached the highest temperatures in the ensemble, it will be sufficiently de-correlated

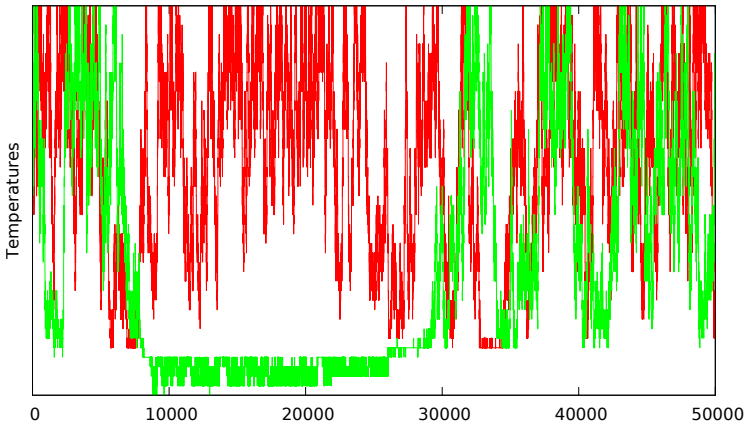

Figure 5.2: Two systems ($L = 36$) exploring temperature space via parallel tempering swap moves over the course of the simulation. Time is given in units of sweeps on the horizontal axis.

$J_\perp$	T_c/J	T range	$\langle\tau_R\rangle$	$\frac{2\tau_R}{N_R}$
1.0	1.72 ± 0.020	$1.8 \rightarrow 3.6$	144.9	19.3
0.4	0.99 ± 0.008	$1.1 \rightarrow 3.6$	357.6	27.5
0.2	0.68 ± 0.014	$0.8 \rightarrow 3.6$	523.3	31.7
0.1	0.50 ± 0.010	$0.4 \rightarrow 3.6$	1089.5	45.4

Table 5.1: Times (in lattice sweeps) to traverse temperature range at various interaction strength for four systems ($L = 12$).

from its initial state. Thus, given that we have an ensemble with N_R systems being simulated, we can assume that after $\frac{2\tau_R}{N_R}$ parallel tempering swap moves, measurements of system properties will be sufficiently de-correlated. We find that $\frac{2\tau_R}{N_R}$ is generally on the order of N_R. As discussed previously, we can consider autocorrelation times to judge whether measurements are sufficiently independent. We can examine the time-displaced autocorrelation for any observable, for example, magnetisation

$$\chi(t) = \int \mathrm{d}t' \left[m(t') - \langle m\rangle\right]\left[m(t'+t) - \langle m\rangle\right] \sim \exp\left[\frac{-t}{\tau}\right], \tag{5.17}$$

$$\int_0^\infty \mathrm{d}t \frac{\chi(t)}{\chi(0)} = \int_0^\infty \mathrm{d}t \exp\left[-\frac{t}{\tau}\right] = \tau \tag{5.18}$$

We expect that $\chi(t)$ will decay exponentially [47], so we ensure independence of measurements by taking them at intervals of 2τ, where τ is the natural time-scale. Heuristic arguments quickly show that it is reasonable to expect $\tau \approx 1$ Metropolis

sweep and this is confirmed for various systems. However, in the parallel tempering framework, these correlation times are computed to be nearly exactly 1 because they are measured in time-steps of swaps and it is expected that the swaps will strongly de-correlate observables such as magnetisation and energy.

The details of simulations and efficiency of algorithms can vary tremendously. In the case of parallel tempering, this is especially true. However, we have used the standard measures, in addition to heuristic arguments that we have checked for our simulations (e.g. diffusive τ_R and overlap of energy distributions), to be confident in our simulations.

5.3 Phase Diagram and Ordering Transition

In this section we discuss the phase diagrams of the three stacked triangular lattice systems we have simulated. Several signatures are generally used to locate phase transitions and determine boundaries in phase diagrams. Before discussing these signatures, though, it is helpful to review some facts about related systems that provide a starting point for our discussion of the phase diagram for STLIAFMs. First of all, there can be no phase transition when interlayer coupling is absent, $J_\perp = 0$. The single-layer model is known to remain paramagnetic down to $T = 0$. Second, the point $J_\perp = J$ in the *abc* case is well-known in the context of the face-centred-cubic lattice and exhibits a strongly first-order transition [48, 49]. One also expects that the transition temperature of the frustrated stackings will be lowered as compared with the simple, unfrustrated, stacking. This follows intuitively from the idea that degeneracy and disorder due to frustration prevent ordering. Maxima in the heat capacity are a traditional signature used to locate transitions. Especially in the case of first-order transitions, with a discontinuity in the energy as a function of temperature, this can be a very clear signature. However, the heat capacity is just one moment of the distribution. The transition in these systems can also be seen clearly from considering the entire distribution. In particular, we expect a bimodal energy distribution for a system at a temperature near the transition temperature.

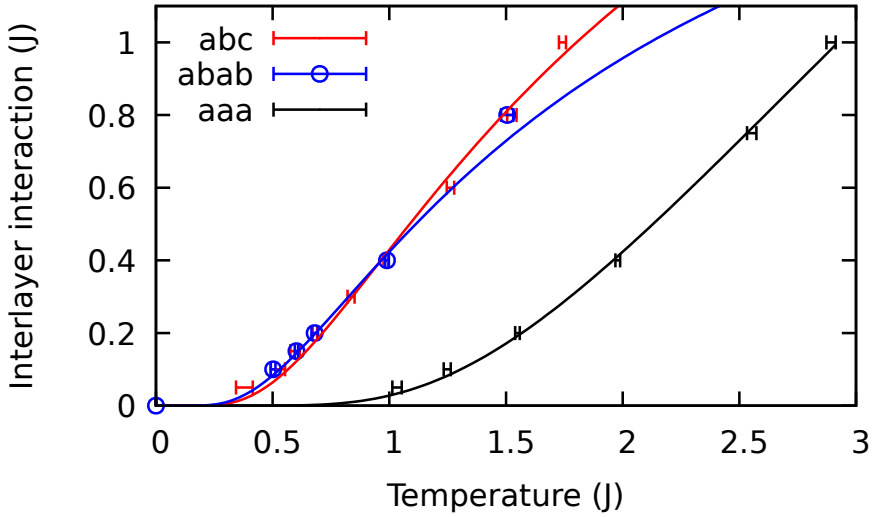

Figure 5.3: Phase boundaries for the unfrustrated (*aaa*) and frustrated (*abc* and *abab*) stackings. Points: data from Monte Carlo simulations. Lines: fits to height model theory of Chapters 6, 7.

Phase diagrams as a function of T and $J_\perp$ are shown in Fig. 5.3 for both the unfrustrated (*aaa*) and the frustrated (*abc* and *abab*) stackings. For a given strength of interlayer coupling, the ordering temperature (determined from the maximum of the heat capacity, see Fig. 5.5 for an example) is indeed much lower in the systems with frustrated stackings compared with the unfrustrated one. In addition, over most of the range of $J_\perp/J$ studied, the transitions in the systems with frustrated stackings remain strongly first-order. The first-order nature can be seen in both signatures mentioned above. The probability distribution of the energy is strongly bimodal at the transition unless $J_\perp/J \ll 1$. The peak in the heat capacity follows from this observation and also from direct numerical results. The discontinuity in the energy at the transition decreases with decreasing $J_\perp$, and for $J_\perp \lesssim 0.05J$ the order of the transition is not discernible from the simulations. Examples of the energy distribution at different temperatures are shown in Fig. 5.4.

Differences in transition temperature between the two frustrated stackings are very small for $J_\perp/J \leq 1$. The results for the *abc* stacking at $J_\perp = J$ can be compared with earlier work on the fcc lattice, and are in good agreement with the transition

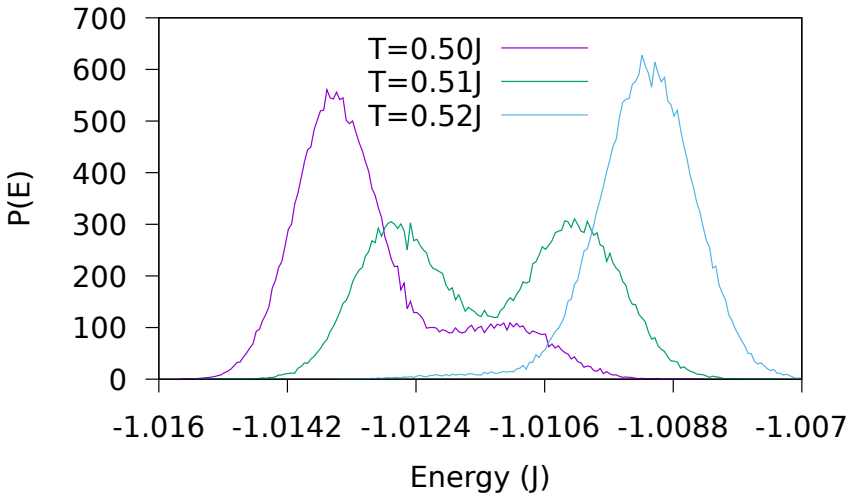

Figure 5.4: Energy distributions for the *abc* stacking with $J_\perp = 0.1J$. Temperatures shown are near the transition. System size $L = 72$, $L_z = 12$. The distribution in the centre is for a system at the middle temperature. Its bimodal form indicates a first-order transition.

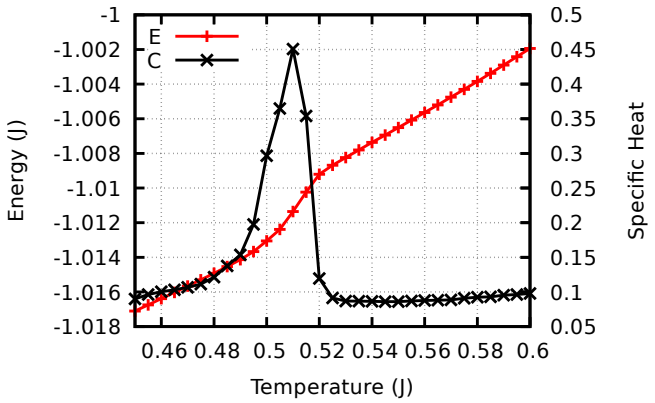

Figure 5.5: Energy and specific heat for the *abc* stacking with $J_\perp = 0.1J$. The transition is clearest from the large peak in the specific heat and is accompanied by a noticeable drop in the energy as a function of temperature. System size $L = 72$, $L_z = 12$. Based on a comparison with Fig. 5.4, we conclude that this is a first-order transition, although this is not as easy to see from the curve of energy.

temperature of $T_c \approx 1.72J$ found in [48, 49].

While questions remain unanswered about the nature of the transition at small interlayer coupling and also with regard to the details of the ordering mechanism, we are interested in the region of parameter space firmly in the paramagnetic state.

5.4 Structure Factor and Correlations

A characteristic feature of classical spin-liquids is the presence of strong correlations and a large correlation length, without long-range order or proximity to a critical point. In this section we present correlation functions and correlation lengths for TLIAFMs with frustrated stackings, determined from Monte Carlo simulations. We will explain the results first in 5.4.1 and 5.4.2 before giving details of the data analysis methods in 5.4.3. Notably, the results corroborate the results from the SCGA approach and also qualitatively agree with relevant results from experiments.

5.4.1 *abc* stacking

The behaviour of the structure factor for a system with *abc* stacking in the classical spin-liquid regime is illustrated in Fig. 5.6. Combining information from the series of slices in reciprocal space that are shown in this figure, it is apparent that maxima in $S(\mathbf{q})$ lie on helices in reciprocal space. The axes of these helices pass through corners of the triangular-lattice Brillouin zone.

To analyse this behaviour quantitatively, we extract a reciprocal-space radius Q for the helix and a correlation length $\xi_\perp$ by fitting data for $S(\mathbf{q})$ near the maxima to a sum of in-plane Lorentzians

$$S\left(\mathbf{q}\right) = \frac{I}{\xi_\perp^2 \left(\mathbf{q}_\perp - \mathbf{q}_\perp^0(q_z)\right)^2 + 1} \tag{5.19}$$

from each helix. Provided any dependence of $|\mathbf{q}^0(q_z)|$ on q_z is weak, we can make the identification $Q = |\mathbf{q}^0(q_z)|$.

Results are shown in Fig. 5.7. The correlation length $\xi_\perp$ increases rapidly with decreasing T for $T \lesssim J$, as demonstrated in Fig. 5.7(a). It reaches large values within

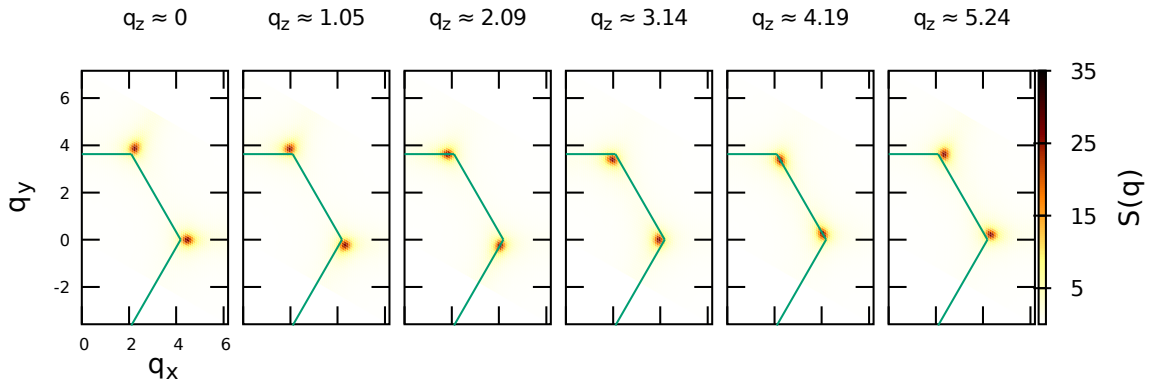

Figure 5.6: Cross-sections of structure factor at constant q_z in a system with *abc* stacking. For each q_z, sharp maxima in $S(\mathbf{q})$ occur near the Brillouin zone boundary, which is shown as a green dashed line. As q_z increases, the maxima precess around the zone corners without significant change in intensity, indicating that they form helices in the three-dimensional reciprocal space. Parameter values are $J_\perp = 0.2J$, $T = 0.8J$, $L = 72, L_z = 12$; for this value of $J_\perp$, $T_c = (0.68 \pm 0.01)J$.

the paramagnetic phase if $J_\perp/J$ is small. Its dependence on $J_\perp$ at fixed T is very weak. The variation of the helix radius Q with $J_\perp$ and T is illustrated in Fig. 5.7(b). Its value is given quite accurately by the SCGA, Eq. (4.15), for $T \gtrsim J$, and shows a small increase with decreasing temperature.

In the ordered phase, Bragg peaks are expected in the structure factor, in place of a continuous distribution of weight on helices. We probe the evolution between the two behaviours by computing

$$S_{\text{avg}}(q_z) = \frac{1}{L^2} \sum_{q_x, q_y} S(\mathbf{q}) \,. \tag{5.20}$$

Results in Fig. 5.8 show the rapid development of Bragg peaks as temperature is lowered through the transition. Although we believe (from the bimodal energy distribution of Fig. 5.4) that the transition is first-order for the value of $J_\perp/J$ studied here, discontinuities are not apparent in the temperature dependence of $S_{\text{avg}}(q_z)$, presumably because of finite-size rounding.

5.4.2 *abab* stacking

Because the *abab*-stacked lattice has two sites in a primitive unit cell, the relation between fluctuations and correlations is less direct than for the *abc* stacking, in which

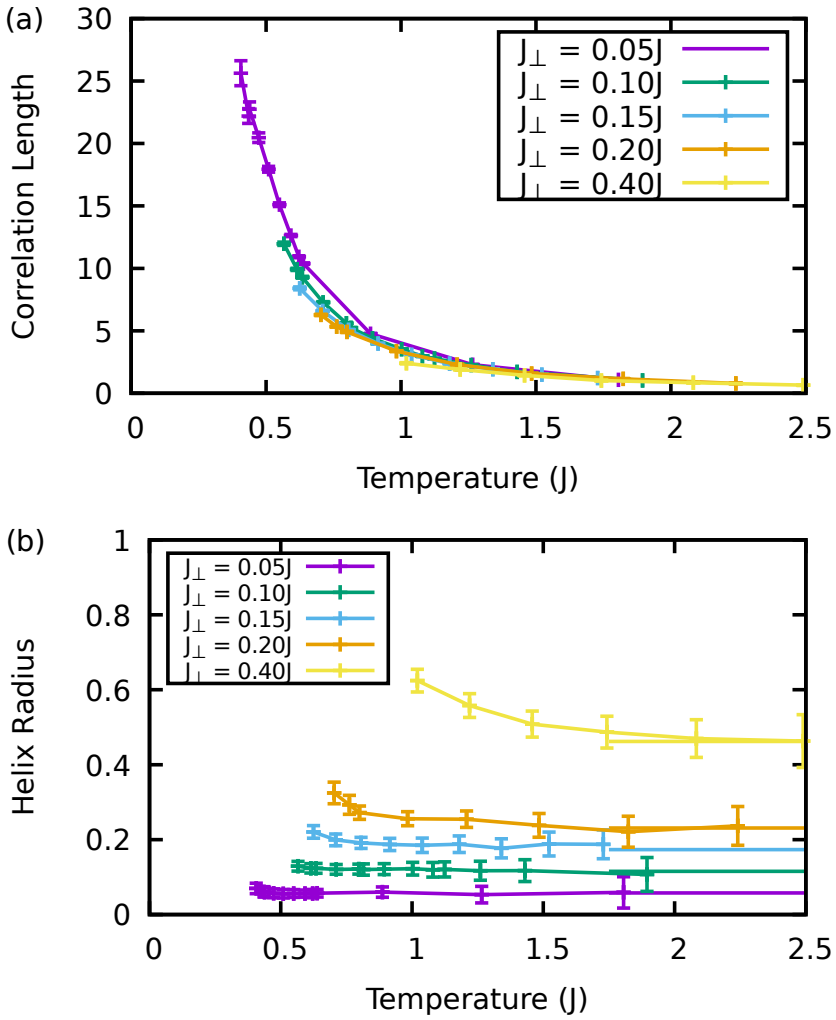

Figure 5.7: (a) Correlation length $\xi_\perp$ and (b) helix radius Q, as a function of temperature for various values of $J_\perp$ in the *abc* stacking. $\xi_\perp$ is measured in units of lattice spacing, Q in units of inverse lattice spacing. Dashed lines are SCGA predictions for Q from Eq. (4.15). Results were obtained in a system of size $L = 72, L_z = 12$. Data for each value of $J_\perp$ extend to the lowest temperature employed in parallel tempering that was above T_c.

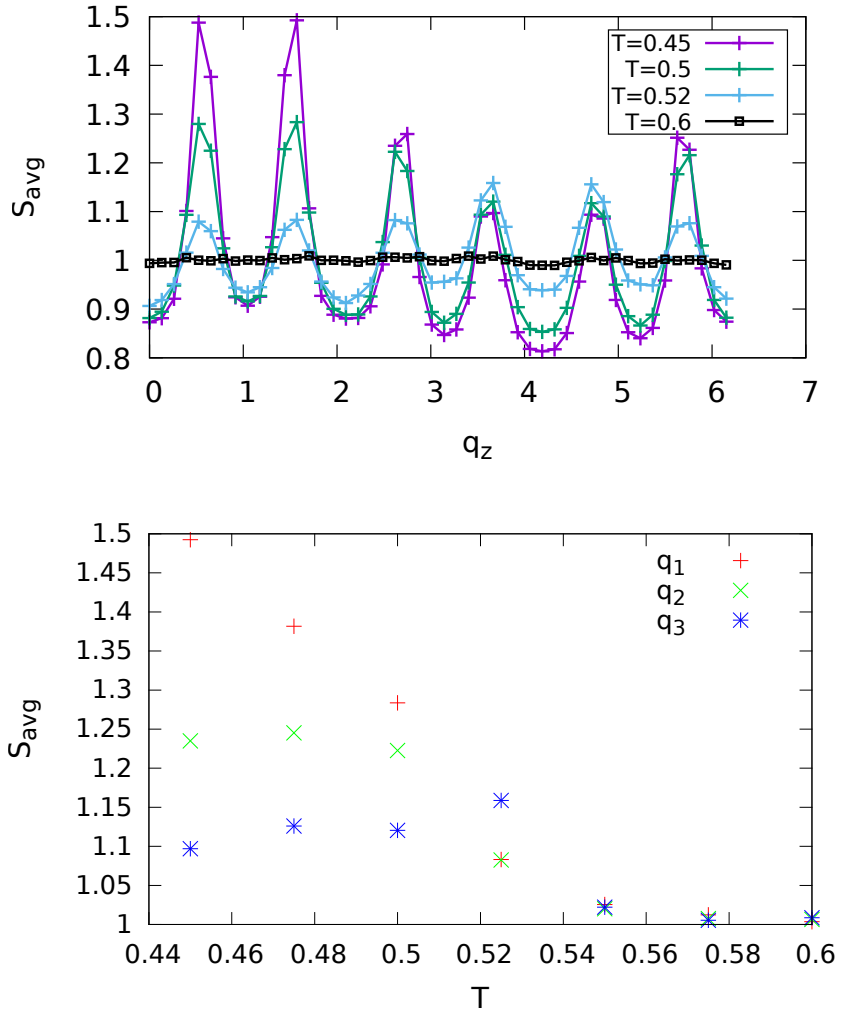

Figure 5.8: Development of Bragg peaks in the ordered phase for the *abc* stacking. Top: $S_{\rm avg}(q_z)$ [Eq. (5.20)] as a function of q_z at four selected temperatures near the transition, in a system with $J_\perp = 0.1J$. Data are for $T = 0.45J$, $0.5J$, $0.52J$ and $0.6J$, in order of decreasing peak intensity, and the transition temperature is $T_{\rm c} \approx 0.54J$. Bottom: $S_{\rm avg}(q_z)$ as a function of T for the three values of q_z that are marked with vertical dashed lines in the top panel. Results for both panels were obtained in a system of size $L = 36$, $L_z = 48$.

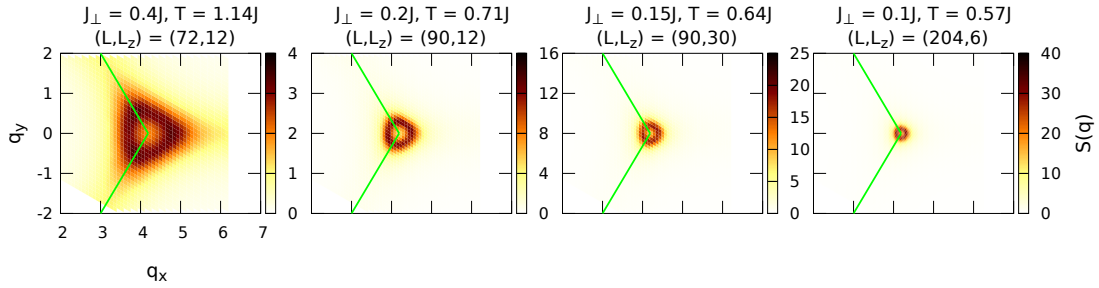

Figure 5.9: Cross-sections of structure factor at $q_z = 0$ for systems with varying $J_\perp$ in the *abab* stacking. Intensity is maximum on a closed loop, which is approximately circular for small $J_\perp/J$ but develops triangular distortions with increasing $J_\perp/J$. Data (from left to right) are for $T = 1.14J$, $0.71J$, $0.64J$, $0.57J$, obtained in systems of size $L = 72$, 90, 90, 204 and $L_z = 12$, 12, 30, 6. Note the changing intensity scale and increasing maximum intensity as $J_\perp$ and T decrease. The ordering temperatures are $T_c/J = 0.99 \pm 0.008$, 0.680 ± 0.014, 0.602 ± 0.007 and 0.502 ± 0.01.

the unit cell has a single site. More specifically, the form of $S(\mathbf{q})$ is affected by interference between contributions from the two sites. Within the SCGA, this is apparent from Eq. (4.31), where contributions involving a given eigenvalue $\epsilon^l_{\mathbf{q}}$ of the interaction matrix are weighted by a sum,

$$\sum_{\alpha,\alpha'} u^{l*}_{\mathbf{q}}(\alpha)\, u^{l}_{\mathbf{q}}(\alpha')\,, \tag{5.21}$$

that includes both site-diagonal ($\alpha = \alpha'$) and interference ($\alpha \neq \alpha'$) terms. In order to eliminate these interference effects and expose fluctuations in the *abab* stacking in a simple way, we compute the structure factor using contributions only from one of the two sites in each unit cell, by restricting the sum in Eq. (4.31) to this set of sites.

We expect from Eq. (4.23) that this single-sublattice structure factor will have its maxima lying on closed loops in the $q_z = 0$ plane. An overview of our data, illustrating this behaviour, is given in Fig. 5.9.

A simple way to extract a correlation length $\xi_\perp$ is by fitting data for $q_z = 0$ and q_x, q_y close to a selected Brillouin zone corner to the functional form

$$S(\mathbf{q}) = \frac{I}{\xi_\perp^2 \left(Q - |\mathbf{q}_\perp - \mathbf{K}|\right)^2 + 1}, \tag{5.22}$$

where $\mathbf{K}$ denotes the location of the Brillouin-zone corner and Q specifies the reciprocal-space radius of the ring of intensity. This fitting function provides a good description

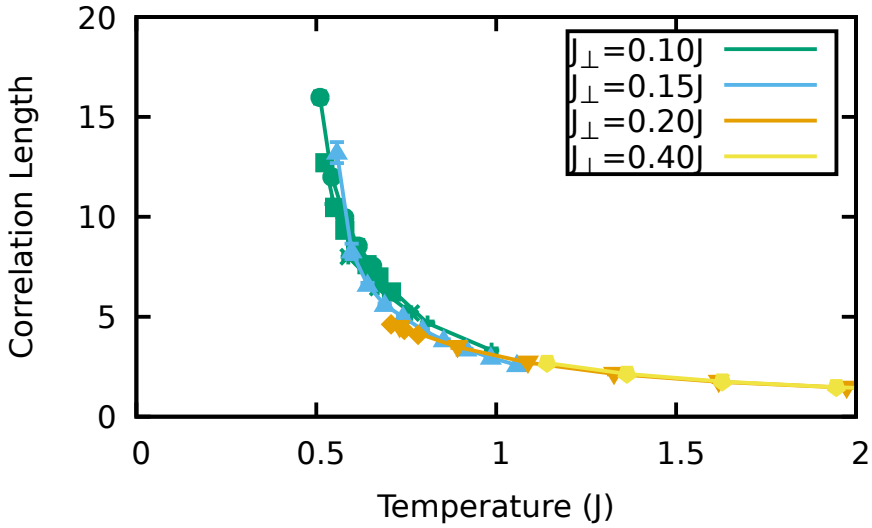

Figure 5.10: Correlation length, $\xi_\perp$, as a function of temperature for various values of $J_\perp$ in the *abab* stacking, obtained by fitting to the functional form given in Eq. (5.22).

of the data for small values of $J_\perp/J$, where the maximum in the structure factor lies on a circle, but it does not capture the triangular distortions for larger $J_\perp/J$ that are apparent in the left-most panel of Fig. 5.9. As shown in Fig. 5.10, and as for the *abc* stacking, the resulting values of $\xi_\perp$ increase rapidly with decreasing temperature but vary little with $J_\perp$.

5.4.3 Fitting Procedure

Here we discuss in further detail our Monte Carlo results for $S(\mathbf{q})$ and the fitting procedures used to analyse them.

As a simple check, we start by considering uncoupled layers, which are expected to display power-law correlations at low temperature with $S(\mathbf{K}+\mathbf{q}) \sim q^{-3/2}$. The behaviour illustrated in Fig. 5.11 matches this quite accurately. As we will see below, interlayer interactions produce significant changes in $S(\mathbf{q})$, and no clear remnant of the 3/2 power law is identifiable even for the smallest values of $J_\perp/J$ that we have investigated. Instead, we find for non-zero $J_\perp$ that $S(\mathbf{q})$ is well-represented using Lorenztian functions of wave vector.

First, we consider the details for the *abc* stacking. The data displayed in Fig. 5.6

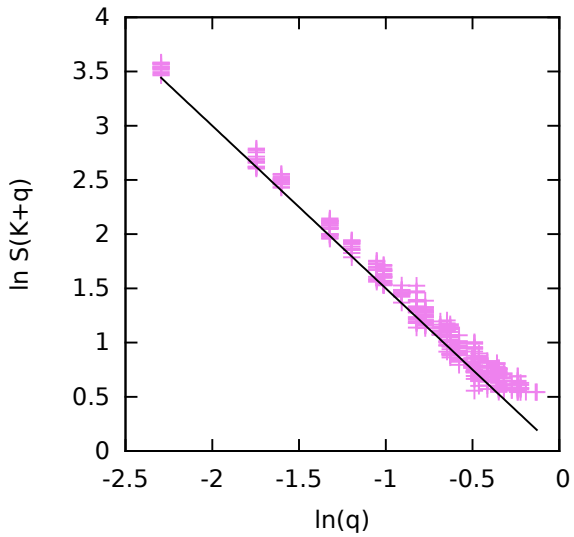

Figure 5.11: Illustration of power-law behaviour without interlayer coupling: line has slope $-\frac{3}{2}$; system parameters are $L = 72$ and $T = 0.31J$.

show helices of high intensity with axes passing through the K-points of the triangular-lattice Brillouin zone. In broad terms, we extract the correlation length $\xi_\perp$ and the helix radius Q by analysing simulation results for $\mathrm{S}(\mathbf{q})$ separately at each q_z, and fitting data near the maximum to a sum of Lorentzian contributions, one from each helix that intersects the plane.

In detail, we consider values of $S(\mathbf{q})$ at fixed q_z with (q_x, q_y) spanning one Brillouin zone. To focus on the maxima, we retain the N largest values of $S(\mathbf{q})$ from a total of L^2 points within each q_z-plane. If N is too large, some points are included that are too far in reciprocal space from the helix to be well-represented by the fitting function; if N is too small, statistical accuracy is sacrificed. Results are insensitive to the choice of N in the range $20 \leq N \leq 200$, and we use $N = 50$. Referring to Fig. 5.12, the form of $S(\mathbf{q})$ near the K-points labelled a and b should be dominated by helices with their axes passing through these K-points, but may also be influenced by helices with axes passing through the four K-points c – f if the helix radius is large. Our fitting function therefore includes six terms, labelled by i,

$$F_{4nn}(\mathbf{q}_\perp) = \sum_i \frac{I}{\xi_\perp^2 \left(\mathbf{q}_\perp - \mathbf{q}_{\perp,i}\right)^2 + 1}. \tag{5.23}$$

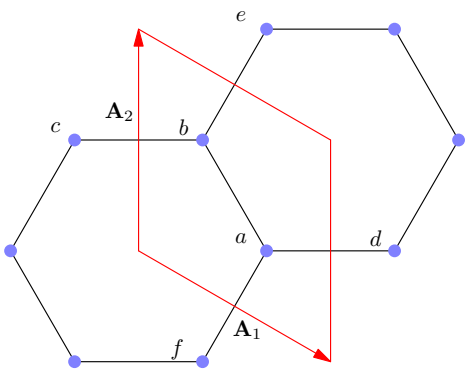

Figure 5.12: Brillouin zone for the triangular lattice, with K-points labelled a–f.

We can fit the results of Monte Carlo simulations for the structure factor to peaks located at sites labelled a and b, as well as the four peaks closest to those, c, d, e, and f. In order to reduce the number of parameters being fit, we assume that the peaks at c, d, e, and f are identical to a and b, up to a phase. To make this more clear, consider decomposing $\mathbf{q}_a$ into $\mathbf{q}_{a,0} + \boldsymbol{\delta} q_a$, where $\mathbf{q}_{a,0}$ points to the corner a and $\boldsymbol{\delta} q_a$ is the displacement from the corner.

Then, for example, we could write:

$$q_{x,e} = \cos\theta_e (\boldsymbol{\delta} q_a)_x - \sin\theta_e (\boldsymbol{\delta} q_a)_y + (\boldsymbol{q}_{a,0})_x + (\mathbf{A}_2)_x \tag{5.24}$$

$$= \cos\theta_e \left[(\mathbf{q}_a)_x - (\mathbf{q}_{a,0})_x\right] - \sin\theta_e \left[(\mathbf{q}_a)_y - (\mathbf{q}_{a,0})_y\right] + (\mathbf{q}_{a,0})_x + (\mathbf{A}_2)_x \tag{5.25}$$

where θ_e is given by the difference in φ_0 for a and e, i.e. $\frac{4\pi}{3} - 0$. The sine/cosine terms encode the fact that we assume the e peak is simply rotated about the corner relative to the a peak, which is additionally shifted to the e corner by the last term.

We can also use symmetry to relate the helices centred on a and b. The coordinates of the b peak will be the same as those at a, but reflected across $\mathbf{A}_1 + \mathbf{A}_2$. As this vector makes a 30° angle with the horizontal, we can write the reflection matrix as

$$\begin{pmatrix} \frac{1}{2} & \frac{\sqrt{3}}{2} \\ \frac{\sqrt{3}}{2} & -\frac{1}{2} \end{pmatrix} \tag{5.26}$$

This means we can easily rewrite the location of all the corners using the coordinates

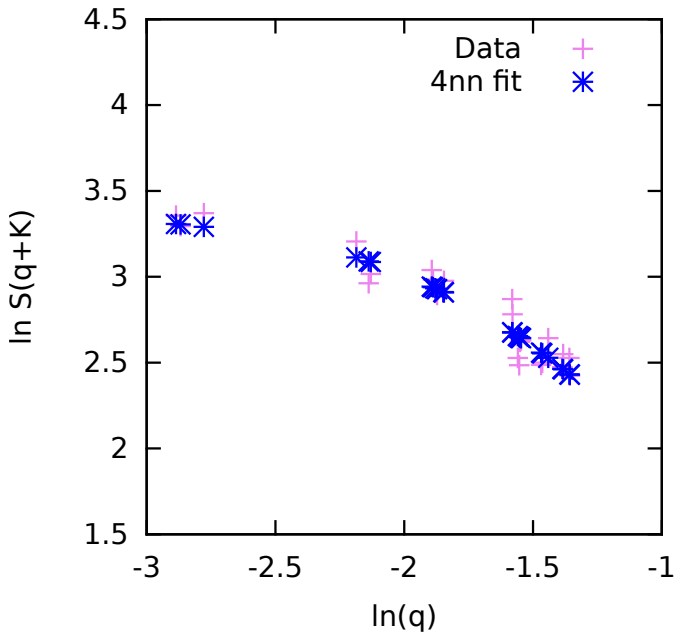

Figure 5.13: Comparison of F_{4nn} with data for $L = 72, L_z = 12$, $J_\perp = 0.2J$, $T = 0.8J$ in the *abc* stacking.

of a single one:

$$q_{x,b} = \frac{1}{2} \cdot q_{x,a} + \frac{\sqrt{3}}{2} \cdot q_{y,a}, \tag{5.27}$$

$$q_{y,b} = \frac{\sqrt{3}}{2} \cdot q_{x,a} - \frac{1}{2} \cdot q_{y,a}. \tag{5.28}$$

So we can perform the fitting with only four parameters: I_a, ξ_a, $q_{x,a}$, $q_{y,a}$. The quality of fit we obtain in this way is illustrated in Fig. 5.13. In principle, one expects $S(\mathbf{q})$ to be characterised by two distinct correlation lengths, $\xi_\perp$ and ξ_z, as we will discuss in Chapter 7. In practice, we have been unable to extract a second correlation length from our Monte Carlo data for the *abc* stacking, for reasons we now discuss. Consider first the ideal form of correlations, reached in the limit of divergent correlation lengths

$$S_{\text{ideal}}(\mathbf{q}) = \delta\left(q_x - q_x^0(q_z)\right) \delta\left(q_y - q_y^0(q_z)\right) . \tag{5.29}$$

The consequences of finite correlation lengths can be represented by convolving $S_{\text{ideal}}(\mathbf{q})$ with a form factor that is characterised by its width in two directions transverse to the line $q_x^0(q_z)$, $q_y^0(q_z)$. The fitting function $F_{4nn}(\mathbf{q}_\perp)$ corresponds to a choice

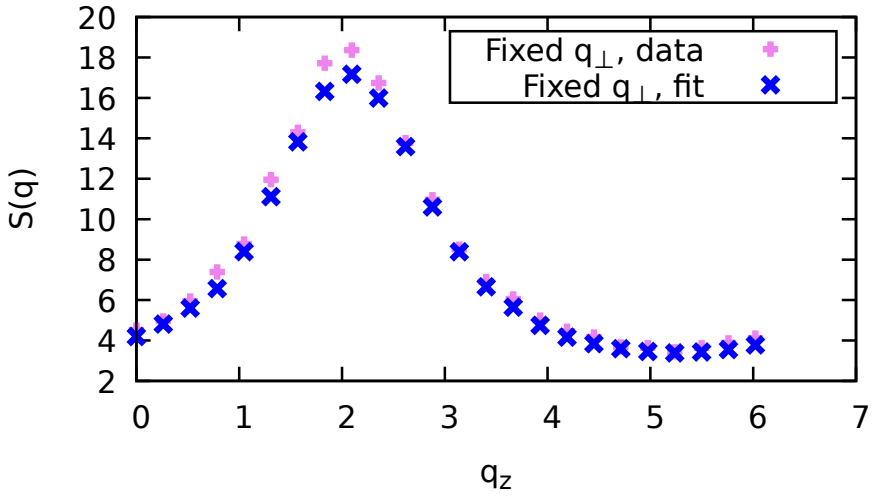

Figure 5.14: $S(\mathbf{q})$ vs q_z for fixed q_x, q_y in the *abc* stacking, comparing data and fitting function. $J_\perp = 0.1J$, $L = 36, L_z = 48$, $T = 0.56J$.

for this form factor that has circular contours in the q_x–q_y plane. More general possibilities have elliptical contours; we have made fits of this type, but find they do not show significant in-plane anisotropy. As a demonstration that the form $F_{4nn}(\mathbf{q}_\perp)$ is an adequate representation of our data, we show in Fig. 5.14 a comparison of it with Monte Carlo data, as a function of q_z at fixed q_x, q_y, on a line passing through the helix. The close match indicates that the broadening within the q_x–q_y plane that is contained in $F_{4nn}(\mathbf{q}_\perp)$ also accounts for the broadening of the helix along q_z.

For the *abab* stacking, our fitting of $S(\mathbf{q})$ as a function of q_x and q_y follows similar steps to the ones used for the *abc* stacking, but analysis of the dependence on q_z has new features. For this stacking the peak width of $S(\mathbf{q})$ as a function of q_z yields directly the interlayer correlation length ξ_z. An example of a fit is shown in Fig. 5.15 and the resulting values of ξ_z are displayed as a function of $J_\perp$ and T in Fig. 5.16. We can see from these plots that the interlayer correlation length is certainly larger than the spacing between two layers and increases steeply as the system parameters move deeper into the classical spin-liquid regime, i.e. weak interlayer coupling and low temperature.

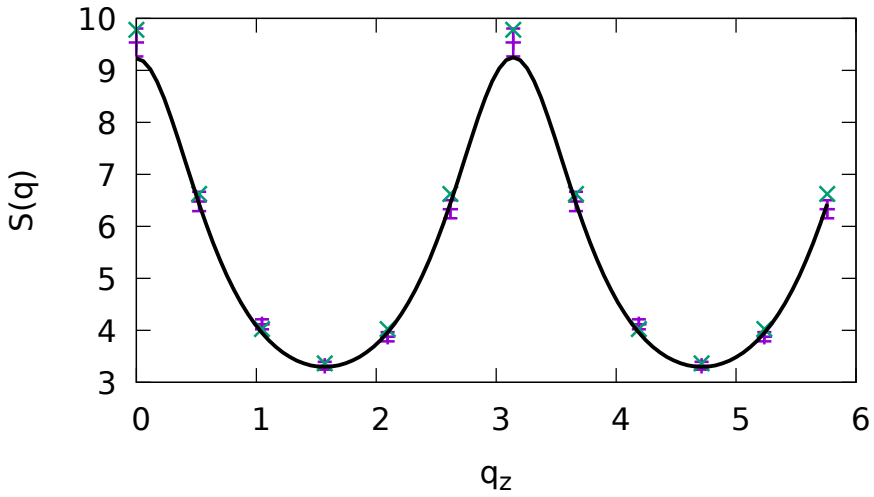

Figure 5.15: $S(\mathbf{q})$ vs q_z, for fixed q_x, q_y passing through the maximum, in the *abab* stacking: data (red); fit to SCGA (green); sum of Lorentzians (black). $J_\perp = 0.20J, T = 0.73J$.

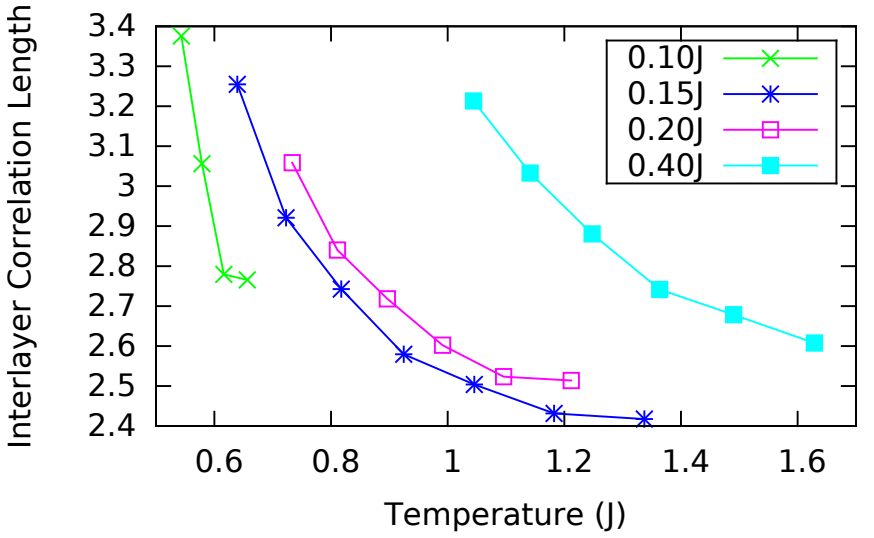

Figure 5.16: ξ_z vs T for different values of $J_\perp$ in the *abab* stacking. The unit of length is the spacing between successive a-layers.

5.5 Comparison with self-consistent Gaussian approximation

The SCGA provides a useful description of frustrated magnets in the strongly correlated regime. In particular, it offers a simple theoretical prediction for $S(\mathbf{q})$, which we now show to be a good representation of our simulation data. We use the functional form of Eq. (4.31) in two ways, which are distinct in principle but yield very similar results. One of these treats the variable λ as a fitting parameter with respect to simulations; the other uses the SCGA self-consistency condition.

The self-consistency constraint in the SCGA fixes the parameter λ in the expression for the correlations. This parameter is directly related to the correlation length and we can make comparisons with the numerics. The self-consistency equation is:

$$1 = \frac{1}{N}\mathrm{Tr}\left(\beta\mathbf{J} + \lambda\mathbf{1}\right)^{-1} \approx \frac{1}{\Omega_{BZ}}\int_{BZ} d^3\mathbf{q} \sum_l \frac{u_{\mathbf{q}}^{l*} u_{\mathbf{q}}^{l}}{\epsilon_{\mathbf{q}}^{l}\left(\lambda\right)} \tag{5.30}$$

where $u_{\mathbf{q}}^{l}$ are the eigenvectors of $J_{\mathbf{q}}$. We can solve this equation numerically by carrying out the integral with Monte Carlo methods for closely spaced values of λ and using the method of bisection to solve for λ.

We now compare the two methods of extracting correlation length. The results for $\xi_\perp$ are shown in Fig. 5.17. They agree to $\sim 10\%$ with those obtained by fitting the functional forms given in Eq. (5.19) and Eq. (5.22) for the *abc* and *abab* cases respectively (see Figs. 5.7a and 5.10). Alternatively, the value of λ can be determined without reference to simulations, using the SCGA condition, yielding a theoretical prediction for $\xi_\perp$. From Fig. 5.17, it is apparent that both approaches to determining λ yield very similar results.

The SCGA form for $S(\mathbf{q})$ is especially helpful at larger values of $J_\perp/J$, when detailed lattice effects are important. The results of these lattice effects for the *abc* stacking include dependence of the helix radius [$\mathbf{q}_\perp^0(q_z)$ in Eq. (5.19)] on q_z. For the *abab* stacking they generate correlations that are not represented using the circular maximum in $S(\mathbf{q})$ implied by the fitting function given in Eq. (5.22). The SCGA describes this physics well. Notably, for the *abab* stacking the SCGA fits are effective

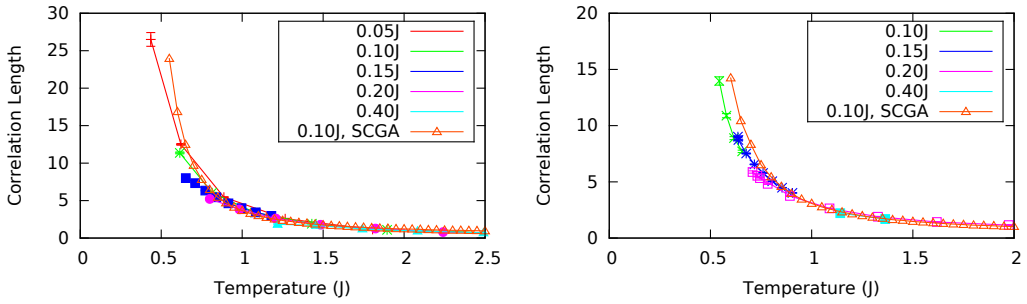

Figure 5.17: Correlation length $\xi_\perp$ as a function of temperature for various values of $J_\perp$ as obtained from the SCGA. Left: abc stacking. Right: abab stacking. The data labelled 'SCGA' have been derived by imposing the condition $\langle|\sigma|^2\rangle = 1$ while the variable λ is used as a fitting parameter in the other curves.

in capturing the triangular distortion of the rings, as demonstrated in Fig. 5.18.

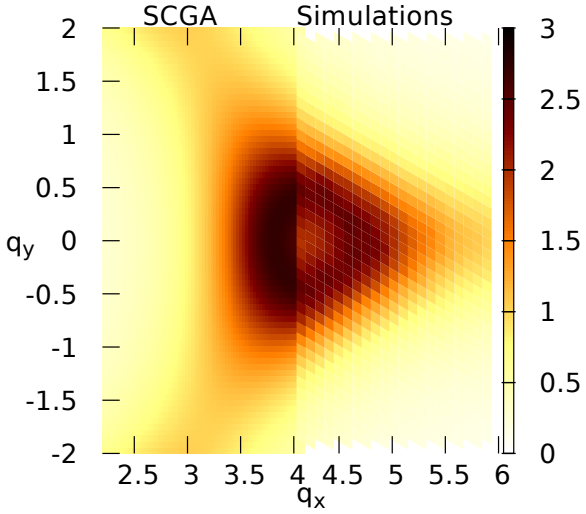

Figure 5.18: Comparison of SCGA and simulation results for $S(\mathbf{q})$ in the *abab* stacking. $J_\perp = 0.4J$, $T = 1.36J$.

In this chapter, we have seen that the parallel tempering Monte Carlo simulations provide evidence that strongly supports the existence of a classical spin-liquid regime in the frustrated STLIAFMs. This evidence is both qualitative, in the form of sharp features in the structure factor, and quantitative, in the form of steeply increasing correlation lengths.

Chapter 6

Height Models

We now turn to an analytical treatment of stacked triangular lattice Ising antiferromagnets. Although the SCGA, as demonstrated, provides a good approximate description, it is formally correct only for n-component spins in the large-n limit. It is therefore not a natural starting point for a systematic approach. By contrast, the height model provides a representation of a single-layer TLIAFM that is known to capture exactly the physics at low temperatures and long distances.

The models we are interested in originate in studies of crystal interfaces and solid-on-solid (SOS) models. We focus on the height models first articulated by Blöte et al. that can be used to describe frustrated magnets. Although we will not explore them here, SOS models and, more broadly, surface growth have been and continue to be areas rich with highly diverse and novel physics.

The height model will provide a mapping between ground states of the TLIAFM and a scalar field in two dimensions. The route from spins to heights is somewhat circuitous and relies on various conventions which we will motivate here, following the original work by Blöte et al.[29].

Starting from a ground state configuration on the TLIAFM, we have triangles that consist of two satisfied antiferromagnetic bonds and one unsatisfied bond. Now consider erasing the frustrated bonds. One can view the resulting figure as the irregular surface of a cubic lattice from the $(1, 1, 1)$ perspective. From here, one can write down a convention for assigning heights to the points on this surface. The convention is shown in the table for the different bonds. This is the original mapping between the TLIAFM spins and heights of a surface. In this work, however, we will formulate

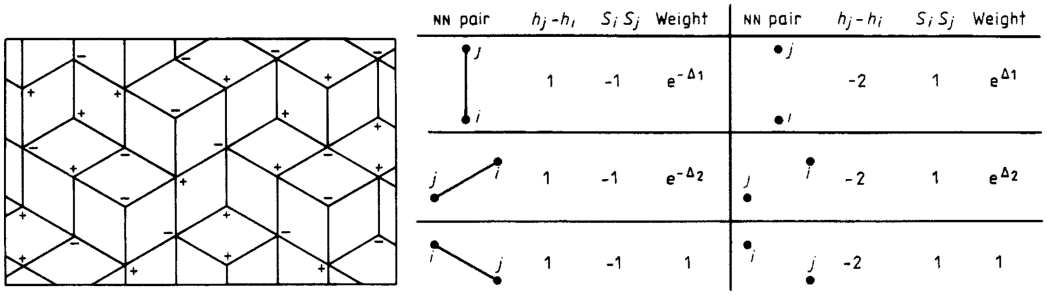

Figure 6.1: Figure from [29]. Example of conventions for defining discrete heights on the sites of the triangular lattice Ising antiferromagnet.

different (but equivalent) conventions for describing this mapping.

6.1 Triangular Lattice Ising Antiferromagnet (TLIAFM)

Following Zeng and Henley [30], we map ground states of a single layer Ising model onto states of a height model. We reformulate the conventions for the mapping presented by Blöte *et al.* in an equivalent way that will be more convenient.

The mapping is done in such a way that spin configurations with long-range three-sublattice order correspond to "flat" height configurations, where "flat" will be defined more clearly in the rest of this section. Because of frustration, domain walls can be introduced without energy cost between regions with different types of three-sublattice order. These domain walls correspond to steps in the height field. In a coarse-grained description, steps are represented by a gradient in the height field, and a large value for this gradient carries an entropy penalty.

The mapping is described in two stages. First, we define heights at the sites of the triangular lattice, as in [29]. Second, following [30], we average these site heights to define heights at the centres of triangles, obtaining a height model that is easily coarse-grained.

Explicitly, the procedure we have in mind for the height mapping is given as follows. We consider ground state configurations of spins in the TLIAFM. Starting from a reference spin, the height at the origin is $h = 0$. The convention for heights at

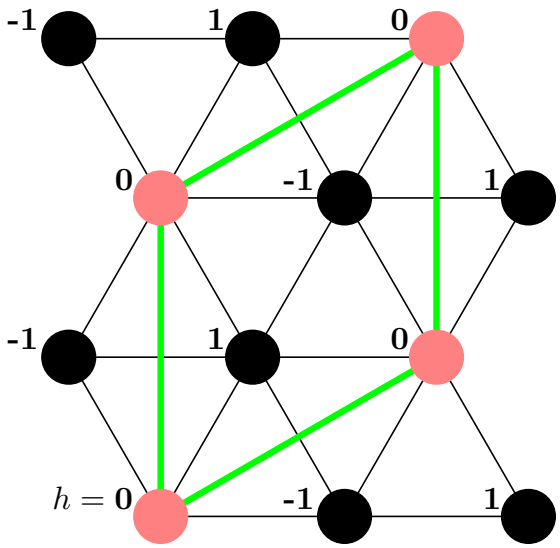

Figure 6.2: An example of a spin configuration with height labels following the convention: starting from a reference spin, the height at the origin is $h = 0$. The convention for heights at all other lattice points is given by: $h_j = h_i + 2$ when the bond from i to j, traversed anti-clockwise (clockwise) on an upward(downward)-pointing triangle, has $\sigma_i = \sigma_j$ and $h_j = h_i - 1$ when $\sigma_i = -\sigma_j$.

all other lattice points is given by: $h_j = h_i + 2$ when the bond from i to j, traversed anti-clockwise (clockwise) on an upward(downward)-pointing triangle, has $\sigma_i = \sigma_j$ and $h_j = h_i - 1$ when $\sigma_i = -\sigma_j$. This mapping is demonstrated in Fig. 6.2.

The next step is defining heights on the centres of triangles instead of on the lattice sites. This will have two advantages: first, it allows a more straightforward coarse-graining. Second, it reveals some intuition about the various types of ground states in the TLIAFM.

To define the heights on triangle centres, we first make note of the three-sublattice structure of the triangular lattice. We can label these A, B, and C sublattices. There are six configurations which are ordered on the sublattices. However, following the procedure above for heights on the corners and then averaging to define heights on the centres fails to distinguish between all six sublattice-ordered configurations. The additional convention needed to distinguish these is described below.

We define heights at the corners of triangles and the centres modulo 6. Then, we pick a convention for labelling these states; see Table 6.1. This convention indicates

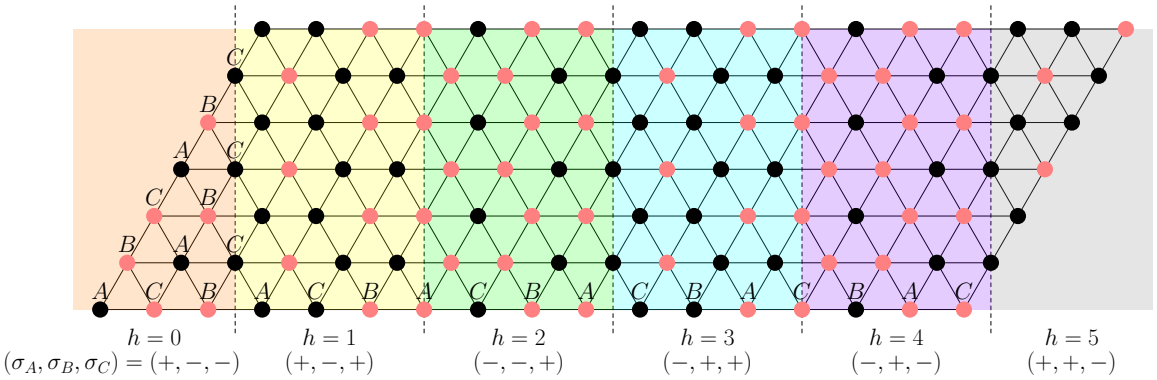

Figure 6.3: Sample of spin configuration that displays all six different flat states; black is $+$, red is $-$. These flat states are related by single-sublattice spin-flips.

$h = \frac{1}{3}(h_A + h_B + h_C)$	h_A	h_B	h_C	σ_A	σ_B	σ_C
0	0	1	-1	$+$	$-$	$-$
1	0	1	2	$+$	$-$	$+$
2	3	1	2	$-$	$-$	$+$
3	3	4	2	$-$	$+$	$+$
4	3	4	5	$-$	$+$	$-$
5	6	4	5	$+$	$+$	$-$

Table 6.1: Heights defined at triangle centres (column 1) and at triangle corners (columns 2-4), for each ground state spin configuration (columns 5-7) of the triangle. The spin configuration determines the height configuration up to a global shift. The sublattice labelling is illustrated in Fig. 6.3.

that the height on every triangle is constant in each of these configurations, i.e. these configurations are flat and that each of the six sublattice-ordered configurations corresponds to a flat configuration with its own constant height modulo 6.

The convention can be motivated by Fig. 6.3. In that figure, we start from the configuration corresponding to $h = 0$ and see first that it is reasonable to label this configuration $h = 0$ because when averaging the sites for each triangle, one gets 0 everywhere. Second, we see that by flipping the spins on one sublattice, the height on each triangle should be incremented: $h \to h + 1$. Carrying out five successive single-sublattice spin-flips returns the configuration equivalent to $h = 0$ and so we make the identification that flat height configurations are identical modulo 6.

This mapping is unique up to the labelling of sublattices A, B and C. Rotations of

the labels by $2\pi/3$ around the centres of triangles (or equivalently a lattice translation) correspond to global shifts of the height field $h \to h+2$. A global spin-flip corresponds to a global shift of the height field $h \to h+3$. The other shifts $h \to h+1, 5$ can be obtained from combinations of the label permutations and global spin-flips.

We can also express the inverse mapping, from a height configuration to a configuration of Ising spins. The inverse mapping is given in terms of a periodic function, $f(h) = f(h+6)$, and a constant, s_α. $f(h)$ is $+1$ for $h = 0, 1, 5$ and -1 for $h = 2, 3, 4$. The constant s_α is indexed by the sublattices and has values: $s_A = 0, s_B = 2, s_C = -2$. The Ising spins are then given by $\sigma_\alpha = f(h + s_\alpha) = f_\alpha(h)$.

We note that each spin is part of six triangles and therefore the choice of which triangle's height is used must be unimportant for this mapping. Indeed, when the heights are integer-valued, and change by at most 1 between any pair of adjacent triangles, the mapping does not rely on this choice. For such integer-valued configurations, we can write the inverse mapping explicitly

$$f(h) = \frac{4}{3}\cos\left(\frac{\pi h}{3}\right) - \frac{1}{3}\cos\left(\pi h\right). \tag{6.1}$$

To motivate the next step in our construction of the height model, we consider the entropy of various ground states. In flat ground states, with constant height, there are macroscopically many "flippable" spins. These spins can be flipped from $+1$ to -1 without any energy cost. We contrast these with other ground states that have constant gradient. In these "tilted" configurations, there are zero flippable spins, see Fig. 6.4.

We can then write down an entropically motivated free energy to describe the statistical mechanics of the ground states of the TLIAFM [29]. The effective Hamiltonian for the system is

$$\mathcal{H} = \frac{K}{2}\int \mathrm{d}^2\mathbf{r}\,|\nabla h(\mathbf{r})|^2 + \int \mathrm{d}^2\mathbf{r}\,\tilde{V}(h). \tag{6.2}$$

The locking potential, $\tilde{V}(h) = -v\cos(2\pi h)$, arises because we must have microscopic heights which are integers.

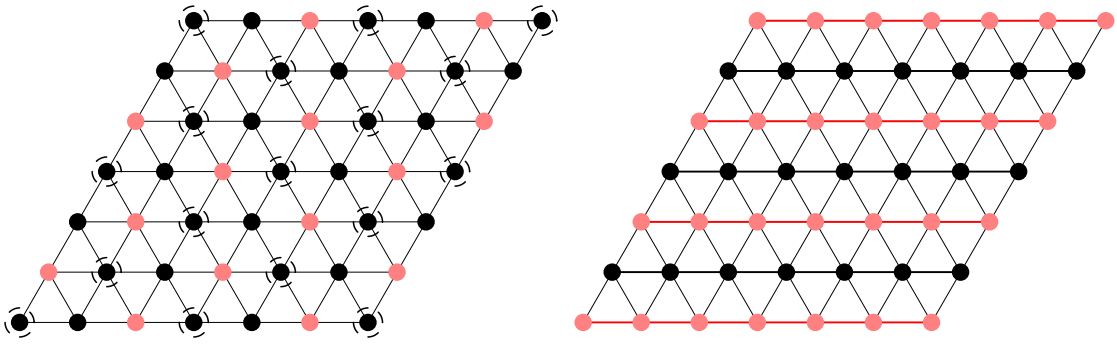

Figure 6.4: (left) An example of a flat ground-state configuration with flippable spins circled in dashed lines. (right) An example ground-state configuration without any flippable spins; black is +, red is −.

Armed with the phenomenological free energy, we can fix the stiffness by comparison with the exact solution. In particular, we consider the spin-spin correlation functions in the absence of a locking term.

To begin, we make our notation clear. Statistical expectation averages of observables will be written

$$\langle O \rangle = \frac{\int \mathcal{D}\left[h\right] O e^{-\beta \mathcal{H}}}{\int \mathcal{D}\left[h\right] e^{-\beta \mathcal{H}}}. \tag{6.3}$$

where $\mathcal{D}\left[h\right]$ denotes a functional integral over the scalar field $h\left(\mathbf{r}\right)$.

To fix the stiffness, we start with the form of the correlation function from the exact solution. Stephenson has shown that at long distances [11]

$$\langle \sigma_\alpha(\mathbf{r}) \sigma_\beta(\mathbf{r}') \rangle \sim \frac{\omega^s}{\sqrt{|\mathbf{r} - \mathbf{r}'|}} + \text{c. c.}\,, \tag{6.4}$$

where $s = (s_\alpha - s_\beta)/2$ and $\omega = e^{2\pi i/3}$, and c.c. stands for the complex conjugate. In that work, Stephenson used the Pfaffian representation of the partition function developed by Kasteleyn [12] and the approach to correlation functions developed by Montroll, Potts, and Ward [13].

Now we can also express this correlation function in terms of the height fields and evaluate the thermodynamic averages using the phenomenological free energy. The leading terms in the expression for the intra-sublattice spin-spin correlation function

in terms of the height fields are

$$\langle \sigma_\alpha(\mathbf{r})\,\sigma_\beta(\mathbf{r}')\rangle \sim \langle e^{i\frac{\pi}{3}[h(\mathbf{r})-h(\mathbf{r}')]}\rangle \omega^s + \text{c. c.} \tag{6.5}$$

$$= e^{-\frac{1}{2}\left(\frac{\pi}{3}\right)^2\langle[h(\mathbf{r})-h(\mathbf{r}')]^2\rangle}\omega^s + \text{c. c.}. \tag{6.6}$$

Note that we are ignoring the locking term in the potential in these expectations (we will see later that this turns out to be irrelevant). Carrying out the functional integral using our form of the effective Hamiltonian yields

$$\langle \sigma_\alpha(\mathbf{r})\,\sigma_\beta(\mathbf{r}')\rangle \sim \exp\left[-\frac{2\pi}{36K}\ln|\mathbf{r}-\mathbf{r}'|\right](\omega^s+\omega^{-s}) \tag{6.7}$$

$$\sim |\mathbf{r}-\mathbf{r}'|^{-\frac{2\pi}{36K}}(\omega^s+\omega^{-s}). \tag{6.8}$$

Hence at zero temperature, to reproduce the long-wavelength properties of the exact solution, we equate the expressions and match the scaling exponents

$$|\mathbf{r}-\mathbf{r}'|^{-1/2} = |\mathbf{r}-\mathbf{r}'|^{-\frac{2\pi}{36K}}, \tag{6.9}$$

and thus take $K = \pi/9$. This fixes the stiffness constant in our phenomenological theory.

However, there are still other aspects of this theory that should be noted and checked for consistency with what is known about the single-layer TLIAFM.

First, we have ignored the locking potential term in the effective Hamiltonian when calculating the above correlation functions. We can include such a potential, $\tilde{V}(h) = -v\cos(2\pi h)$, to account for the microscopic integer heights. At small length scales, integer heights are strongly preferred, so v is large and positive. However, at long distances, the effective value of v depends on the scaling dimension of the operator. We can deduce the scaling dimension from the two-point function. We have

$$\langle \cos(2\pi h(\mathbf{r}))\cos(2\pi h(\mathbf{r}'))\rangle \sim |\mathbf{r}-\mathbf{r}'|^{-\frac{2\pi}{K}} \tag{6.10}$$

$$\int d^2r\cos(2\pi h(\mathbf{r})) \sim L^{2-\frac{\pi}{K}}. \tag{6.11}$$

At $T = 0$, or when $K = \pi/9$, this yields the scaling dimension $2-\frac{\pi}{K} = -7$. Hence the effective value of the coefficient v decreases rapidly as we probe the system at longer

length-scales, and its effect on the long-wavelength correlations is negligible. Thus we are justified in neglecting the locking potential when using the long-wavelength theory to fix the stiffness.

Lastly, we can use the effective Hamiltonian formalism described so far to consider behaviour at finite temperatures. Doing so requires that we consider excitations in the height field. Excitations out of the ground states include configurations with three spins aligned in a single triangle. The mapping to a height model is not well-defined for these configurations. This is clear when we consider using the conventions from earlier to map a triangle with three aligned spins in the height mapping. Starting at $h = 0$ for one of the spins, we traverse only bonds with aligned spins and so cannot make the height field self-consistent.

Within the language of the effective Hamiltonian, we include these excitations as singularities in the height field and identify them as vortices. Once we have done this, the theory is equivalent to a 2D xy model at an effective temperature which is set by the stiffness, K.

In order to determine the role of vortices in these systems, we must consider the scaling dimension. The scaling dimension can be obtained from estimating the free energy of a vortex. We compute the free energy by considering the entropic and energetic contributions. There are $\frac{L^2}{a^2}$ locations for vortices and, from the effective Hamiltonian, each vortex contributes the following to the free energy

$$\delta\mathcal{H} = \frac{9K}{\pi} \ln\left(\frac{L}{a}\right). \tag{6.12}$$

The combined contribution to the free energy is then

$$\delta F = \left(\frac{9K}{\pi} - 2\right) \ln\left(\frac{L}{a}\right). \tag{6.13}$$

For increasing system size, L, this free energy depends on K and for $K = \pi/9$, the free energy is increasingly negative with system size. This favours the creation of vortices and therefore we are in the high-temperature regime of the xy model in which vortices are unbound. The vortex density is set by the fugacity associated with

the excitation energy of a vortex. The density sets the correlation length and this reflects the fact that the TLIAFM is a paramagnet at any finite temperature.

We have now seen how the height model presented captures the phase diagram and correlations for the TLIAFM. In particular, the locking potential is irrelevant at long wavelengths and the vortices that arise at $T > 0$ are relevant and make the system paramagnetic at finite temperature.

Next, we use the height model to construct a description of the multilayer system that allows for a controlled treatment of weak interlayer interactions.

6.2 Coupled Height Models

We move now to the cases of primary interest for this work. These are extensions of the height model described above for the stacked TLIAFM. This description will be applicable in the weakly coupled layers case.

As with a single layer, we rely on the single harmonic mapping from spins to heights. It is instructive to begin by studying the unfrustrated stacking. For the *aaa* stacking, the interlayer coupling is

$$J_\perp \left(\sigma_{A,z}\sigma_{A,z+1} + \sigma_{B,z}\sigma_{B,z+1} + \sigma_{C,z}\sigma_{C,z+1}\right) = \frac{8J_\perp}{3}\cos\left(\delta_1 h_z\right) + \frac{J_\perp}{3}\cos\left(\pi h_z\right)\cos\left(\pi h_{z+1}\right) + \ldots \tag{6.14}$$

where $\ldots$ represents terms of quadratic and higher order in the derivatives. These terms arise when considering higher harmonic terms in $f\left(h\right)$, but we drop them here as they turn out to be irrelevant in the scaling sense. We also introduce the notation

$$\delta_p h_z(\mathbf{r}) \equiv \frac{\pi}{3}[h_{z+p}(\mathbf{r}) - h_z(\mathbf{r})]. \tag{6.15}$$

The most relevant term is $\cos\left(\delta_1 h_z\right)$. The scaling dimension can again be obtained from terms in the two-point function

$$\langle \cos\left(\delta_1 h_z\right)\cos\left(\delta_1 h'_z\right)\rangle \sim |\mathbf{r} - \mathbf{r}'|^{-\frac{\pi}{9K}} \tag{6.16}$$

$$\int d^2 r \cos\left(\delta_1 h_z\right) \sim L^{2-\frac{\pi}{18K}}. \tag{6.17}$$

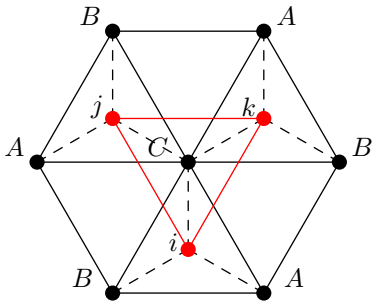

Figure 6.5: Interactions between layer z and $z+1$. Dashed lines represent interactions between adjacent layers. A, B, C label sublattices in layer z; i, j, k label sites in layer $z+1$.

The above indicates a scaling dimension of $\frac{3}{2}$ for $K = \pi/9$. The term $\cos(\pi h_z)\cos(\pi h_{z+1})$ has scaling dimension $-\frac{5}{2}$ and can be neglected.

Hence the effective Hamiltonian of the height model for the *aaa* stacking is

$$\mathcal{H}^{(aaa)} = \frac{K}{2}\sum_z \int d^2r\{|\nabla h_z(\mathbf{r})|^2 + \kappa_3 \cos(\delta_1 h_z)\}, \tag{6.18}$$

with $\kappa_3 = 16\beta J_\perp/3K$. The ground states of this effective model are

$$h_z(\mathbf{r}) = \gamma, \tag{6.19}$$

for constants γ. These ground states have a $U(1)$ symmetry under changes of γ. This symmetry is broken down to a six-fold discrete symmetry by the interaction $\tilde{V}(h)$. This interaction is irrelevant in the scaling sense at the fixed point describing uncoupled layers.

For both the *abc* and the *abab* stackings, we consider two neighbouring layers as shown in Fig. 6.5. There is a coupling between each site on the red lattice and the three sites around it from an up-triangle on the black lattice, or equivalently between each site on the black lattice and the three sites around it from a down triangle on the red lattice. We denote heights on the red lattice by $h_{z+1}(\mathbf{r})$, and ones on the black lattice by $h_z(\mathbf{r})$. We will group the contributions by the three black up-triangles.

We can map the interlayer contribution to the Hamiltonian, below, to the analogous term in the continuum free-energy in terms of the height field

$$H_\perp = J_\perp \sum_{\{ij\},z} \sigma_{i,z}\sigma_{j,z+1}. \tag{6.20}$$

To carry out the mapping, we first use the fact that the mapping has period 6. This means we can expand as

$$\sigma(\mathbf{r}) = \sum_{\ell \in \mathbb{Z}} F_\ell e^{\frac{2\pi i \ell}{6} h(\mathbf{r})}. \tag{6.21}$$

When considering the coarse-grained theory, we only consider the most relevant Fourier components, ℓ. Higher order components are less relevant so we take

$$\sigma(\mathbf{r}) \sim C_1 \cos\left(\frac{\pi}{3} h(\mathbf{r})\right), \tag{6.22}$$

where we have accounted for the fact that the spins are real and have neglected the higher components.

We consider the sublattice dependence of the spin-height mapping to write

$$\sigma(\mathbf{r}_\alpha) \approx C_1 \cos\left(\frac{\pi}{3}\left[h(\mathbf{r}_\alpha) + s_\alpha\right]\right), \tag{6.23}$$

$$s_A = 0, s_B = 2, s_C = -2. \tag{6.24}$$

Another approximation that will be useful in writing out these interactions explicitly is the expansion of $h(\mathbf{r})$

$$h(\mathbf{r} + \mathbf{c}) \approx h(\mathbf{r}) + \mathbf{c} \cdot \nabla h(\mathbf{r}). \tag{6.25}$$

Using these expressions, we can write a more detailed mapping between the spins and heights which includes the sublattice differences and coarse-graining. We denote the centre of a triangle by $\mathbf{r}_0$ and a lattice vector from $\mathbf{r}_0$ to sublattice α by ϵ_α. The mapping is then

$$\begin{aligned}
\sigma_z(\mathbf{r}_\alpha) &\approx C_1 \cos\left(\frac{\pi}{3}\left[h_z(\mathbf{r}_0 + \epsilon_\alpha) + s_\alpha\right]\right) && (6.26)\\
&\approx C_1 \cos\left(\frac{\pi}{3}\left[h_z(\mathbf{r}_0) + \epsilon_\alpha \cdot \nabla h_z(\mathbf{r}_0) + s_\alpha\right]\right) && (6.27)\\
&= C_1 \left[\cos\left(\frac{\pi}{3}\left[h_z(\mathbf{r}_0) + s_\alpha\right]\right) \cos\left(\frac{\pi}{3}\epsilon_\alpha \cdot \nabla h_z(\mathbf{r}_0)\right)\right. && (6.28)\\
&\quad \left. - \sin\left(\frac{\pi}{3}\left[h_z(\mathbf{r}_0) + s_\alpha\right]\right) \sin\left(\frac{\pi}{3}\epsilon_\alpha \cdot \nabla h_z(\mathbf{r}_0)\right)\right].
\end{aligned}$$

We now assume that any appearance of h_z or h_{z+1} refers to the height at $\mathbf{r}_0$. Additionally, we can use the fact that the lattice spacing is small in the continuum limit

to approximate this as:

$$\sigma_z(\mathbf{r}_\alpha) \approx C_1 \left[\cos\left(\frac{\pi}{3}[h_z + s_\alpha]\right) - \frac{\pi}{3}\epsilon_\alpha \cdot \nabla h_z \sin\left(\frac{\pi}{3}[h_z + s_\alpha]\right)\right]. \tag{6.29}$$

We can apply this mapping to a specific set of the interaction terms and then sum over these terms. We consider three sites in layer z that compose a triangle and the site in layer $z+1$ that they each interact with.

To start, we note that we fix the sublattice so that in an upward triangle with the top vertex labelled sublattice-A, the other two are in clockwise order, so the bottom right is sublattice-B and the bottom left is sublattice-C. In Fig. 6.5, we start with the black upward pointing triangle centred on j and the associated interlayer interaction terms. The next step is to consider the other two triplets of interaction terms grouped around i, k in Fig. 6.5.

One of those trios is centred on $\sigma_{z+1}(\mathbf{r}_k) = \sigma_{z+1}(\mathbf{r}_j + \mathbf{a}_1)$ and the other is centred on $\sigma_{z+1}(\mathbf{r}_i) = \sigma_{z+1}(\mathbf{r}_j + \mathbf{a}_1 - \mathbf{a}_2)$. In the language of the lattice spacing used here, the vectors $\mathbf{a}_1 = (1, 0)$ and $\mathbf{a}_2 = \left(\frac{1}{2}, \frac{\sqrt{3}}{2}\right)$.

We start with the interactions around site j

$$J_\perp \sigma_{z+1}(\mathbf{r}_j)\left[\sigma_z(\mathbf{r}_j + \mathbf{e}_3) + \sigma_z(\mathbf{r}_j + \mathbf{e}_2) + \sigma_z(\mathbf{r}_j + \mathbf{e}_1)\right]. \tag{6.30}$$

Here, the displacement from the centre of the triangle is given by

$$\mathbf{e}_1 = \left(0, \frac{2\sqrt{3}}{6}\right) = \frac{2}{3}\mathbf{a}_2 - \frac{1}{3}\mathbf{a}_1, \tag{6.31}$$

$$\mathbf{e}_2 = \left(\frac{1}{2}, -\frac{\sqrt{3}}{6}\right) = \frac{2}{3}\mathbf{a}_1 - \frac{1}{3}\mathbf{a}_2, \tag{6.32}$$

$$\mathbf{e}_3 = \left(-\frac{1}{2}, -\frac{\sqrt{3}}{6}\right) = -\frac{1}{3}\mathbf{a}_1 - \frac{1}{3}\mathbf{a}_2. \tag{6.33}$$

Each of the interaction terms can be written using the expression above (note that

h_z, h_{z+1} are implicitly at $\mathbf{r}_j$)

$$\sigma_{z+1}(\mathbf{r}_j) = \cos\left(\frac{\pi}{3}[h_{z+1} + s_j]\right), \tag{6.34}$$

$$\sigma_z(\mathbf{r}_j + \mathbf{e}_3) = \cos\left(\frac{\pi}{3}[h_z + s_A]\right) - \frac{\pi}{3}\mathbf{e}_3 \cdot \nabla h_z \sin\left(\frac{\pi}{3}[h_z + s_A]\right), \tag{6.35}$$

$$\sigma_z(\mathbf{r}_j + \mathbf{e}_2) = \cos\left(\frac{\pi}{3}[h_z + s_C]\right) - \frac{\pi}{3}\mathbf{e}_2 \cdot \nabla h_z \sin\left(\frac{\pi}{3}[h_z + s_C]\right), \tag{6.36}$$

$$\sigma_z(\mathbf{r}_j + \mathbf{e}_1) = \cos\left(\frac{\pi}{3}[h_z + s_B]\right) - \frac{\pi}{3}\mathbf{e}_1 \cdot \nabla h_z \sin\left(\frac{\pi}{3}[h_z + s_B]\right). \tag{6.37}$$

Using the fact that the cosine terms contribute 0 altogether, we can write

$$\sigma_{z+1}(\mathbf{r}_j)\left[\sigma_z(\mathbf{r}_j + \mathbf{e}_3) + \sigma_z(\mathbf{r}_j + \mathbf{e}_2) + \sigma_z(\mathbf{r}_j + \mathbf{e}_3)\right] \tag{6.38}$$

$$= -\frac{\pi}{3}\cos\left(\frac{\pi}{3}[h_{z+1} + s_j]\right)\nabla h_z \cdot \left[\mathbf{e}_3 \sin\left(\frac{\pi}{3}[h_z + s_A]\right)\right. \tag{6.39}$$

$$\left. + \mathbf{e}_2 \sin\left(\frac{\pi}{3}[h_z + s_C]\right) + \mathbf{e}_1 \sin\left(\frac{\pi}{3}[h_z + s_B]\right)\right].$$

The terms $\mathbf{e}_n \cdot \nabla h_z$ are

$$\mathbf{e}_3 \cdot \nabla h_z = \left(-\frac{1}{2}\partial_x h_z - \frac{\sqrt{3}}{6}\partial_y h_z\right), \tag{6.40}$$

$$\mathbf{e}_2 \cdot \nabla h_z = \left(\frac{1}{2}\partial_x h_z - \frac{\sqrt{3}}{6}\partial_y h_z\right), \tag{6.41}$$

$$\mathbf{e}_1 \cdot \nabla h_z = \left(\frac{2\sqrt{3}}{6}\partial_y h_z\right). \tag{6.42}$$

We write the $\partial_x h_z$ and $\partial_y h_z$ terms separately

$$\partial_x : \frac{\pi}{6}\partial_x h_z \cos\left(\frac{\pi}{3}[h_{z+1} + s_j]\right)\left[\sin\left(\frac{\pi}{3}[h_z + s_A]\right) - \sin\left(\frac{\pi}{3}[h_z + s_C]\right)\right], \tag{6.43}$$

$$\partial_y : \frac{\pi\sqrt{3}}{18}\partial_y h_z \cos\left(\frac{\pi}{3}[h_{z+1} + s_j]\right)\left[\sin\left(\frac{\pi}{3}[h_z + s_A]\right)\right. \tag{6.44}$$

$$\left. + \sin\left(\frac{\pi}{3}[h_z + s_C]\right) - 2\sin\left(\frac{\pi}{3}[h_z + s_B]\right)\right].$$

We can consider the other triplets of interactions using analogous expressions for the height mapping. It is clear that we need to sum over hexagons that include these three triangles to sum over the entire plane. We can write all the ∂_x and ∂_y terms together. By grouping these terms appropriately, we can use the sum of cosines again to cancel some terms

$$\partial_x : \frac{\pi}{6}\partial_x h_z \left(\cos\left(\frac{\pi}{3}[h_{z+1} + s_k]\right)\left[-3\sin\left(\frac{\pi}{3}[h_z + s_B]\right)\right]\right. \tag{6.45}$$

$$\left. + \cos\left(\frac{\pi}{3}[h_{z+1} + s_j]\right)\left[3\sin\left(\frac{\pi}{3}[h_z + s_A]\right)\right]\right),$$

$$\partial_y : \frac{\sqrt{3}\pi}{18}\partial_y h_z \left(\cos\left(\frac{\pi}{3}\left[h_{z+1}+s_i\right]\right)\left[3\sin\left(\frac{\pi}{3}\left[h_z+s_B\right]\right)+3\sin\left(\frac{\pi}{3}\left[h_z+s_A\right]\right)\right]\right. \tag{6.46}$$
$$+\cos\left(\frac{\pi}{3}\left[h_{z+1}+s_k\right]\right)\left[-3\sin\left(\frac{\pi}{3}\left[h_z+s_A\right]\right)\right]$$
$$\left.+\cos\left(\frac{\pi}{3}\left[h_{z+1}+s_j\right]\right)\left[-3\sin\left(\frac{\pi}{3}\left[h_z+s_B\right]\right)\right]\right).$$

Using the convention $s_A = 0, s_B = 2, s_C = -2$, we need to fix a convention for the above layer as well. Here we use $s_i = -2, s_j = 2, s_k = 0$. Together, these give

$$\frac{3\pi}{6}\partial_x h_z \left(\cos\left(\frac{\pi}{3}\left[h_{z+1}+2\right]\right)\sin\left(\frac{\pi}{3}h_z\right)-\cos\left(\frac{\pi}{3}h_{z+1}\right)\sin\left(\frac{\pi}{3}\left[h_z+2\right]\right)\right)$$
$$= -\frac{\sqrt{3}\pi}{4}\partial_x h_z \cos\left(\delta_1 h_z\right) \tag{6.47}$$

$$\frac{\sqrt{3}\pi}{6}\partial_y h_z \left(\cos\left(\frac{\pi}{3}\left[h_{z+1}-2\right]\right)\left[\sin\left(\frac{\pi}{3}\left[h_z+2\right]\right)+\sin\left(\frac{\pi}{3}h_z\right)\right]\right.$$
$$\left.-\cos\left(\frac{\pi}{3}h_{z+1}\right)\sin\left(\frac{\pi}{3}h_z\right)-\cos\left(\frac{\pi}{3}\left[h_{z+1}+2\right]\right)\sin\left(\frac{\pi}{3}\left[h_z+2\right]\right)\right)$$
$$= \frac{\pi\sqrt{3}}{4}\partial_y h_z \sin\left(\delta_1 h_z\right) \tag{6.48}$$

So the total contribution for a hexagon is

$$= -\frac{\pi\sqrt{3}}{4}\left[\partial_x h_z \cos\left(\delta_1 h_z\right) - \partial_y h_z \sin\left(\delta_1 h_z\right)\right] \tag{6.49}$$

When we account for the multiplicative factors in the height mapping and sum over the contributions across the entire lattice, the Hamiltonian can be written as

$$\mathcal{H}_\perp = -\frac{4\pi J_\perp}{9\sqrt{3}}\sum_{\mathbf{r}}\left(\cos\left(\delta_1 h_z\right)\partial_x h_z - \sin\left(\delta_1 h_z\right)\partial_y h_z\right) + \ldots \tag{6.50}$$

where $\ldots$ indicates RG-irrelevant terms which would appear if we had included higher harmonic terms in the height mapping. Thus keeping only the relevant interlayer couplings and completing the square with the terms above leads to the effective Hamiltonian for the *abc* stacking

$$\mathcal{H}^{(abc)} = \frac{K}{2}\sum_z \int \mathrm{d}^2 r \left\{\left(\partial_x h_z - \kappa_\perp \cos\left(\delta_1 h_z\right)\right)^2 + \left(\partial_y h_z + \kappa_\perp \sin\left(\delta_1 h_z\right)\right)^2 - \left(\frac{\kappa_\perp}{K}\right)^2\right\} \tag{6.51}$$

with $\kappa_\perp \sim \beta J_\perp$.

The effective Hamiltonian for the *abab* stacking can be obtained similarly. One difference is that the vertical unit cell contains two layers, with the layers above and below offset in opposite directions. We use integer z to label unit cells in the vertical direction and $\mu = 1, 2$ to label layers within unit cells. The effective Hamiltonian is

$$\begin{aligned}\mathcal{H}^{(abab)} = \frac{K}{2}\sum_z \int \mathrm{d}^2 r \sum_\mu \big[& |\nabla h_{z,\mu}|^2 \\ & -\kappa_\perp \Big[\partial_x \left(h_{z,1} + h_{z,2}\right) \cos\frac{\pi}{3}\left(h_{z,2} - h_{z,1}\right) - \partial_y \left(h_{z,1} + \ h_{z,2}\right) \sin\frac{\pi}{3}\left(h_{z,2} - h_{z,1}\right) \\ & +\partial_x (h_{z+1,1} + h_{z,2}) \cos\frac{\pi}{3}(h_{z,2} - h_{z+1,1}) - \partial_y (h_{z+1,1} + h_{z,2}) \sin\frac{\pi}{3}(h_{z,2} - h_{z+1,1})\Big]\big] .\end{aligned} \tag{6.52}$$

For both frustrated stackings, emergent continuous symmetries not present in the lattice models are displayed by the effective Hamiltonian if terms irrelevant at the $J_\perp = 0$ fixed point are omitted.

Both models have a $U(1) \times U(1)$ symmetry. One $U(1)$ symmetry is associated with global shifts in the height field. It results from the discrete symmetry of the microscopic model related to global shifts in h. When the pinning potential is omitted, this symmetry is promoted to a continuous one. The pinning potential, $\tilde{V}(h)$, is irrelevant under RG, as in the single-layer height model. Also as in the unfrustrated case, we parameterise the symmetry with γ. The second $U(1)$ symmetry is associated with real-space rotations and is reduced to the discrete rotational symmetry of the lattice by irrelevant terms. We parameterise it with θ.

In detail, these symmetries take the following form. Let R_θ denote a rotation in the xy plane through the angle θ and write $\mathbf{r}' = R_\theta(\mathbf{r})$. Then $\mathcal{H}^{(abc)}$ is invariant under the transformation

$$h_z(\mathbf{r}) \to h'_z(\mathbf{r}) = h_z(\mathbf{r}') + \frac{3z\theta}{\pi} + \gamma. \tag{6.53}$$

Similarly $\mathcal{H}^{(abab)}$ is invariant under $h_{z,\mu}(\mathbf{r}) \to h'_{z,\mu}(\mathbf{r})$ with

$$h'_{z,1}(\mathbf{r}) = h_{z,1}(\mathbf{r}') - \frac{3\theta}{2\pi} + \gamma \tag{6.54}$$

$$h'_{z,2}(\mathbf{r}) = h_{z,2}(\mathbf{r}') + \frac{3\theta}{2\pi} + \gamma. \tag{6.55}$$

By inspection of the effective Hamiltonians, we can write down the ground state configurations. For the *abc* stacking, ground state configurations are

$$h_z(\mathbf{r}) = \kappa_\perp(x\cos\theta - y\sin\theta) + \frac{3z\theta}{\pi} + \gamma. \tag{6.56}$$

It can be checked that these are ground states by plugging them into the effective Hamiltonian. For the *abab* stacking the ground states are

$$h_{z,1}(\mathbf{r}) = \kappa_\perp(x\cos\theta - y\sin\theta) - \frac{3\theta}{2\pi} + \gamma, \tag{6.57}$$

$$h_{z,2}(\mathbf{r}) = \kappa_\perp(x\cos\theta - y\sin\theta) + \frac{3\theta}{2\pi} + \gamma. \tag{6.58}$$

In the *abab* case, we also have a second symmetry-related set of ground states.

However, as noted above, the continuous symmetry described by rotations θ is not present in the microscopic model. This symmetry is broken if one includes higher harmonic contributions in the height mapping from the spin interactions. The leading irrelevant terms are sufficient to break this symmetry. For the *abc* stacking, these are

$$\mathcal{H}_b^{(abc)} = \kappa_b \sum_z \int \mathrm{d}^2\mathbf{r} \left(\left[(\partial_x h_z(\mathbf{r}))^2 - (\partial_y h_z(\mathbf{r}))^2 \right] \cos\delta h_z(\mathbf{r}) + 2\partial_x h_z(\mathbf{r}) \partial_y h_z(\mathbf{r}) \sin\delta h_z(\mathbf{r}) \right), \tag{6.59}$$

where the form for the *abab* stacking follows analogously for higher harmonic contributions in the mapping. The symmetry may also be broken by certain further-neighbour couplings which are relevant. These terms may be generated under renormalisation or included microscopically.

For the *abc* stacking, some relevant and marginal couplings that are not included in the effective Hamiltonian above are

$$\mathcal{H}_{\nabla,m}^{(abc)} = \frac{K_m}{2} \sum_z \int \mathrm{d}^2\mathbf{r}\, \nabla h_z(\mathbf{r}) \cdot \nabla h_{z+m}(\mathbf{r}), \tag{6.60}$$

$$\mathcal{H}_2^{(abc)} = \kappa_2 \sum_z \int \mathrm{d}^2\mathbf{r} \left\{ \partial_x h_z(\mathbf{r}) \cos\frac{\pi}{3}(h_{z+2} - h_z) + \partial_y h_z(\mathbf{r}) \sin\frac{\pi}{3}(h_{z+2} - h_z) \right\}, \tag{6.61}$$

$$\mathcal{H}_3^{(abc)} = \kappa_3 \sum_z \int \mathrm{d}^2\mathbf{r}\, \cos\frac{\pi}{3}(h_{z+3} - h_z). \tag{6.62}$$

$\mathcal{H}_3^{(abc)}$ is the most relevant of these three: it breaks the rotational degeneracy of θ, selecting ground states for which $3\theta = 0$ (π) for $\kappa_3 < 0$ $(\kappa_3 > 0)$. $\mathcal{H}_3^{(abc)}$ is an unfrustrated coupling between sites displaced by 3 layers in the z direction. $\mathcal{H}_2^{(abc)}$ has the same scaling dimension as the bare interlayer coupling. It also breaks the symmetry, again favouring states for which $3\theta = 0$ (π) for $\kappa_2 < 0$ $(\kappa_2 > 0)$. $\mathcal{H}_2^{(abc)}$ is a coupling between nearest neighbours that are separated by 2 layers in the z direction. $\mathcal{H}_{\nabla,m}^{(abc)}$ is marginal, and does not break the degeneracy between the ground states identified above, all of which have the same in-plane gradients in each layer. This term is a coupling between the gradients of planes separated by m layers.

Therefore as well as potentially being broken spontaneously at low temperature, the emergent $U(1)$ spiral symmetry of the *abc* model can be broken explicitly at a scale set by the coefficients κ_2 and κ_3. This latter form of symmetry breaking will be discussed later.

For the *abab* stacking, the most important couplings beyond the bare model are interlayer gradient couplings similar to $\mathcal{H}_{\nabla,m}^{(abc)}$ and

$$\mathcal{H}_3^{(abab)} = \kappa_3 \sum_{z,\mu} \int \mathrm{d}^2\mathbf{r} \, \cos\frac{\pi}{3}(h_{z+1,\mu} - h_{z,\mu}). \tag{6.63}$$

$\mathcal{H}_3^{(abab)}$ is the unfrustrated coupling between spins two layers apart.

However, in contrast to the *abc* case, $\mathcal{H}_3^{(abab)}$ is not important in determining the ordering temperature. $h_{z+1,\mu} - h_{z,\mu}$ does not depend on the parameters θ, γ for ground state configurations in the *abab* stacking and so these terms will not break the degeneracy. Instead, the symmetry is broken by irrelevant couplings that arise from the higher harmonic contributions to the height mapping, $\mathcal{H}_b^{(abab)}$.

6.3 Spin Correlations from Heights

The structure factor, which shows helices and rings for the frustrated stackings, is the most striking signature of the classical spin-liquid regime. Here we show how these arise from considering expressions for the correlation functions in terms of the height fields. Because there is no long-range order within the classical spin-liquid, the

system is divided into independent correlation volumes. As an approximation, we can average over the ground states to estimate the correlation function in this regime.

We first rely on the assumption that the first harmonic in the spin-height mapping is sufficient, so $\sigma_{j,z} \sim \cos\left(\frac{\pi}{3}\left[h_z\left(\mathbf{r}_j\right) + s_\alpha\right]\right)$. Then, using the notation from subsection 4.1.1, we can write the Fourier transform of the spins near the Brillouin zone corner $\mathbf{K}$,

$$\mathbf{k} = \mathbf{K} + n_1\mathbf{A}_1 + n_2\mathbf{A}_2 + \mathbf{q}, \tag{6.64}$$

$$p = n_1 + n_2, \tag{6.65}$$

$$\sum_{j,z} \sigma_{j,z} e^{i(\mathbf{K}+\mathbf{q})\cdot\mathbf{r}_{j,z}} = \sum_{j,z} e^{-i\left[\frac{\pi}{3}h_z(\mathbf{r}_j) - \left(\mathbf{q}_\perp\cdot\mathbf{r}_j + \left(q_z + \frac{2\pi}{3}p\right)\right)\right]}, \tag{6.66}$$

where the ground states are of the form $h_z\left(\mathbf{r}\right) = \kappa_\perp\left(x\cos\theta + y\sin\theta\right) + \frac{3\theta z}{\pi}$. Carrying out the integral and averaging over the ground states (via an integral over θ, denoted $\langle \ldots \rangle$ here), we obtain for the structure factor

$$S\left(\mathbf{K}+\mathbf{q}\right) = \sum_{j,z} \langle \sigma_{0,0}\sigma_{j,z}\rangle e^{i(\mathbf{K}+\mathbf{q})\cdot\mathbf{r}_{j,z}}, \tag{6.67}$$

$$= (2\pi)^3 \left\langle \delta\left(q_z - \theta + \frac{2p\pi}{3}\right)\delta\left(q_x - \frac{\pi}{3}\kappa_\perp\cos\theta\right)\delta\left(q_y + \frac{\pi}{3}\kappa_\perp\sin\theta\right)\right\rangle, \tag{6.68}$$

$$= (2\pi)^2\,\delta\left(q_x - \frac{\pi}{3}\kappa_\perp\cos\left(q_z + \frac{2\pi}{3}p\right)\right)\delta\left(q_y + \frac{\pi}{3}\kappa_\perp\sin\left(q_z + \frac{2\pi}{3}p\right)\right). \tag{6.69}$$

If we had expanded around the Brillouin zone corner $\mathbf{K}'$ instead, the helix would be given with the opposite handedness. Similarly, p dictates the phase shift of the helices. The analogous expression for the *abab* stacking is

$$S\left(\mathbf{K}+\mathbf{q}\right) = \delta\left(q_z\right)\delta^{(2)}\left(q_\perp^2 - \left(\frac{\pi}{3}\right)^2\kappa_\perp^2\right). \tag{6.70}$$

We expect that finite correlation lengths give rise to a broadening of these functions, which we observe in the numerical simulations.

In this section, we have demonstrated that the height field approach for these systems gives access to features of the classical spin-liquid regime, such as helices and rings in the structure factor, in a very straight-forward manner. More broadly, in this

chapter, we have introduced the height model approach for STLIAFMs. We have seen how the height model arises for a single layer, how it captures the basic features of single layers, and details of how it may be generalised to the stacked systems we study here. We have also briefly presented the ground states, some additional couplings in the effective Hamiltonian, and an expression for the structure factor derived via this mapping. The height field provides an analytical tool with which we can investigate the classical spin-liquid regime in a more controlled manner, in particular using the perturbative renormalisation group.

Chapter 7

Renormalisation Group Analysis

With the height field theory for the STLIAFM in hand, we can utilise a standard tool in statistical physics, the perturbative renormalisation group (RG). The RG makes a tremendous conceptual and quantitative leap beyond mean-field theory. In this section, we first present the basic momentum-shell RG in application to the height field for the TLIAFM. This model coincides with the well-known sine-Gordon model in two dimensions.

Subsequently, we apply the renormalisation group to the coupled height field theory of the STLIAFM. We will derive the first-order flow equations and then consider the behaviour of the system using these as a starting point. We then consider fluctuations in the ground state manifold and vortices in these systems. The combination of vortices and terms generated in the RG is essential to the classical spin-liquid regime.

7.1 Renormalisation Group for TLIAFM

The momentum shell renormalisation group procedure can be demonstrated by considering, first, the sine-Gordon model in two dimensions [50]. We note again that we have motivated the following action from the height model.

$$S = S_0 + S_1, \tag{7.1}$$

$$S_0[h] = \frac{1}{2}\int d^2\mathbf{r}|\nabla h|^2, \tag{7.2}$$

$$S_1[h] = \kappa \int d^2\mathbf{r}\cos(\beta h). \tag{7.3}$$

We have assumed that h is a scalar field defined over two dimensions. The partition function is

$$\mathcal{Z} = \int \mathcal{D}\left[h\right] e^{-S[h]}. \tag{7.4}$$

As with the systems considered in this thesis, we imagine that this field theory is obtained via coarse-graining a lattice theory. From the lattice theory, we have a short distance cut-off, ℓ. Equivalently, we can define the large quasimomentum cut-off $\Lambda = \frac{1}{\ell}$. Using this cut-off, we can write the Fourier decomposition of h as

$$h\left(\mathbf{r}\right) = \frac{1}{\sqrt{V}} \sum_{k<\Lambda/s} e^{i\mathbf{k}\cdot\mathbf{r}} h_k + \frac{1}{\sqrt{V}} \sum_{\Lambda/s<k<\Lambda} e^{i\mathbf{k}\cdot\mathbf{r}} h_k, \tag{7.5}$$

$$\equiv h^{<}_{\Lambda/s}\left(\mathbf{r}\right) + h^{>}\left(\mathbf{r}\right). \tag{7.6}$$

$h^{<}_{\Lambda/s}$ is the long wavelength, slow degrees of freedom and $h^{>}$ is the short wavelength, fast degrees of freedom. We can insert this decomposition in the action and observe the following simplification

$$S_0 = \frac{1}{2} \int d^2\mathbf{r} \left(\nabla h^{<}_{\Lambda/s} + \nabla h^{>}\right)^2 \tag{7.7}$$

$$= \frac{1}{2} \int d^2\mathbf{r} \left[\left(\nabla h^{<}_{\Lambda/s}\right)^2 + \left(\nabla h^{>}\right)^2\right] \tag{7.8}$$

$$= S_0\left[h^{<}_{\Lambda/s}\right] + S_0\left[h^{>}\right]. \tag{7.9}$$

The partition function for a given cut-off, Λ, can be written

$$\mathcal{Z}_\Lambda = \int \mathcal{D}h^{<}_{\Lambda/s} \mathcal{D}h^{>} e^{-\left(S_0\left[h^{<}_{\Lambda/s}\right] + S_0[h^{>}] + S_1\left[h^{<}_{\Lambda/s} + h^{>}\right]\right)}. \tag{7.10}$$

We can re-express this combination of functional integrals in a convenient way. First, we re-write the integral over h as an expectation in the free theory for h. Then we obtain an effective action for $h^{<}_{\Lambda/s}$

$$\mathcal{Z}_\Lambda = \mathcal{Z}_0 \int \mathcal{D}h^{<}_{\Lambda/s} e^{-S_0\left[h^{<}_{\Lambda/s}\right]} \langle \exp\left(-S_1\left[h^{<}_{\Lambda/s} + h^{>}\right]\right)\rangle_0, \tag{7.11}$$

$$S_{\text{eff}}\left[h^{<}_{\Lambda/s}\right] = S_0\left[h^{<}_{\Lambda/s}\right] - \ln\left(\langle \exp\left(-S_1\left[h^{<}_{\Lambda/s} + h^{>}\right]\right)\rangle_0\right). \tag{7.12}$$

Now we expand the logarithm and terms therein, truncating at second order to obtain

$$S_{\text{eff}}\left[h^{<}_{\Lambda/s}\right] = S_0\left[h^{<}_{\Lambda/s}\right] + \langle S_1\rangle_0 - \frac{1}{2}\left[\langle S_1^2\rangle_0 - \langle S_1\rangle_0^2\right] + \ldots. \tag{7.13}$$

To obtain an explicit expression for this action, we need to evaluate $\langle S_1 \rangle_0$. We can do this by first writing the cosine in terms of exponentials and then expanding these exponentials to second order. Eventually we just need to evaluate $\langle h^2 \rangle_0$. This is straightforward for the free theory in h and we have

$$\langle h^2 \rangle_0 = \int_{\Lambda/s}^{\Lambda} \frac{d^2\mathbf{k}}{(2\pi)^2} \frac{1}{k^2} \approx \frac{1}{2\pi}(s-1) \equiv \frac{d\ell}{2\pi}, \tag{7.14}$$

$$\langle S_1 \rangle_0 = g \left[1 - \frac{\beta^2}{4\pi} d\ell \right] \int d^2\mathbf{r} \cos\left(\beta h^{<}_{\Lambda/s} \right). \tag{7.15}$$

Finally, we can write the effective action and scale $\mathbf{k} \to \frac{\mathbf{k}'}{s}, \mathbf{r} \to s\mathbf{r}'$ to obtain the renormalised coupling (after renaming $\mathbf{k}' \to \mathbf{k}, \mathbf{r}' \to \mathbf{r}$)

$$S_{\text{eff}}[h] = \frac{1}{2} \int d^2\mathbf{r} |\nabla h|^2 + \kappa \left[1 + \left(2 - \frac{\beta^2}{4\pi} \right) d\ell \right] \int d^2\mathbf{r} \cos(\beta h). \tag{7.16}$$

Identifying $\kappa' = \kappa \left[1 + \left(2 - \frac{\beta^2}{4\pi} \right) d\ell \right]$, we have the scaling equation for the cosine coupling

$$\frac{d\kappa}{d\ell} = \left(2 - \frac{\beta^2}{4\pi} \right) \kappa. \tag{7.17}$$

We can also use this analysis to recover the scaling dimensions presented in the earlier treatment of the TLIAFM. We apply this same procedure to the coupled height field theory below.

7.2 Weakly Coupled Layers

We now consider the perturbative RG for the STLIAFM via the coupled height field. Here we derive the flow equations for parameters $\kappa_\perp, \kappa_3, y$. $\kappa_\perp$ is the interlayer coupling, κ_3 is the coupling between sites in identically labelled layers. For example, coupling between nearest neighbours which are both in b-layers in the *abc* stacking (directly above or below each other, but separated by three layers). For the *aaa* stacking, this coupling is the same as $\kappa_\perp$. y is the vortex fugacity. The vortex fugacity determines the density of vortices. The perturbative regime is for low temperatures and small interlayer coupling.

Using the same momentum-shell RG as above, we can derive the flow equations for these couplings. We demonstrate this for the interlayer coupling in the case of the *abc* stacking

$$\mathcal{H}_\perp = \kappa_\perp \int d^2\mathbf{r} \left[\partial_x h_z(\mathbf{r}) \cos\left(\delta h_z\right) - \partial_y h_z(\mathbf{r}) \sin\left(\delta h_z\right)\right]. \tag{7.18}$$

To make the evaluation of $\langle \mathcal{H}_\perp \rangle_0$ more straightforward, we write $\mathbf{r}$ as $\zeta = x + iy$, where x, y are the planar coordinates for layer z

$$\mathcal{H}_\perp = \kappa_\perp \mathrm{Im}\left[\int d^2\mathbf{r} \partial_{\bar{\zeta}} e^{i\delta h_z}\right], \tag{7.19}$$

$$\langle \mathcal{H}_\perp \rangle_0 = \kappa_\perp \mathrm{Im}\left[\int d^2\mathbf{r} \partial_{\bar{\zeta}} e^{i\delta h_z^<} \langle e^{i\delta h_z^>} \rangle_0\right]. \tag{7.20}$$

After rescaling, we have the flow equation for $\kappa_\perp$

$$\frac{d\kappa_\perp}{d\ln \ell} = \left(1 - \beta_1\right) \kappa_\perp. \tag{7.21}$$

The flow equations to first-order for κ_3, y are

$$\frac{d\kappa_3}{d\ln \ell} = \left(2 - \beta_1\right) \kappa_3, \tag{7.22}$$

$$\frac{dy}{d\ln \ell} = \left(2 - \alpha_1\right) y, \tag{7.23}$$

where $\beta_1 = \frac{\pi}{18K}, \alpha_1 = \frac{9K}{\pi}$. The bare values of these coupling constants can be read off from our effective Hamiltonians

$$\kappa_{3,0} \sim \beta J_\perp, \tag{7.24}$$

$$\kappa_{\perp,0} \sim \beta J_\perp, \tag{7.25}$$

$$y_0 \sim e^{-4\beta J}. \tag{7.26}$$

As we are perturbing from the single-layer problem, we take $K = \frac{\pi}{9}$. Solving the flow equations, we have

$$y = y_0 \ell, \tag{7.27}$$

$$\kappa_\perp = \kappa_{\perp,0} \ell^{1/2}, \tag{7.28}$$

$$\kappa_3 = \kappa_{3,0} \ell^{3/2}. \tag{7.29}$$

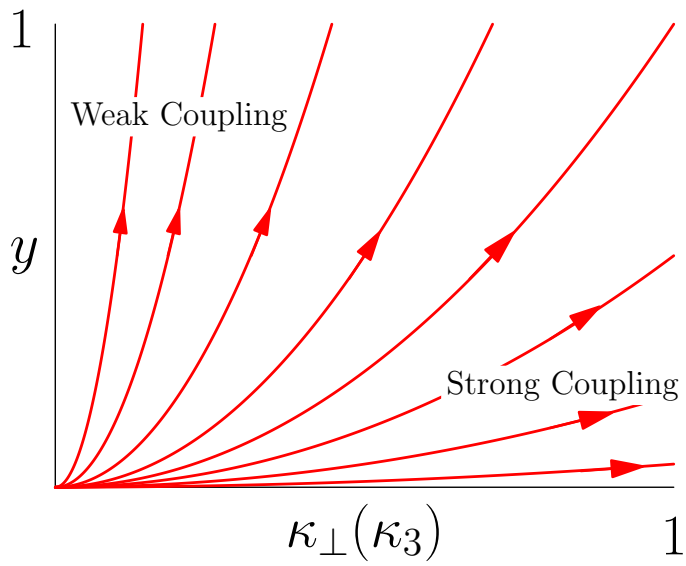

Figure 7.1: Schematic flow of coupling constants to leading order.

Following the flow, the system can arrive in one of two regimes when the largest coupling is of order unity. These regimes are proliferating vortices or strongly coupled layers, see the schematic Fig. 7.1, depending on whether $y \sim 1$ first or $\kappa_\perp(\kappa_3) \sim 1$ first.

We now outline the following approach to the strongly coupled layers. If the coupling constants flow such that the system is composed of strongly coupled layers, one possibility is that the system is long-range ordered. However, we will show that the system resists order and instead displays the classical spin-liquid regime we have described.

Within the strongly coupled regime, there are two possibilities that may disrupt long-range ordering. First, we may have fluctuations in the ground-state manifold that prevent ordering. We will show, however, that these fluctuations are not enough to prevent long-range ordering. Second, the contributions from vortices may prevent ordering. These contributions will be sufficient to allow for the classical spin-liquid regime, in which there are strong correlations throughout the system, but no long-range order. The contributions from vortices are eventually balanced by the locking terms and predict a transition in the coupled height field theory.

7.3 Harmonic Fluctuations

Here we consider the first possibility for avoiding long-range order in the strongly coupled layer regime. We compute the energy cost of harmonic excitations out of the ground states and use the dispersion to evaluate fluctuations. If the fluctuations are divergent, long-range order will be destroyed. We will find that the harmonic excitations for *abc* and *abab* stackings are soft, but do not lead to divergences in the fluctuations for finite interlayer coupling.

We start by writing a field configuration that includes small excitations out of the ground state. We pick a ground state parametrised by $\theta = 0$.

$$h_z(r) = h^{GS}(r) + \phi_z = \kappa_\perp x + \gamma + \phi_z. \tag{7.30}$$

Now we can write an expression for the effective Hamiltonian in terms of these degrees of freedom, truncating at quadratic order in the excitations:

$$\begin{aligned}
\mathcal{H}^{(abc)} &= \frac{K}{2}\sum_z \int \mathrm{d}^2 r \left\{ \left(\partial_x h_z - \kappa_\perp \cos\left(\delta_1 h_z\right)\right)^2 + \left(\partial_y h_z + \kappa_\perp \sin\left(\delta_1 h_z\right)\right)^2 - \left(\frac{\kappa_\perp}{K}\right)^2 \right\}, \\
&\approx \frac{K}{2}\sum_z \int \mathrm{d}^2 r \left\{ \left(\partial_x \phi_z\right)^2 + \left(\partial_y \phi_z\right)^2 + 2\partial_y \phi_z \kappa_\perp (\delta_1 h_z) + \left(\kappa_\perp (\delta_1 h_z)\right)^2 - \left(\frac{\kappa_\perp}{K}\right)^2 \right\}, \\
&= \frac{K}{2}\sum_z \int \mathrm{d}^2 r \left\{ \phi_z(-\partial_x^2 \phi_z - \partial_y^2 \phi_z - 2\kappa_\perp \partial_y(\phi_{z+1} - \phi_z) + \right. \\
&\qquad \left. 2\kappa_\perp^2(\phi_z - \phi_{z+1})) - \left(\frac{\kappa_\perp}{K}\right)^2 \right\}.
\end{aligned} \tag{7.31}$$

Below, we have expanded the excitation out of the ground state via Fourier transform, rearranged the summation over layers, and consider just the energy change due to the excitations:

$$\phi_z(r) = \frac{1}{(2\pi)^3}\int d^3 q \phi(q) e^{i(\mathbf{q}_\perp \cdot \mathbf{r} + q_z z)}, \tag{7.32}$$

$$\delta\mathcal{H}^{(abc)} = \frac{1}{(2\pi)^3}\frac{K}{2}\int d^3 q |\phi(q)|^2 \epsilon\left(q\right), \tag{7.33}$$

$$\epsilon\left(q\right) = q_x^2 + q_y^2 + 2\left(\kappa_\perp \frac{\pi}{3}\right)^2 - 2\left(\kappa_\perp \frac{\pi}{3}\right)^2 \cos\left(q_z\right) - 2\left(\kappa_\perp \frac{\pi}{3}\right) q_y \sin\left(q_z\right), \tag{7.34}$$

$$= q_x^2 + \left(q_y - \left(\kappa_\perp \frac{\pi}{3}\right)\sin\left(q_z\right)\right)^2 + \left(\kappa_\perp \frac{\pi}{3}\right)^2 \left(1 - \cos\left(q_z\right)\right)^2. \tag{7.35}$$

Considering the line $q_x = 0, q_y = \kappa_\perp \frac{\pi}{3} q_z$, we have a soft dispersion relation. Specifically, we have a dispersion relation that is quartic in q_z. In contrast with some situations, the soft modes here do not lead to divergent fluctuations. We can explicitly use the expression to compute expectations in the manifold of harmonic excitations out of the ground states. In particular, we can see whether the next highest order contributions that we have ignored in the effective Hamiltonian are divergent

$$\langle [h_{z+1} - h_z]^2 \rangle = \langle \phi_{z+1}^2 \rangle + \langle \phi_z^2 \rangle - 2\langle \phi_{z+1}\phi_z \rangle, \tag{7.36}$$

$$\langle \phi_z^2 \rangle = \langle \phi_{z+1}^2 \rangle = \frac{1}{(2\pi)^3}\frac{1}{K}\int d^3q \frac{1}{\epsilon\,(q)}, \tag{7.37}$$

$$2\langle \phi_z \phi_{z+1} \rangle = \frac{1}{(2\pi)^3}\frac{1}{K}\int d^3q \frac{e^{iq_z} + e^{-iq_z}}{\epsilon\,(q)}, \tag{7.38}$$

$$\langle [h_{z+1} - h_z]^2 \rangle = \frac{1}{(2\pi)^3}\frac{1}{K}\int d^3q \frac{2(1-\cos\,(q_z))}{\epsilon\,(q)}. \tag{7.39}$$

Expanding along the line of soft modes, we see that these fluctuations are finite for $\kappa_\perp \neq 0$. As we explicitly consider the regime with non-zero interlayer coupling, this result yields the following conclusion. Harmonic fluctuations, despite giving rise to soft modes, do not lead to divergences that destroy long-range order in the coupled-layer regime.

So far, we have only considered the *abc* stacking. We briefly summarise the results for the other stackings here. The procedure for deriving the dispersion relations is very similar, except for changes to accommodate the two-site unit cell in the *abab* stacking.

For the other stacking which is frustrated, *abab*, we have soft modes which are similar to the *abc* case. We introduce two fields to describe the fluctuations for each of the sites in the unit cell. The resulting dispersion is characterised by two relations

$$\epsilon_\pm(q) = q_x^2 + q_y^2 + 2\left(\kappa_\perp \frac{\pi}{3}\right)^2 \pm 2\left(\kappa_\perp \frac{\pi}{3}\right)\left|\cos\left(\frac{q_z}{2}\right)\right| \sqrt{q_y^2 + \left(\kappa_\perp \frac{\pi}{3}\right)^2}. \tag{7.40}$$

The $\epsilon_-(q)$ dispersion relation is $q_x^2 + \left(\tilde{\kappa}_\perp^2 q_z^2 + q_y^4/\tilde{\kappa}_\perp^2\right)/4$ for small $|\mathbf{q}|$ in reciprocal space, and again yields finite fluctuations for finite $\kappa_\perp$.

The *aaa* stacking leads to a dispersion which is unsurprising. The excitations in

that case are governed by

$$\epsilon(q) = q_x^2 + q_y^2 + \kappa_\perp \frac{\pi}{3}\left(1 - \cos\left(q_z\right)\right), \tag{7.41}$$

which does not admit a line with quartic dispersion, and so there are no soft modes.

The analysis of harmonic excitations out of ground states in the strongly coupled regime does not lead to divergences that disrupt ordering. However, we note that the dispersion in the frustrated stackings, *abc* and *abab*, is unconventional. The dispersion relations for the frustrated stackings have a line of soft modes which will play an important role in the subsequent analysis of vortex excitations out of the ground-state manifold.

7.4 Bound Vortices

Instead of considering small excitations out of the ground states, we now consider vortices in the height field that occur at finite temperature. We have already shown that vortices proliferate in the case of uncoupled layers and lead to a paramagnet at non-zero temperature. Here we will see that vortices are bound, but still lead to divergent fluctuations.

We start by considering a vortex-antivortex pair within a layer ($z = 0$) and will show that these are bound and have a linear confining potential. To start, we consider the vortex contribution to the energy in the height field out of the ground-state $\theta = 0$ for the *abc* stacking

$$h_z(r) = \kappa_\perp x + \chi_z(r), \tag{7.42}$$

$$\chi_z(r) = 0 \text{ if } z \neq 0. \tag{7.43}$$

Assuming that the vortices occupy a single layer, we expect two terms

$$\begin{aligned}\delta\mathcal{H}_{v-av} = &\left(\partial_x\chi_0(r) + \kappa_\perp\left(1 - \cos\left(\frac{\pi}{3}\chi_0(r)\right)\right)\right)^2 + \left(\partial_y\chi_0(r) + \kappa_\perp \sin\left(\frac{\pi}{3}\chi_0(r)\right)\right)^2 \\ &+ \left(-\kappa_\perp \cos\left(\frac{\pi}{3}\chi_0(r)\right)\right)^2 + \left(-\kappa_\perp \sin\left(\frac{\pi}{3}\chi_0(r)\right)\right)^2.\end{aligned} \tag{7.44}$$

We make the following assumptions about the vortex-antivortex pair: they are well-separated and give a change in the height field of 6 across a width of w. We can

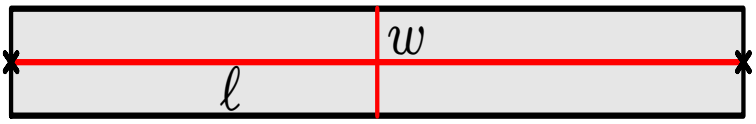

Figure 7.2: Schematic of region integrated over to compute contribution to effective Hamiltonian from vortex-antivortex pair.

integrate the expression above across the width of the strip, as shown in Fig. 7.4, to obtain the energy contribution of such a configuration using these assumptions

$$\delta\mathcal{H}_{v-av} = \frac{K}{2}\int \mathrm{d}^2 r \left[|\nabla\chi_0|^2 + 4\kappa_\perp^2\right]. \tag{7.45}$$

Considering only contributions that depend on w, we have energy cost per length

$$\frac{\delta\mathcal{H}_{v-av}}{\ell} \sim Kw\left[\frac{1}{2w^2} + 2\kappa_\perp^2\right]. \tag{7.46}$$

We can find the optimal width $w = \frac{1}{2}\kappa_\perp^{-1}$, which gives a confining potential $\mathcal{E}_{v-av} \sim 2K\kappa_\perp$. Vortex pairs which are widely separated will have a separation large with respect to the width. Since the width is inversely proportional to $\kappa_\perp$, the pairs are tightly bound by the linear confining potential in the strongly coupled layer regime. These bound vortices will prove to be an essential ingredient for the classical spin-liquid regime in the frustrated stackings. This is surprising as one would generally expect that bound vortex pairs are unimportant at sufficiently large length scales.

To see the effect these bound vortex pairs have on the systems when in the strongly coupled layer regime, we need a more convenient way to incorporate vortices into the height field theory. Instead of treating the bona fide multivalued height fields, we make an alternative treatment that includes the essential physics.

We start by writing the vortex contribution to the height field for a vortex-antivortex pair in a single layer. This must be a configuration which is a solution to $\nabla^2 h(\mathbf{r}) = 0$, where we write $\chi(\mathbf{r})$ again for the vortex portion of $h(\mathbf{r})$,

$$\chi_{v-av}(\mathbf{r}) = \frac{3}{\pi}\left[\arctan\left(\frac{2x+b_x}{2y+b_y}\right) - \arctan\left(\frac{2x-b_x}{2y-b_y}\right)\right], \tag{7.47}$$

where the pair is separated by $\mathbf{b}$ and centred on the origin. To circumvent the multivalued nature of the height field, we can consider such a configuration at points

in space which are far from the origin. By going to the limit of $|\mathbf{r}| \gg |\mathbf{b}|$, we can write the configuration for a vortex-antivortex pair as

$$\chi_{v-av}(\mathbf{r}) \approx \frac{3}{\pi}\frac{|\mathbf{b}\times\mathbf{r}|}{r^2}. \tag{7.48}$$

We can include the cost of vortex-antivortex pairs on top of a ground state in the strongly coupled limit by writing a potential term. The potential should couple to the height field in a way that induces the above configuration. To accomplish this, we write an expression for the effective Hamiltonian of a single layer in terms of Fourier modes

$$\mathcal{H} = \frac{K}{2}\frac{1}{(2\pi)^2}\int d^2\mathbf{q}\left[\epsilon(\mathbf{q})|\phi(\mathbf{q})|^2 - \phi(-\mathbf{q})v(\mathbf{q})\right]. \tag{7.49}$$

To see that the second term can be used to induce the vortex-antivortex pair configuration, we can minimise the effective Hamiltonian in the usual way. The optimal configuration of the height field out of the ground-state is

$$\phi(\mathbf{q}) = \frac{v(\mathbf{q})}{\epsilon(\mathbf{q})}. \tag{7.50}$$

In order to determine the potential needed, we write the vortex-antivortex pair configuration in Fourier space

$$\chi_{v-av}(\mathbf{q}) \approx 6i\frac{|\mathbf{q}\times\mathbf{b}|}{q^2}. \tag{7.51}$$

Using the dispersion of a single layer, $\epsilon(\mathbf{q}) = q^2$, we can write the potential necessary to induce a vortex-antivortex pair

$$v_{v-av}(\mathbf{q}) = 6i|\mathbf{q}\times\mathbf{b}|. \tag{7.52}$$

We now generalise to the multilayer, stacked systems. By using the same linear coupling to a potential of the Fourier modes in the effective Hamiltonian, we can induce configurations that have vortex-antivortex pairs. Suppose we have n vortex-antivortex pairs with centres $\mathbf{r}_j, z_j$ and pair separation $\mathbf{b}_j$. The potential above is modified first by accounting for multiple pairs and second by using the dispersion

$\epsilon(\mathbf{q})$ for the stacked systems instead of a single layer

$$v_{\rm tot}(\mathbf{q}) = 6i \sum_j |\mathbf{q} \times \mathbf{b}_j| e^{-i(\mathbf{q}_\perp \mathbf{r}_j + q_z z_j)}. \tag{7.53}$$

As above, we can compute the fluctuations from the configurations arising from many vortex-antivortex pairs

$$\int d^3\mathbf{r} \langle [\phi_{\rm tot}(\mathbf{r})]^2 \rangle = \int \frac{d^3\mathbf{r}}{(2\pi)^6} \langle \left[\int d^3\mathbf{q} \frac{v_{\rm tot}(\mathbf{q})}{\epsilon(\mathbf{q})} e^{i(q_\perp r + q_z z)} \right]^2 \rangle \tag{7.54}$$

$$= \int \frac{d^3\mathbf{q} d^3\mathbf{q}'}{(2\pi)^6} \int d^3\mathbf{r} \langle e^{i((q'_\perp + q_\perp)r + (q'_z + q_z)z)} \frac{v_{\rm tot}(\mathbf{q}') v_{\rm tot}(\mathbf{q})}{\epsilon(\mathbf{q})\epsilon(\mathbf{q}')} \rangle \tag{7.55}$$

$$= \frac{\rho}{(2\pi)^3} \int d^3\mathbf{q} \frac{\langle |v_{v-av}(\mathbf{q})|^2 \rangle}{\epsilon^2(\mathbf{q})}, \tag{7.56}$$

where ρ is the density of vortices, which we assume are Poisson distributed. In the above expression, the average $\langle \dots \rangle$ denotes an average over vortex-antivortex pair separation, $\mathbf{b}_j$, rather than a thermal average. For small $\mathbf{q}$, this integral is divergent for the soft dispersion of the frustrated stackings (though it is convergent for the *aaa* stacking). We thus draw the conclusion that these vortex-antivortex pairs lead to fluctuations that prevent long-range order in the *abc* and *abab* stackings.

We also note that the unfrustrated stacking, *aaa*, does not admit any divergences, so we lack a mechanism to prevent long-range order in the strongly coupled layer regime and cannot have a classical spin-liquid regime.

The divergence of the fluctuations can be used to estimate the correlation length. To extract the correlation length in the regime with strongly coupled layers and no long-range order, we require that the average separation is given by the length scale ℓ, where ℓ corresponds to $\kappa_\perp \sim 1$. By imposing a small wave vector cutoff in the fluctuation integrals when they reach order 1, we obtain the following correlation lengths for the *abc* stacking

$$\xi_\perp \sim \kappa_\perp^{-1} \left(\rho \ell^2\right)^{-2}, \tag{7.57}$$

$$\xi_z \sim \left(\rho \ell^2\right)^{-1}. \tag{7.58}$$

The analogous expressions for the *abab* stacking are

$$\xi_\perp \sim \kappa_\perp^{-1} \left(\rho\ell^2\right)^{-\frac{1}{2}}, \tag{7.59}$$

$$\xi_z \sim \left(\rho\ell^2\right)^{-\frac{1}{2}}. \tag{7.60}$$

The story presented thus far allows for a regime of strongly coupled layers that avoid long-range order. This is the classical spin-liquid regime of the paramagnetic phase. However, we know that the system must eventually undergo a transition to a long-range ordered phase.

7.5 Transition to Order

The transition from the classical spin-liquid regime to the long-range ordered state relies on interactions that we have not considered in the analysis thus far. These interactions are locking terms which balance the fluctuations from the vortex-antivortex pairs and lead to an ordering transition.

For the *abc* stacking, there are two types of locking terms to consider. The first is a term which is absent microscopically, but which is generated at higher orders in the renormalisation group. This interaction has been denoted κ_3 and refers to coupling between sites which are three layers apart. The second type of coupling is a term which is present microscopically, but which we have ignored to this point. These couplings are denoted κ_b and are interactions which are generated at higher orders in the expansion of the height field.

Although κ_3 is relevant and κ_b is irrelevant, in the case here (without κ_3 in the initial Hamiltonian), κ_b will stabilise order instead of κ_3. The initial values for each of these couplings are

$$\kappa_3 \sim \left(\beta J_\perp\right)^7, \tag{7.61}$$

$$\kappa_b \sim \left(\beta J_\perp\right). \tag{7.62}$$

These statements and initial values follow from the second-order RG equations [1], which we do not discuss here. We take these insights and focus on the coupling

κ_b. The flow equation for κ_b is

$$\frac{d\kappa_b}{d\ln\ell} = -\beta_1\kappa_b. \tag{7.63}$$

We can use the locking term to estimate the ordering transition boundary in the strongly coupled layers regime. We find the boundary by requiring that the locking potential, when integrated over the correlation volume, is order 1 to balance the fluctuations from the bound vortex-antivortex pairs.

$$\kappa_b\xi_\perp^2\xi_z \sim 1. \tag{7.64}$$

For the *abab* stacking, there is not a relevant locking term, κ_3. So, the equivalent κ_b coupling is the term which dictates the ordering transition. In the next chapter, we use the expressions derived here to find explicit predictions for the phase boundaries and compare these with the numerical results.

In this chapter, we have shown that considerations of harmonic fluctuations, bound vortex-antivortex pairs, and locking terms lead to the classical spin-liquid in the STLIAFMs. The combination of soft modes and bound vortex-antivortex pairs give a regime in which layers are strongly coupled, but resist long-range order. This regime emerges within the conventional paramagnet as temperature decreases and the frustration and vortex-antivortex pair fluctuations become important. At even lower temperatures, the locking terms balance these fluctuations and the system undergoes a transition to a 3D ordered states. Chapter 8, we characterise the phase diagram from this treatment and make a comparison with numerics.

Chapter 8

Phase Diagram and Summary

In this section, we present a phase diagram for the STLIAFM generated from the height field theory predictions. We compare the boundaries on this diagram to the phase boundaries determined by the numerical simulations and show good agreement. Following these comparisons, we give a brief outlook of some possible future directions and summarise the work in this Part of the thesis.

8.1 Phase Boundaries and Comparisons

Here we derive the phase boundaries in the STLIAFM using the predictions from the height field approach. We start by recalling the conclusion from the first-order renormalisation group analysis: if the parameters $\kappa_\perp$ or κ_3 flow to $\mathcal{O}(1)$ before the parameter y flows to $\mathcal{O}(1)$, then the systems are in the strongly coupled regime.

In this regime, we have seen how the frustrated stacking can remain disordered due to soft modes in the dispersion and bound vortex-antivortex pairs. However, we also noted the balancing of these contributions with the contributions from locking terms that can be generated under RG or present microscopically. These terms break the continuous symmetry and provide an ordering effect over a volume dictated by the correlation lengths. Balancing these effects allows us to determine the phase boundary to long-range order as follows, for the *abc* stacking,

$$\kappa_b \xi_\perp^2 \xi_z \sim 1, \tag{8.1}$$

$$\left(\kappa_{b,0} \ell^{-1/2}\right) \sim \kappa_\perp^2 \left(\ell^2 \rho\right)^5, \tag{8.2}$$

$$\left(\beta J_\perp\right) \ell^{-1/2} \sim y^{10}, \tag{8.3}$$

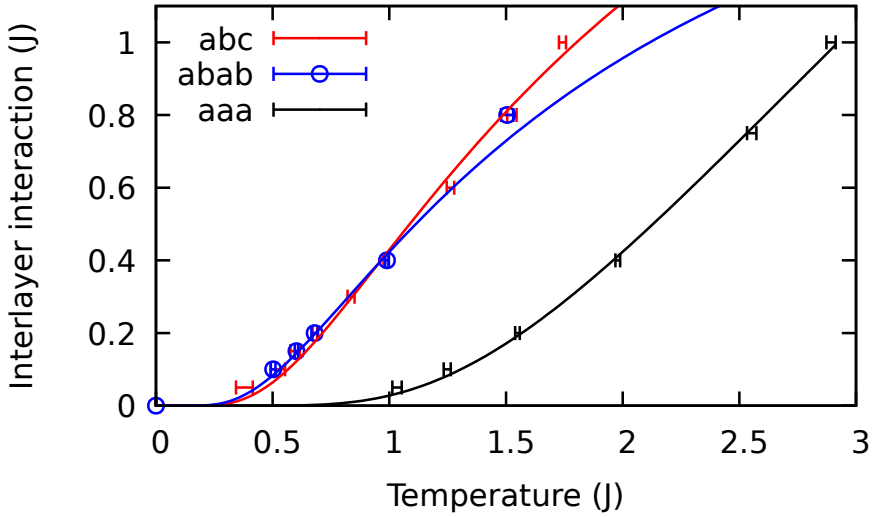

Figure 8.1: Phase boundaries for the unfrustrated (*aaa*) and frustrated (*abc* and *abab*) stackings. Points: data from Monte Carlo simulations. Lines: fits to height model theory of Chapters 6, 7.

where we have used the expressions for correlation lengths as derived in Chapter 7. The length scale ℓ for strongly coupled layers is $\ell \sim (\beta J_\perp)^{-2}$. Writing the phase transition condition in terms of $J_\perp$, we have

$$(\beta J_\perp)^2 \sim \left(e^{-4\beta J}\right)^{10} (\beta J_\perp)^{-20}, \tag{8.4}$$

$$J_\perp \sim J e^{-20\beta J/11}. \tag{8.5}$$

For the *abab* stacking, the equivalent expression is modified due to the difference in expressions for $\xi_z, \xi_\perp$. As expected, the boundary does not vary much

$$J_\perp \sim J e^{-5\beta J/3}. \tag{8.6}$$

The crossover to the conventional paramagnetic behaviour is given by the same expression for both frustrated stackings and arises from requiring that $y \sim \kappa_\perp \sim 1$, i.e. the tendency to disorder balances the coupling between layers. This boundary is given by $J_\perp \sim J e^{-2\beta J}$.

We note that the unfrustrated stacking, *aaa*, has an ordering transition which is expressed by the same condition as the crossover to the conventional paramagnet for

Stacking	c-fit	theory
aaa	5.44 ± 0.2	6.0
abc	1.90 ± 0.08	$20/11 \approx 1.82$
$abab$	1.63 ± 0.11	$5/3 \approx 1.67$

Table 8.1: Values of fit parameters for phase boundaries. For the fit parameter A, the values for the aaa, abc, $abab$ stackings, respectively, are $6.43 \pm 0.5, 2.87 \pm 0.2, 2.16 \pm 0.27$.

the frustrated stackings. That is, we simply require $y \sim \kappa_3 \sim 1$. In the unfrustrated stacking, the vortex-antivortex pairs do not play a role and we obtain the boundary $J_\perp \sim Je^{-6\beta J}$.

The classical spin-liquid regime, characterised by an absence of long-range order but strong correlations within and between layers, is given by

$$Je^{-2\beta J} \lesssim J_\perp \lesssim Je^{-c\beta J}, \tag{8.7}$$

for $c = \frac{20}{11}, \frac{5}{3}$ in the abc and $abab$ stackings respectively. In Fig. 8.1, we have reproduced Fig. 5.3 for convenience. The solid lines shown are fits to the function $J_\perp = AJe^{-c\beta J}$. The values of c for the various stackings are compared with the predicted values in Table 8.1. We conclude that the predictions from the analysis of vortex-antivortex pairs and the locking terms are in very good agreement with the numerical results.

8.2 Summary and Outlook

Using three different approaches, we have elucidated the classical spin-liquid regime in STLIAFMs. We started with the self-consistent Gaussian approximation that builds on the ideas of using mean-field theory. We then presented comprehensive numerics, via parallel tempering Monte Carlo simulations, which show additional evidence and support for the classical spin-liquid regime. Lastly, we have described a mapping to a scalar height field, which allowed for a perturbative analytical approach via the Renormalisation Group. These three methods give a consistent picture within the paramagnetic phase of the STLIAFMs: there is a classical spin-liquid regime over a broad temperature range when interlayer couplings are weak. This regime is characterised by strong correlations throughout the system, but no long-range order.

There are two main possibilities for future investigations of these systems. One of these is a more careful incorporation of the details of the experimental systems. This could include, for example, the bilayer structure of the stacking or the magnetic degrees of freedom which are also present. Another potential avenue of investigation is the ordering transition. From preliminary results, the nature of the transition is not immediately straightforward. It appears possible that, for weak interlayer coupling, there is a series of first-order transitions closely spaced in temperature, rather than a single ordering transition. This may be reasonable given the macroscopic degeneracy and near-degeneracy of states.

In the classical spin-liquids seen here, frustration is the crucial element that allows for the emergence of a cooperative paramagnet regime. Although quenched disorder is absent from these problems, the classical spin-liquids are characterised by the striking fact that they resist long-range order despite strong correlations.

Part III

Disorder

Chapter 9

Disordered and Driven Systems

In this part of the thesis, we study driven Anderson insulators. In this chapter, we begin with a broad discussion of Anderson insulators and localisation. We also briefly describe some tools and ideas that we will use to study driven quantum systems. Lastly, at the end of this chapter, we give a detailed outline of the rest of Part III.

9.1 Anderson Localisation

The term "disorder" has numerous connotations and implications, depending on context. In particular, we contrast the ideas of quenched and annealed disorder. A model exhibits annealed disorder when some of the parameters defining it are random variables which are determined by Boltzmann distributions. We will focus on systems that have quenched disorder. Systems with quenched disorder are defined by parameters which are random variables that remain fixed with respect to the degrees of freedom and are drawn from a distribution that we imagine is determined in the preparation of the sample. We focus on models that were introduced by Anderson in the study of transport in quantum systems [51]. Anderson sought to provide an explanation of experiments on silicon semiconductors with impurity doping. These experiments measured extremely long relaxation times for electron spins. With some caveats, his claim was that in the presence of disorder, after an infinite amount of time, a particle will be found some distance x away with a probability that tends to zero as x goes to infinity.

To study these materials, Anderson introduced a heavily simplified model which

remains one of the starting points for the study today. The phenomenon of "Anderson localisation" describes fermions in a disordered potential whose eigenstates decay exponentially in space. Specifically, Anderson studied a tight-binding model of fermionic particles with short-range, translationally-invariant hopping, $\lambda_{i,j}$, and uniformly distributed (on $[-W, W]$) on-site potentials, w_i. We introduce a further simplification by studying nearest-neighbour hopping, λ. Our Hamiltonian in one dimension is

$$H = \sum_i w_i c_i^\dagger c_i - \lambda \left(c_i^\dagger c_{i+1} + \text{h.c.} \right). \tag{9.1}$$

Anderson's treatment of this problem involves perturbation theory to all orders, but we will present some coarser arguments to justify the phenomenon of localisation. We start by considering the limit in which $\lambda \ll W$. The expected difference between on-site potentials of nearest-neighbours is $w_i - w_{i+1} \propto W \gg \lambda$. We expect some hopping between neighbouring sites for on-site energies within λ of each other. With bandwidth $2W$, we can estimate the hopping amplitude between sites separated by x lattice spacings as $\sim \lambda \left(\frac{\lambda}{2W}\right)^x \sim \lambda e^{-\frac{x}{\xi}}$. In the limit of very small $\frac{\lambda}{2W}$, this hopping will lead to wavefunctions which are exponentially localised, $|\psi(x)| \propto e^{-\frac{x}{\xi}}$.

Naturally, one can ask about the robustness of this result. We might think that since in a large system there will be states very close in energy, small perturbations can easily mix these localised states. From first-order perturbation theory, we can see that this will not be possible. The change of a wavefunction ψ_σ for a perturbation ΔH is given by

$$\Delta\psi_\sigma = \sum_\alpha \frac{\langle \psi_\sigma | \Delta H | \psi_\alpha \rangle}{\epsilon_\sigma - \epsilon_\alpha} \psi_\alpha. \tag{9.2}$$

Obviously one might expect that this could be large for nearly degenerate eigenvalues. Specifically, for a density of states per unit energy and volume, ρ, we expect the minimal energy difference for states separated by x sites to be $\left(\rho x^d\right)^{-1}$, where d is the dimension of the system. However, as we expect the matrix elements to decay exponentially, the contributions do not prevent self-consistently having a band

of localised states. In particular, we see that although the energy difference in the denominator may be small, the matrix element in the numerator is smaller.

9.1.1 Scaling Argument for Localisation

We turn to one of the tools mentioned earlier: scaling analysis. The scaling analysis of these systems provides intuition for the manner in which disorder affects macroscopic properties. Scaling analysis is concerned with the changes in physical properties due to changes in the system length scale. One advantage of this approach is that it makes clear the dependence on spatial dimensionality. We will present the argument for general dimension, d, but avoid considering the details of $d > 1$.

Edwards and Thouless [52] suggested the following criterion for detecting localisation. In the strongly-localised regime, the system should not be sensitive to changes in boundary conditions. In particular, the ordered energy levels will not shift very much if boundary conditions are changed (e.g. from $\psi(N) = \psi(0)$ to $\psi(N) = -\psi(0)$). On the other hand, if an eigenstate is extended, changes in the boundary condition will significantly affect the energy levels. To examine the degree of localisation in a system, Edwards and Thouless studied the ratio of the mean energy shift, $\overline{\Delta E}$ to the level spacing, η, and expressed this quantity in terms of the d.c. conductivity, σ.

$$\frac{\overline{\Delta E}}{\eta} \propto \frac{\sigma L^{d-2}}{e^2/h}. \tag{9.3}$$

Then, the so-called "Gang of Four" [53] formulated a renormalisation group analysis based around this quantity. Specifically, they discuss the behaviour of the dimensionless conductance as a function of the scale L

$$g(L) \equiv \frac{G(L)}{e^2/h}, \tag{9.4}$$

where $G(L)$ is the conductance of a sample with linear dimension L. The crucial assumption is that the macroscopic properties of the system depend only on the properties of a small sample as characterised by its conductance. That is, if we have a cube of material L^d, the properties of a cube of size $(2L)^d$ depend only on the

properties of the first cube. In other words, we assume the scale-dependence of the dimensionless conductance, g, is a function of g only,

$$\frac{\partial \ln g}{\partial \ln L} = \beta(g). \tag{9.5}$$

We start by considering the basic electronic properties of the system and the dependence of these properties on system size deep in the clean and disordered limits. In particular, we can imagine that in the limit of very weak disorder the system is essentially metallic. In this limit, $g \gg 1$, and we assume the conductance depends on scale in the usual way, $G \propto \sigma L^{d-2}$. In the opposite limit, corresponding to strong disorder $g \ll 1$, the drop-off in the amplitude of the wavefunction will be exponential in distance and we expect a similar drop-off for the conductance; explicitly, we take $g \propto e^{-\frac{L}{\xi}}$. We can use these two limits of $g(L)$ to determine the scaling behaviour. We have

$$\frac{\partial \ln g}{\partial \ln L} = d - 2, g \gg 1, \tag{9.6}$$

$$\frac{\partial \ln g}{\partial \ln L} = -\frac{L}{\xi} = \ln g, g \ll 1. \tag{9.7}$$

Now we make another assumption that turns out to be correct, but for which we will not provide justification here. We assume that one can interpolate between the two limits in a monotonic fashion. For $d = 1$, the result is straightforward. We see that $\beta(g)$ is always negative. Consequently, we expect large systems will always flow to the limit of $g \ll 1$, regardless of the starting value for g. Hence, for $d = 1$, we expect eigenstates in disordered systems of this kind will always be localised.

For $d > 1$, the situation is more complicated. The $d = 2$ case is "marginal" and we can see that the conductance does not change with L in the limit $g \gg 1$. It is reasonable to guess that $\beta(g)$ is monotonic and so the systems should always flow to the localised limit for $d = 2$.

For $d > 2$, we expect two phases. In particular, $\beta(g) = 0$ for $g = g_c$ and when $g > g_c$, the system flows to the delocalised limit, $g \gg 1$. At the point $g = g_c$, the conductance does not depend on the system size. When $g < g_c$, the system flows to

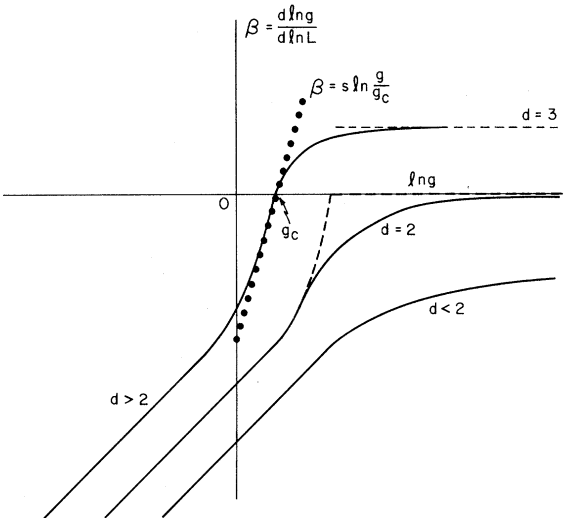

Figure 9.1: Figure from [53]. Plot of $\beta(g)$ vs. $\ln g$ for $d < 2, d = 2, d > 2$. Justification for smooth, monotonic interpolation between the two limits is omitted.

the localised limit as $\beta(g) < 0$. This is related to the idea of a "mobility edge" which refers to an energy at which eigenstates are localised or extended. The scaling theory suggests that there is no mobility edge in $d \leq 2$ and that there is such a feature in $d > 2$.

9.1.2 Transfer Matrices and Localisation

When $d = 1$ and we consider a tight-binding Anderson model, one can also use a transfer matrix formalism. This provides a compact way of seeing the exponential decay of the eigenstates as a function of position. Consider a semi-infinite, tight-binding, single-particle Hamiltonian

$$H = \sum_{k \geq 0} w_k |k\rangle\langle k| - \lambda \left(|k+1\rangle\langle k| + |k\rangle\langle k+1| \right), \tag{9.8}$$

where $w_k \in [-W, W]$, λ is nearest-neighbour hopping, and $\{|k\rangle\}$ is the position-space basis. Now we expand an eigenstate $|\psi\rangle$ in the position basis and write the Schrödinger equation component-wise. We have an equation in terms of transfer matrices and can use this to express the solution in terms of a_0, a_1, where a_k are the

complex amplitudes in an expansion of the solution in the position basis.

$$Ea_k = w_k a_k - \lambda \left(a_{k-1} + a_{k+1}\right), \tag{9.9}$$

$$\begin{pmatrix} a_{k+1} \\ a_k \end{pmatrix} = \begin{pmatrix} \frac{w_k - E}{\lambda} & -1 \\ 1 & 0 \end{pmatrix} \begin{pmatrix} a_k \\ a_{k-1} \end{pmatrix}, \tag{9.10}$$

$$T_k \equiv \begin{pmatrix} \frac{w_k - E}{\lambda} & -1 \\ 1 & 0 \end{pmatrix}, \tag{9.11}$$

$$\begin{pmatrix} a_{n+1} \\ a_n \end{pmatrix} = \prod_i T_i \begin{pmatrix} a_1 \\ a_0 \end{pmatrix}. \tag{9.12}$$

At this point we appeal to mathematical results on random matrices [54–56]. While we avoid discussing the finer details of the assumptions for these results, we note that the T_i are reasonably simple matrices: they are independently distributed and have finite entries. In particular, they have ± 1 on the off-diagonal. We are given the following expression involving the product of transfer matrices

$$\lim_{n\to\infty} \frac{1}{n} \ln \| T_n T_{n-1} \dots T_1 \| = \frac{1}{\xi} > 0, \tag{9.13}$$

where ξ is the localisation length and $\|A_{ij}\| = \max_i \sum_j |A_{ij}|$. In other words, the weight of the wavefunction $|a_i|$ is exponentially decaying with localisation length ξ.

9.1.3 Localisation and Numerics

For a tight-binding model as described above, it is straightforward to see the localisation of wavefunctions from numerics. We can diagonalise the Hamiltonian for a particular disorder realisation and plot the magnitude of the wavefunctions. In Fig. 9.2, for a range of disorder strengths, W, we plot eigenstates taken from the middle of the band. We can immediately see that these are localised to varying degrees.

Although we have focused on systems with $d = 1$ later in this work, the essential feature we rely upon is the existence of a localised regime. While we have presented a reasonably clear picture of Anderson localisation above for single-particle, isolated systems, there are many natural questions one may ask about this phenomenon. One obvious extension is the inclusion of interactions. The presence of interactions

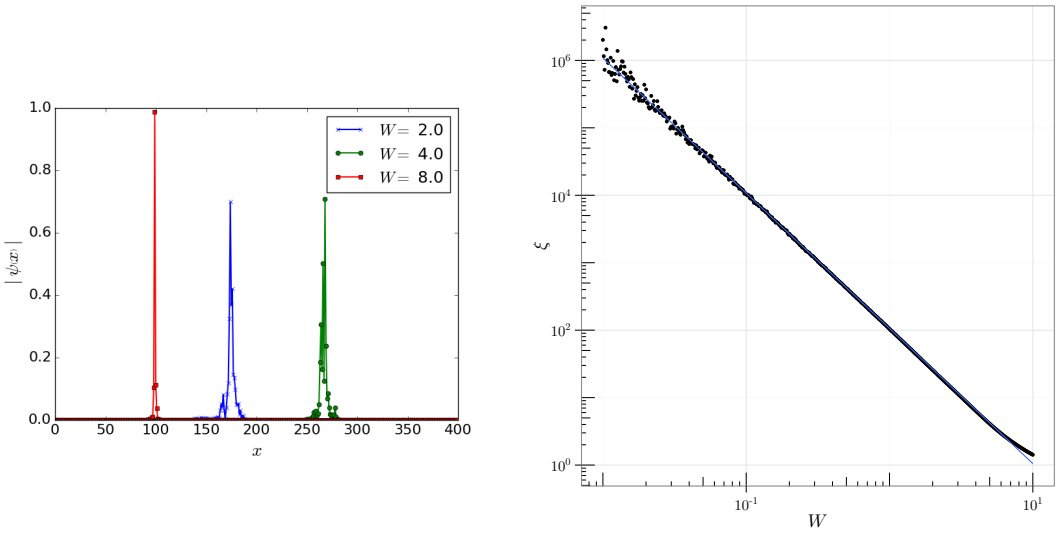

Figure 9.2: (left) Plot of $|\psi(x)|$ for various disorder strengths in system with 400 sites. Eigenstates from the middle of the band are plotted. $\lambda = 1, W = 2, 4, 8$. (right) Figure from [57]. Plot of localisation length as a function of disorder strength, W. The notation W used in [57] corresponds to $2W$ with $\lambda = 1$ in our notation.

brings the Pandora's box of many-body localisation [58–63], which we do not dare open here. Another question is how these systems respond to external driving or perturbations. This question constitutes the area of focus for Part III. Lastly, one may ask for experimental evidence. We do not discuss the experiments in detail, but will list some examples: evidence for Anderson localisation ranges from studies of the same material that inspired Anderson, doped silicon [64] to more recent ultracold atom experiments [65].

9.2 Driving and Response in Quantum Systems

In this section we present background on driven quantum systems. In this section, we discuss Floquet theory, a formalism for studying the dynamics of periodically driven, isolated, quantum systems. We will see that Floquet theory provides a useful means for both thinking about physical systems conceptually and extracting concrete details about the long-time behaviour of systems.

The dynamics of quantum systems are given by the unitary evolution from the

Schrödinger equation. This time-evolution is conceptually simple for time-independent Hamiltonians. Time-dependent systems are, in general, far more complicated. However, Hamiltonians which are periodic in their time-dependence admit some simplification in their dynamics. These systems are highly relevant from a physical perspective; for example, models subjected to periodic electromagnetic fields are examples of such systems. More broadly, renewed focus on localisation and quantum thermalisation has underscored the importance of understanding non-equilibrium systems and possible characteristics. Floquet systems constitute a class of non-equilibrium systems with some relatively simple properties and significant physical importance.

Although Floquet [73] preceded Bloch [74] by nearly fifty years, Bloch's theorem is probably more widely known amongst condensed matter physicists. Despite this, there is a direct mathematical analogy between the two. Bloch's theorem in spatially periodic systems, e.g. crystals, applies in precisely the same fashion for temporally periodic Hamiltonians. Specifically, given a Hamiltonian, $H(t) = H(t+T)$, Schrödinger's equation

$$i\frac{d|\psi(t)\rangle}{dt} = H(t)\,|\psi(t)\rangle, \tag{9.14}$$

$$\tag{9.15}$$

has solutions of the form

$$|\psi_\alpha(t)\rangle = e^{-i\epsilon_\alpha t}|\phi_\alpha(t)\rangle, \tag{9.16}$$

where ϕ_α are periodic, $|\phi_\alpha(t)\rangle = |\phi_\alpha(t+T)\rangle$, and ϵ_α are real and uniquely defined up to multiples of $\frac{2\pi}{T}$. In analogy with Bloch modes in crystals, we have Floquet eigenstates and quasienergies. Continuing the direct analogy, one can think of the quasienergies in a periodic way, $0 < \epsilon_\alpha \leq 2\pi/T$, just one does with quasimomentum in the Brillouin zone.

One of the key conceptual simplifications that the Floquet theorem provides is revealed by considering the unitary time-evolution operator for a single period. If we consider this operator in the usual sense, where $U(T+t,t)$ denotes time-evolution

according to the Schrödinger equation from time t to time $t+T$, then we can see

$$|\psi_\alpha(T)\rangle = U(T,0)\,|\psi_\alpha(0)\rangle, \tag{9.17}$$

$$|\psi_\alpha(T)\rangle = e^{-i\epsilon_\alpha T}|\phi_\alpha(T)\rangle = e^{-i\epsilon_\alpha T}|\psi_\alpha(0)\rangle, \tag{9.18}$$

where we have used the definition of time-evolution in the first line and then the properties of the Floquet eigenstates. We now define the Floquet Hamiltonian, H_F,

$$e^{-iH_F T} \equiv U(T). \tag{9.19}$$

From the above, we can see that the Floquet modes, $|\phi_\alpha(0)\rangle$, are eigenstates of H_F with eigenvalues ϵ_α. By studying the Floquet Hamiltonian, we can extract information about the system at long times. In particular, when observing stroboscopically, we have an essentially time-independent problem. Unfortunately, though, the Floquet Hamiltonian is not so easy to deal with. Computing the Floquet Hamiltonian is obviously non-trivial to do exactly because it is equivalent to computing time-evolution for a time-dependent system. While there are procedures for approximating H_F, we find it most fruitful to construct it numerically.

To demonstrate a convenience of Floquet formalism, we evaluate the time-dependence of observables. We start with a time-periodic Hamiltonian, $H(t) = H(t+T)$. Given an observable, $\mathcal{O}(t)$ and initial state $|\psi_0\rangle$, we wish to evaluate

$$\langle\mathcal{O}(t)\rangle = \langle\psi_0|U^\dagger(t)\,\mathcal{O}(t)\,U(t)|\psi_0\rangle, \tag{9.20}$$

where $U(t)$ is the unitary time-evolution operator from time 0 to t. Expressing $t = nT + s$ and using the periodicity, we can write

$$\langle\mathcal{O}(t)\rangle = \langle\psi_0|\left[U^\dagger(T)\right]^n U^\dagger(s)\,\mathcal{O}(t)\,U(s)\,[U(T)]^n|\psi_0\rangle. \tag{9.21}$$

Using the Floquet Hamiltonian and writing $U^\dagger(s)\,\mathcal{O}(t)\,U(s) \equiv \mathcal{O}^s$, we have

$$\langle\mathcal{O}(t)\rangle = \langle\psi_0|e^{iH_F nT}\mathcal{O}^s(t)\,e^{-iH_F nT}|\psi_0\rangle. \tag{9.22}$$

We can take advantage of the complete basis of Floquet eigenstates and insert two resolutions of the identity operator

$$\langle\mathcal{O}(t)\rangle = \sum_{\alpha,\beta}\langle\psi_0 \mid \alpha\rangle e^{i\epsilon_\alpha nT}\langle\alpha|\mathcal{O}^s(t)|\beta\rangle e^{-i\epsilon_\beta nT}\langle\beta \mid \psi_0\rangle. \tag{9.23}$$

If we had started with a many-body initial state of Slater determinants in the $t = 0$ Hamiltonian eigenbasis, we could express this expectation value in terms of the occupation, n_i, of the ith eigenstate

$$\sum_{\alpha,\beta,i} \mathcal{O}^s_{\alpha\beta}(t)\, e^{inT\left(\epsilon_\alpha - \epsilon_\beta\right)} V_{\alpha i} V^\dagger_{i\beta} n_i, \tag{9.24}$$

where $V_{\alpha,i}$ is the unitary mapping between the Floquet eigenbasis and the $t = 0$ basis for Slater determinants.

Both of these expressions yield a significant simplification in the limit of long times. Explicitly, we define the limit of $t \to \infty$ by averaging over many cycles. Through this averaging, terms will vanish unless unless $\alpha = \beta$. This is the so-called "diagonal" ensemble. For a time-independent observable, or a periodically defined observable

$$\langle \mathcal{O}(t \to \infty) \rangle \equiv \lim_{N\to\infty} \frac{1}{N} \sum_{n=1}^{N} \langle \mathcal{O}(nT) \rangle = \sum_\alpha |\langle \psi_0 \mid \alpha \rangle|^2 \langle \alpha | \mathcal{O} | \alpha \rangle. \tag{9.25}$$

From the above, it is clear that the Floquet formalism, specifically the Floquet eigenstates, can be used to compute the long-time behaviour and get information about, for example, questions of thermalisation. As an example, one can have Floquet modes localised in the space of energy eigenstates of $H(t = 0)$ [75, 76]. Instead of continual absorption of energy until reaching an infinite-temperature thermal state, in the presence of Anderson localisation, it is possible that systems reach a steady state with finite energy density.

9.3 Outline of Part III

In the rest of Part III, we will study Anderson insulators in the strongly localised regime and with periodic, monochromatic drives. In Chapter 10, we give some background on previous work related to this topic, introduce the specific models we consider, and describe the numerical techniques we use. Next, in Chapter 11, we directly investigate the linear response regime and frequency dependence of conductivity. We show that this is consistent with the Mott law results. Then, in Chapter 12, we

investigate the breakdown of linear response and the development of non-linear response in the strong-driving regime. We also characterise these periodically driven systems at long times. In particular, we describe a regime with adiabatic crossings in instantaneous energy levels. Systems in this regime exhibit periodic non-local charge rearrangement similar to the rearrangements described in [77]. Throughout, we support our claims with results from numerical simulations of these systems in both linear and non-linear response regimes and describe the short- and long-time behaviour.

Chapter 10

Floquet-Anderson Insulators

The Anderson insulator is one of the simplest models of the quantum phenomenon of localisation [51]. In one dimension and at zero temperature, for any amount of disorder, it exhibits vanishing d.c. conductivity. The linear response when a monochromatic, oscillating electric field is applied is characterised by the celebrated Mott form for the a.c. conductivity [79]. We will study the Anderson insulator beyond linear response and describe the features at both long times and strong periodic driving.

Joule heating refers to the idea that electric current flowing through a conductor generates heat [80]. We will extract the a.c. conductivity directly by observing this heating. In many situations, a system is coupled to a bath and so heating can continue and the system will absorb energy steadily at long times. However, in isolated systems, this regime must break down and cross over to a long-time regime. We refer to the behaviour at long times as the Floquet regime and one objective of our work is to characterise the physical nature of the Floquet regime.

When the framework of time-dependent perturbation theory breaks down, we will introduce the Landau-Zener formalism. Using a combination of analytic techniques and numerical diagonalisation, we identify several dynamical regimes in the parameter space of driving amplitude and frequency. In particular, we predict that there is a non-linear adiabatic regime which exhibits non-local properties.

The two systems we study are differentiated by the nature of the periodic drive that is applied. In one case, we consider periodically driving with a spatially local potential and in the other case we consider applying a uniform, monochromatic electric field. We will consider zero-temperature systems, except in Chapter 12, where

we consider the evolution of individual eigenstates. In the rest of this chapter, we briefly outline some of the previous work on driven, disordered systems and some of the details of the numerical set-up we have used.

10.1 Previous work

When discussing previous work on periodically driven Anderson insulators, the results from Mott (reviewed more carefully in Chapter 11) are likely the most well-known. Mott's work describes the linear response regime and gives the low-frequency behaviour of the conductivity [79]. Since then, there have been many attempts to understand localised systems and time-dependent perturbations.

Saso [81] performed detailed numerics to reproduce the Mott law (more specifically, prefactors from Berezinskii [82]). Saso's work uses the Kubo-Greenwood formula from linear response theory (rather than Joule heating) to compute the conductivity. In [75], Gefen and Thouless study a one-dimensional system with random potentials subject to a constant electric field. They use the Landau-Zener formalism to treat level crossings, show that energy absorption saturates, and demonstrate that the Floquet eigenstates (introduced in Chapter 9) are localised in the basis of $t = 0$ energy eigenstates.

Other studies have used random matrices as models for disordered physical systems, and have demonstrated relationships between energy absorption and drive amplitude and frequency [83, 84] and that energy absorption can saturate when the eigenstates of the evolution operator are localised [85]. [86] uses a random matrix Hamiltonian and periodic driving to show that linear response breaks down. In [76], the authors study a generic quantum system perturbed by d incommensurate driving frequencies and show that under certain conditions these systems exhibit saturation in energy absorption due to localisation.

Very recent work has also studied localised, driven systems. This has mostly been in the context of many-body localisation [87, 88], but has also utilised Landau-Zener formalism to treat energy level crossings [88]. This work considered interacting

models, which require far more computational resources to simulate, and so only studied systems of size $L = 12$. Other work has considered adiabatic, time-dependent perturbations and the response to such perturbations [77].

Work by Shirley used the Floquet formalism to study driven two-site systems [89]. Shirley studies the two-site Rabi problem [90], which we discuss in 11.2, without using the Rotating Wave Approximation (RWA). Shirley's work uses the Floquet theorem to rewrite the two-site Hamiltonian in terms of an infinite-dimensional Hamiltonian. Shirley did not, however, consider disordered systems in this work.

There is a growing body of experimental work investigating the response of localised quantum systems to periodic driving in ultracold atomic gases. Experiments by the Bloch group have studied the effects of driving an interacting, localised system [72, 91]. Other recent experiments have begun to combine localised systems and periodic driving outside of ultracold atoms, instead in trapped ions and nitrogen vacancy systems. These experiments have sought rather exotic forms of matter which we will not discuss here [92–95].

10.2 Models and Numerical Simulation

We study two models of periodically driven Anderson-localised systems in this work. Though similar, each has its own conceptual and practical advantages. One model is an Anderson insulator with periodic driving at a single location. The other is an Anderson insulator driven by a uniform monochromatic electric field. We study both models at zero temperature and finite fermion density.

We consider these models in the continuum and on a lattice. For systems in the continuum, we assume $\mathcal{H}_0$ is a one-dimensional, undriven, Anderson insulator Hamiltonian. We denote the localisation length ξ and the density of states per unit energy and length ρ. $\mathcal{H}_0$ is driven with a local oscillating potential or a global electric

field. The full continuum versions of the Hamiltonians are

$$\mathcal{H}_{SSD}(t) = \mathcal{H}_0 - v\delta(x - x_d)\sin(\omega t), \tag{10.1}$$

$$\mathcal{H}_{GD}(t) = \mathcal{H}_0 - eE_0 x \sin(\omega t), \tag{10.2}$$

where SSD stands for single-site drive and GD stands for global drive. The level spacing within a localisation length is given by $\Delta_\xi = (\rho\xi)^{-1}$. We can define dimensionless parameters for this problem as follows

$$\Omega \equiv \hbar\omega\xi\rho = \frac{\hbar\omega}{\Delta_\xi}, \tag{10.3}$$

$$\mathcal{E}_{SSD} \equiv v\rho = \frac{v}{\xi\Delta_\xi}, \tag{10.4}$$

$$\mathcal{E}_{GD} \equiv eE_0\rho\xi^2 = \frac{eE_0\xi}{\Delta_\xi}. \tag{10.5}$$

In order that we do not probe transitions within a localisation volume, we take $\Omega \ll 1$. To avoid distorting the non-resonant zero-field eigenstates, we take $\mathcal{E}_{SSD,GD} \ll 1$.

The lattice Hamiltonians describe one-dimensional, tight-binding fermions with on-site disorder. The Hamiltonians are

$$H_{SSD}(t) = \sum_i \left[-\lambda\left(c_i^\dagger c_{i+1} + \text{h.c.}\right) + w_i c_i^\dagger c_i\right] + \hat{v}(t), \tag{10.6}$$

$$H_{GD}(t) = \sum_i \left[-\lambda\left(e^{i\Phi(t)} c_i^\dagger c_{i+1} + \text{h.c.}\right) + w_i c_i^\dagger c_i\right], \tag{10.7}$$

where w_i are uniformly distributed in $[-W, W]$, and $\lambda \ll W$. ω is the driving frequency, $\hat{v}(t) = v\sin(\omega t)\, c_d^\dagger c_d$ is the local potential at site d, and $\Phi(t) = \phi_0 \cos(\omega t)$.

The Peierls substitution is a means of including an electromagnetic potential in a tight-binding model [96] by introducing a phase factor in the hopping terms. We can see the effect of our time-dependent hopping more clearly by considering a single particle situation. If we expand the wavefunction in terms of the lattice basis (with amplitude a_i on site i) and write the Schrödinger equation

$$|\psi\rangle = \sum_i a_i |i\rangle, \tag{10.8}$$

$$i\frac{\partial a_k}{\partial t} = \lambda e^{-i\Phi(t)} a_{k-1} + \lambda e^{i\Phi(t)} a_{k+1} + a_k \epsilon_k, \tag{10.9}$$

we can then make the gauge transformation, $a_k \to b_k e^{-ik\Phi}$. Now we see that the resulting equations have a time-dependent, spatially uniform electric field represented in this gauge by a scalar potential

$$i\frac{\partial b_k}{\partial t} = \lambda b_{k-1} + \lambda b_{k+1} + b_k \epsilon_k - k\frac{\partial \Phi}{\partial t} b_k. \tag{10.10}$$

For $\Phi(t) = \phi_0 \cos(\omega t)$, we have an applied electric field of $\phi_0 \omega \sin(\omega t)$.

We define the following quantities that will be used to describe the behaviour of the systems. Stroboscopic normalised energy absorption is defined by

$$\Delta E(nT) \equiv \frac{\langle \psi(t = nT) | \mathcal{H}_0 | \psi(t = nT) \rangle - E_0}{E_\infty - E_0}, \tag{10.11}$$

where $t = nT$ is a multiple of the drive period, E_∞ is the energy at infinite temperature and E_0 is the energy at $t = 0$. When the system is at infinite temperature, we expect this quantity to be 1. We will also consider the occupation as a function of energy, $n(\epsilon, t)$, where this is the average number of particles with energy ϵ at time $t = nT$. We write the change in occupation, relative to $t = 0$, as

$$\delta n(\epsilon, t) \equiv \begin{cases} n(\epsilon, t = 0) - n(\epsilon, t), & \epsilon < 0 \\ n(\epsilon, t) - n(\epsilon, t = 0), & \epsilon > 0, \end{cases} \tag{10.12}$$

where we recall that since we typically consider initial states at zero-temperature, with chemical potential zero, $n(\epsilon, t = 0)$ will be a Heaviside theta function, $\theta(-\epsilon)$. We will also consider $n(x, t)$, where this is the average occupation of a site x at time t.

We study the systems described above via numerical simulations. The two models for Floquet-Anderson insulators are highly amenable to numerical analysis.

Now we review the method used to compute the time-evolution for systems that have time-dependent Hamiltonians. Consider a general periodic Hamiltonian, $H(t) = H(t + T)$; we construct a piecewise-constant, discretised version of the Hamiltonian.

In particular, for $0 < t < T$,

$$H_{disc}(t) = \begin{cases} H(0), & t_0 = 0 \leq t < \frac{\Delta t}{2} \\ H(\Delta t), & \frac{\Delta t}{2} \leq t < \frac{3\Delta t}{2} \\ \vdots & \vdots \\ H(k\Delta t), & \frac{(2k-1)}{2}\Delta t \leq t < \frac{(2k+1)}{2}\Delta t \\ \vdots & \vdots \\ H(T-\Delta t), & T - \frac{3\Delta t}{2} \leq t < T - \frac{\Delta t}{2} \\ H(T), & T - \frac{\Delta t}{2} \leq t < T \end{cases} \tag{10.13}$$

where $\Delta t = \frac{T}{N+1}$, and so the Hamiltonian is evaluated at $N+1$ different times in the drive. We construct the time-evolution operator in the usual way,

$$U\left((2k+1)\frac{\Delta t}{2}, 0\right) = e^{-iH_{disc}(0)\Delta t/2} \prod_{m=1}^{k} e^{-iH_{disc}(m\Delta t)\Delta t}. \tag{10.14}$$

We compute the matrix exponentials above using the method in the SciPy library [97, 98]. This library uses a modified scaling and squaring algorithm.

In the limit $\Delta t \to 0$, this generates the dynamics of a system under a time-dependent Hamiltonian. However, within numerical simulations we must use a finite discretisation. One concern is that a piecewise-constant Hamiltonian will introduce higher-harmonic contributions to the problem. If the piecewise-constant approximation is too coarse, then we are effectively driving with square waves. These will contribute higher harmonics of the drive and lead to increased heating. Another concern is that the dynamics may have avoided crossings in the energy levels. If the discretisation is too coarse, the crossings will be traversed suddenly rather than according to the dynamics of the Hamiltonian.

To study the dependence on discretisation, we study the change of an observable with respect to progressively finer discretisation. In Figs. 10.1, 10.2 we present an illustrative analysis of some features of discretising time-evolution. We will see that when time-evolution is sufficiently discretised, the difference between an observable at discretisation N and a reference discretisation, r (chosen to be extremely fine), follows a power-law decay as a function of discretisation. A measurement is acceptable when the relative changes of an observable are sufficiently small and the power-law behaviour as a function of discretisation holds.

We show plots for the energy absorption in the global drive model at an arbitrary early time, ΔE, and also in the long-time limit, D. In Fig. 10.1, we vary ω and in Fig. 10.2, we vary ϕ_0. These are meant as representatives and similar behaviour holds both for other observables (e.g. average occupation) and the single-site drive model.

In Fig. 10.1, we study the long-time, "diagonal" approximation, D_N, as defined in Eqn. 9.25 (averaging over many periods), for the stroboscopic absorption at a particular discretisation, N. We see that for fine enough discretisation, $|D_N - D_r|$ follows a power-law dependence

$$\ln|D_N - D_r| \propto -k \ln N. \tag{10.15}$$

In Fig. 10.2, we examine the stroboscopic, normalised energy absorbed, ΔE_N at a given discretisation, N, over a wide range of field strength and discretisation. Because of the power-law convergence, we can control the discretisation error in our measurements. Explicitly, we discretise finely enough so that the change in the observables begins to obey the power-law decay. For example, from Fig. 10.1, when driving with a frequency $\omega = 0.05$, a discretisation of $N = 240$ would be acceptable.

We have used systems of size $L = 100$ throughout this work. The range for the frequency parameter ω is 0.02 to 0.45. For the single-site drive, we have considered from $v \approx 10^{-4}$ to $v \approx 5$. In the global drive model, we have studied from $\phi_0 \approx 10^{-4}$ to $\phi_0 \approx 20$, which corresponds to a maximum field amplitude, $\phi_0\omega \gtrsim 1$. Usually, we work with disorder strengths $W = 2, 5$. We estimate the localisation lengths to be ≈ 6 and ≈ 1 lattice spacings, respectively. We disorder average the quenched on-site potentials over 500 to $\sim 10^5$ realisations, depending on the regime of driving. The discretisation we use varies from $N = 160$ to $N = 600$.

Throughout the numerical sections of the following chapters, we will often display plots for either the single-site drive or global drive. When there are significant qualitative differences, we will present both and make a note of this. If the plots for both driving models are very similar, in an effort to streamline presentation, we will show results for just one of the models.

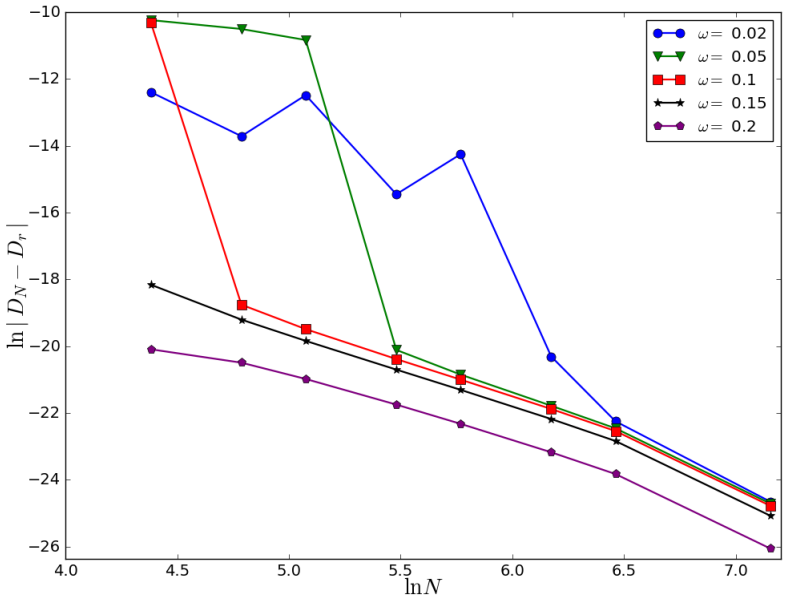

Figure 10.1: **(Global Drive)** Plots of the convergence of the diagonal approximation, or long-time limit, as defined in Eqn. 9.25, for energy absorption as a function of discretisation. We see that increasingly fine discretisation is required for the power-law decay of $|D_N - D_r|$ to set in as ω is reduced. The reference discretisation is $r = 1600$. When measuring observables, we use a discretisation fine enough so the power-law decay is applicable. $\phi_0 = 0.01, W = 5$.

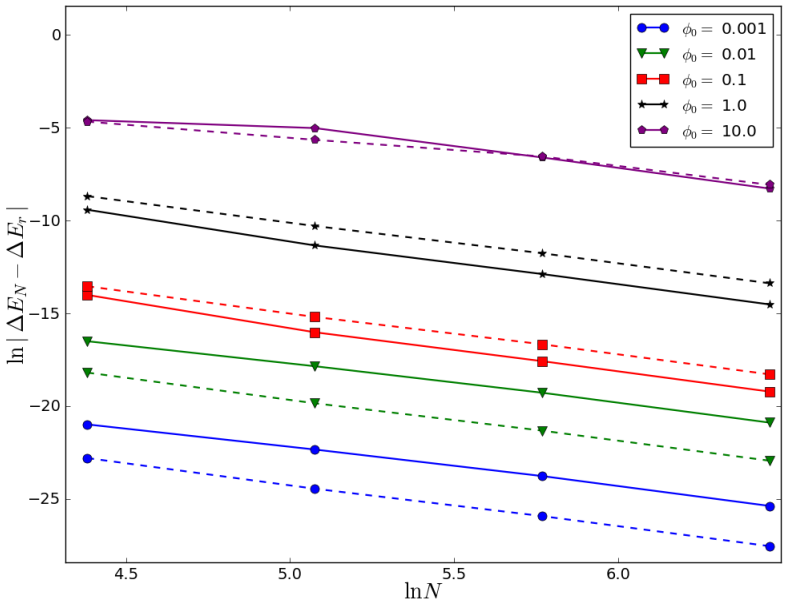

Figure 10.2: **(Global Drive)** Plots of the convergence of energy absorption as a function of discretisation. Solid and dashed lines indicate different disorder realisations. $\omega = 0.15$. Reference discretisation is $r = 1280$. Power-law decay is roughly $|\Delta E_N - \Delta E_r| \propto N^{-2.5}$. When $N = 160, \phi_0 = 0.01$, $|\Delta E_N - \Delta E_r|/\Delta E_r \approx 0.01\%$.

Chapter 11

Weak Driving

The well-studied regime of linear response in disordered conductors can be understood using time-dependent perturbation theory and the Golden Rule. In general, linear response theory seeks to understand the response of a system to a weak perturbation [99]. The underlying idea is that the response is linear in the perturbation. One can derive a Kubo formula [100] for a system with time-independent Hamiltonian, H_0, subject to a perturbation, $H'(t)$, turned on at time $t = t_0$. For a general observable, A, and a system in thermodynamic equilibrium, the linear response is

$$\delta\langle A(t)\rangle \equiv \int_{t_0}^{\infty} i\theta(t-t')\langle[H'_I(t'), A_I(t)]\rangle_0 dt', \tag{11.1}$$

where A_I is an operator in the interaction picture and $\langle\ldots\rangle_0$ is the unperturbed expectation in equilibrium. This formulation is extremely general and can be applied to compute the conductivity, which is the linear response coefficient for a system of charged particles perturbed by an electromagnetically induced current. However, we will extract the conductivity from the dynamical response of such a perturbation directly.

The applicability of linear response theory is at both short times and weak perturbations. We are concerned with the physics beyond both of these constraints in our study of Floquet-Anderson insulators. This chapter is focused on the case of weak driving, both in the short-time linear response regime and in the long-time limit, where the behaviour of these systems can be understood in terms of well-known results.

In this chapter, we first review the time-dependent perturbation theory that leads

to the Golden rule and show how this applies to the two models we consider. Then we consider an ensemble of two-level Rabi problems to extract the long-time behaviour in the weak driving regime. Next we turn to results of numerical simulations. We show that the Mott form of the a.c. conductivity can be extracted from the heating rate and discuss the mechanism for heating in this regime.

11.1 The Golden Rule and Mott Conductivity

The Golden Rule (often attributed to Fermi, but mainly owed to Dirac [78]) is a result from time-dependent perturbation theory that has remarkable versatility and applicability. Here, we give the statement and show how it can be used to make an argument that serves as one starting point for our work on Floquet-Anderson insulators. We follow the argument presented by Mott [79].

We would like to connect the idea of Anderson localisation with the behaviour of conductivity as a function of frequency. Mott computed the asymptotic form of the a.c. conductivity, $\langle \sigma(\omega) \rangle$, as $\omega \to 0$, and showed that this tends to zero. Although Mott used the Kubo-Greenwood formula [100] to compute the conductivity, one can equivalently compute it, as we will do here, using the Golden Rule to evaluate Joule heating.

Consider a one-dimensional Anderson insulator perturbed by a monochromatic field, $\mathcal{E}(t) = \mathcal{E} \sin(\omega t)$. This contributes a term $e\mathcal{E}x \sin(\omega t)$ to the Hamiltonian, $\mathcal{H}_0$. The Golden Rule states that the transition rate from an initial state, $|i\rangle$, with energy E_i to a final one, $|f\rangle$, with E_f is

$$R = \frac{2\pi}{\hbar} e^2 \mathcal{E}^2 |\langle f|\hat{x}|i\rangle|^2 \rho(E_f) V_f. \tag{11.2}$$

where V_f is volume occupied by the final states and $\rho(E_f)$ is the density of states per unit volume of the final states.

We consider two states localised on sites separated by x lattice spacings with on-site potentials w_0, w_x. From perturbation theory, one can see that the most significant contributions to the matrix element will come from pairs of states with splitting near

$E_i - E_f \approx \hbar\omega$. To study these, we take the following effective two-level system

$$H = \begin{pmatrix} w_0 & \lambda e^{-x/\xi} \\ \lambda e^{-x/\xi} & w_x \end{pmatrix}, \tag{11.3}$$

We will require splitting between eigenvalues of $\hbar\omega$ and define a length, x_{Mott},

$$\lambda e^{-x_{\text{Mott}}/\xi} \equiv \frac{\hbar\omega}{2}. \tag{11.4}$$

The splitting between eigenvalues in the two-level problem is $\sqrt{(w_0 - w_x)^2 + 4\lambda^2 e^{-2x/\xi}}$. We now consider all possible pairs by considering the distance separating them. If $x < x_{\text{Mott}}$, $2\lambda e^{-x/\xi} > \hbar\omega$ and so it will not be possible for the splitting to be $\hbar\omega$. If $x > x_{\text{Mott}}$, we will require $w_0 - w_x = \hbar\omega$. These will not contribute as the eigenstates are exponentially localised (giving a small matrix element) and there are a small number of them ($\propto$ const. in $d = 1$ and $\propto x^{d-1}$ in general).

Finally, we consider sites separated to within a lattice spacing of x_{Mott}. These yield a symmetric, anti-symmetric resonant pair of eigenstates $|\pm\rangle = \frac{1}{\sqrt{2}}(|0\rangle \pm |x_{\text{Mott}}\rangle)$ with matrix element $\langle +|\hat{x}|-\rangle^2 \sim \frac{x_{\text{Mott}}^2}{4}$. We account for all sites with separation x_{Mott} by including the factor of volume, which is just 1 in one dimension (or x_{Mott}^{d-1} in d dimensions).

We now compute the energy absorbed by these near-resonant transitions for a system at zero temperature with Fermi energy $E_F = 0$. The amount of energy absorbed or emitted near resonance is $\hbar\omega$ and $n(E)$ is the Fermi distribution function at zero temperature. There are no emission terms because we are at zero temperature. We also have a window of $\hbar\omega$ of states to excite. The net energy absorption rate is

$$W(t) = \omega\hbar\pi e^2 \mathcal{E}^2 V_f \sum_{i,f} \rho(E_i)\,\rho(E_f)\,|\langle f|\hat{x}|i\rangle|^2 n(E_i)\,[1 - n(E_f)], \tag{11.5}$$

$$\sim \omega^2 \mathcal{E}^2 \rho(E_i)^2\, x_{\text{Mott}}^{d-1}\left(x_{\text{Mott}}^2\right). \tag{11.6}$$

We then equate this to Joule heating to obtain the frequency-dependent conductivity

$$W(t) = \frac{1}{2}\mathcal{E}^2 \sigma(\omega), \tag{11.7}$$

$$\sigma(\omega) \sim \omega^2 x_{\text{Mott}}^{d+1} \sim \omega^2 \ln^{d+1}(\omega). \tag{11.8}$$

We see that this tends to zero as $\omega \to 0$ and so Mott's criterion for localisation holds up in the tight-binding Anderson model. We note that this result is problematic if one considers the long-time limit. We would expect that a closed system will eventually reach a steady state. In the following sections and chapters, we will explore the system in the long-time and strong-perturbation limits. However, we first consider the Mott argument in the case of a single-site drive.

11.1.1 Single-site Drive

Here we emphasise the difference between the single-site drive and the global drive by showing that the single-site drive has a different dependence on ω in the expression for energy absorption. We focus on the argument used to evaluate the matrix element above. We again begin by considering effective two-site systems. For a single-site drive, we can write

$$H(t) = \begin{pmatrix} w_0 & \lambda e^{-x/\xi} \\ \lambda e^{-x/\xi} & w_x \end{pmatrix} + \begin{pmatrix} 0 & 0 \\ 0 & V_{SSD}(t) \end{pmatrix}, \tag{11.9}$$

$$V_{SSD}(t) = v \sin(\omega t), \tag{11.10}$$

where $\lambda e^{-x/\xi}$ is the effective hopping amplitude introduced above. The key difference from the Mott argument above arises when evaluating the matrix element $|\langle f|V_{SSD}|i\rangle|^2$. In particular, there is not a factor of $\hat{x}$.

When considering all possible separations, x, of sites, one still finds that the strongest contributions come from pairs separated by $x = x_{\text{Mott}}$. However, the term proportional to x_{Mott}^2 led to the $\ln^2(\omega)$ dependence in the a.c. conductivity when applying a monochromatic, uniform electric field. Here, we do not have such a term and instead have

$$\Delta E \sim v^2 \omega^2, \tag{11.11}$$

where we have avoided writing $\sigma(\omega)$. That notation refers to Mott conductivity, which is the response to an electric field and not applicable for the single-site drive. We will see though, that the proportionality with ω^2 can still be extracted from the numerical simulations.

11.2 Long-time Limit from Rabi Problem

Of course, the linear response regime cannot continue indefinitely. In a closed, finite system, we expect an eventual steady state at long enough times. To study the long-time behaviour, one can treat the two-level system in the framework of the Rabi problem. We will review this treatment and discuss the behaviour of different disorder realisations that contain pairs of sites closer or further from resonance.

In the small amplitude regime, one can apply the rotating wave approximation (RWA) and use insights from the Rabi problem to understand the long-time limit for both the single-site drive and the global drive. Two sites that form an effectively on-resonance Rabi problem will dominate the long-time absorption; note that the condition of being near-resonance is necessary for the applicability of the RWA. Consider the Rabi Hamiltonian

$$H_R = \begin{pmatrix} E_a & 0 \\ 0 & E_b \end{pmatrix} + \begin{pmatrix} v_{aa} & v_{ab} \\ v_{ba} & v_{bb} \end{pmatrix} \sin(\omega t). \tag{11.12}$$

We write the wavefunction as

$$|\psi(t)\rangle = e^{-iE_a t} a(t) |a\rangle + e^{-i(E_a+\omega)t} b(t) |b\rangle. \tag{11.13}$$

The Schrödinger equation is then

$$\begin{aligned} i\partial_t \begin{pmatrix} a \\ b \end{pmatrix} = &\left[\frac{1}{2} \begin{pmatrix} 0 & v_{ab} \\ v_{ba} & 2\Delta \end{pmatrix} + \begin{pmatrix} v_{aa} & 0 \\ 0 & v_{bb} \end{pmatrix} \cos(\omega t) \right] \begin{pmatrix} a \\ b \end{pmatrix} \\ &+ \frac{1}{2} \begin{pmatrix} 0 & v_{ab} e^{-2i\omega t} \\ v_{ba} e^{2i\omega t} & 0 \end{pmatrix} \begin{pmatrix} a \\ b \end{pmatrix}, \end{aligned} \tag{11.14}$$

where $a = a(t), b = b(t)$, the detuning, Δ, is $E_b - E_a - \omega$, $v \equiv v_{ba} = v_{ab}$, and $\Omega^2 = \Delta^2 + v^2$. In the RWA, we neglect the oscillating terms and keep only a simple set of coupled linear differential equations. Solving gives the following probability amplitudes

$$|a(t)|^2 = \cos^2\left(\frac{\Omega t}{2}\right) + \frac{\Delta^2}{\Delta^2 + v^2} \sin^2\left(\frac{\Omega t}{2}\right), \tag{11.15}$$

$$|b(t)|^2 = \frac{v^2}{v^2 + \Delta^2} \sin^2\left(\frac{\Omega t}{2}\right). \tag{11.16}$$

We calculate the absorbed energy by assuming that the level E_a is initially occupied and so at time t, we have $\Delta E = (E_b - E_a)\,|b\,(t)|^2 = (\Delta + \omega)\,|b\,(t)|^2$.

We now consider the system in which this two-level problem resides. We have uniform disorder, so Δ is uniformly distributed. If we take ρ as the density of states at the Fermi energy, then we can count the number of effective two-level problems with detuning Δ. We expect $(\Delta + \omega)\,\rho$ such pairs. Thus, the total contribution to the absorption from these pairs is

$$\Delta E\,(t) = \rho\omega^2 \frac{v^2}{\Delta^2 + v^2} \sin^2\left(\frac{\sqrt{\Delta^2 + v^2}}{2} t\right), \tag{11.17}$$

where we have used the RWA again to write $\Delta + \omega \approx \omega$ because $\Delta \ll \omega$. We can integrate over Δ and consider the long- and short-time limits, again averaging over cycles as we have in the "diagonal approximation" for the long-time limit. This gives

$$\Delta E_{\text{long time}} \propto \rho\omega^2 v, \tag{11.18}$$

$$\Delta E_{\text{short time}} \propto \rho\omega^2 v^2 t, \tag{11.19}$$

where the time-scale which separates these regimes is $t_{sat} \sim \frac{1}{v}$. In both cases, the response is dominated by the limit of $\Delta \ll \omega$. So energy absorption will be dominated by the sine-squared behaviour characterised by a long period, $T \sim \frac{1}{v}$. This dominates the energy absorption at long and short times. In the numerical simulations, we will see this qualitatively through the presence of a long tail in the distribution of energy absorption over disorder realisations.

11.3 Numerical Results for Weak Driving

In this section, we investigate the linear response regime of the periodically driven Anderson insulators using numerical simulations. We start by showing that these systems behave according to the principles we have discussed above. In particular, we show that there is an absorption regime in which ΔE is linearly dependent on t. This linear absorption regime extends to large t when the driving strength is weak. We extract the frequency dependence by comparing the rate of heating for a range of

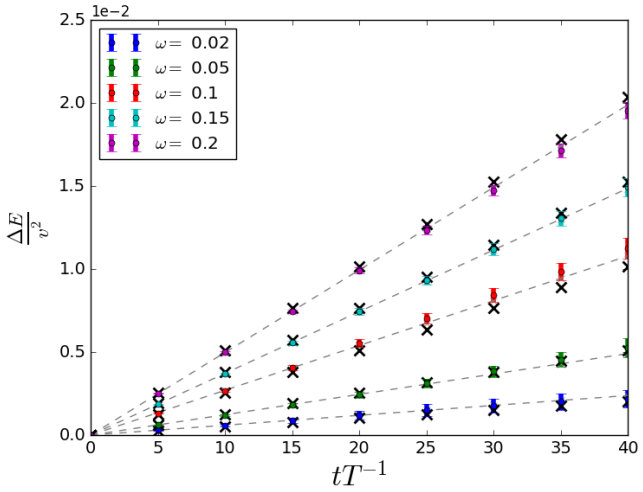

Figure 11.1: **(Single-site Drive)** Absorption of energy, ΔE, is linearly dependent on t. Points are data measured every five periods, black $\times$s are the result of first order perturbation theory, and dashed lines are fits to the data. Drive strength $v = 10^{-4}$, disorder strength $W = 2$, 5×10^5 disorder realisations. We see that the predictions from perturbation theory closely agree with the numerics. We also note that the linear response regime lasts for many periods.

values of ω. We also show that the heating rate in this regime is proportional to the square of the amplitude of the drive. Additionally, we see the long-time behaviour follows as expected from the Rabi picture of two-level systems. As mentioned in the previous chapter, where both the locally and globally driven systems show similar behaviour, we generally refrain from presenting data for both cases.

Here we will characterise the response of these systems in the regime where our above analysis applies. We begin with time-dependence of the energy absorption, $\Delta E\,(t)$. From Fig. 11.1, we see that this absorption is linear in time over many periods. We have also plotted predictions from time-dependent perturbation theory. In Fig. 11.1, the solid curves corresponding to ΔE from time-perturbation theory have a single fitting parameter which is frequency-independent and arises from a factor of the correlation length. We choose to fit this value rather than pick a prescription for ξ which would depend on the strength of the disorder. These results show very good agreement with the absorption from numerical simulations.

Now we focus on the rate of heating. First, we verify that the heating rate is

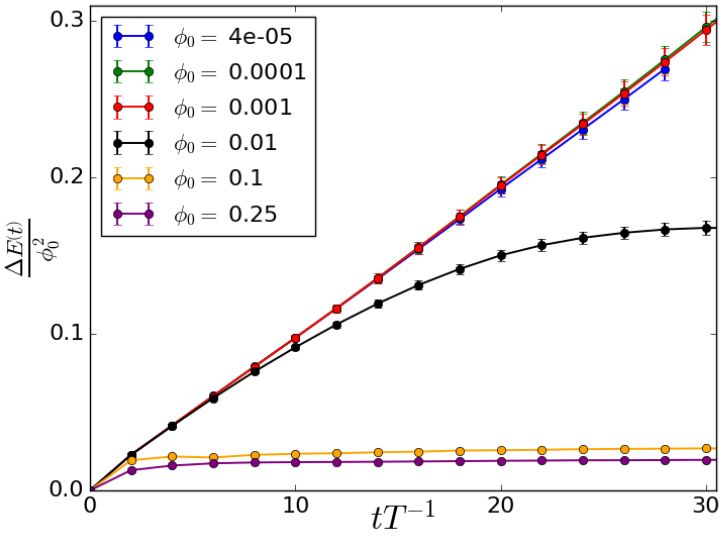

Figure 11.2: **(Global Drive)** Absorption of energy, ΔE, is linear in time at short times and saturates at long times. We see that for a wide range of ϕ_0, the heating rate is proportional to ϕ_0^2. At fixed ω, ϕ_0 determines the strength of the applied field via $\mathcal{E} = \phi_0\omega$. Points are data measured every two periods, lines are visual guides. Frequency $\omega = 0.25$, disorder strength $W = 5$, $\sim 10^5$ disorder realisations.

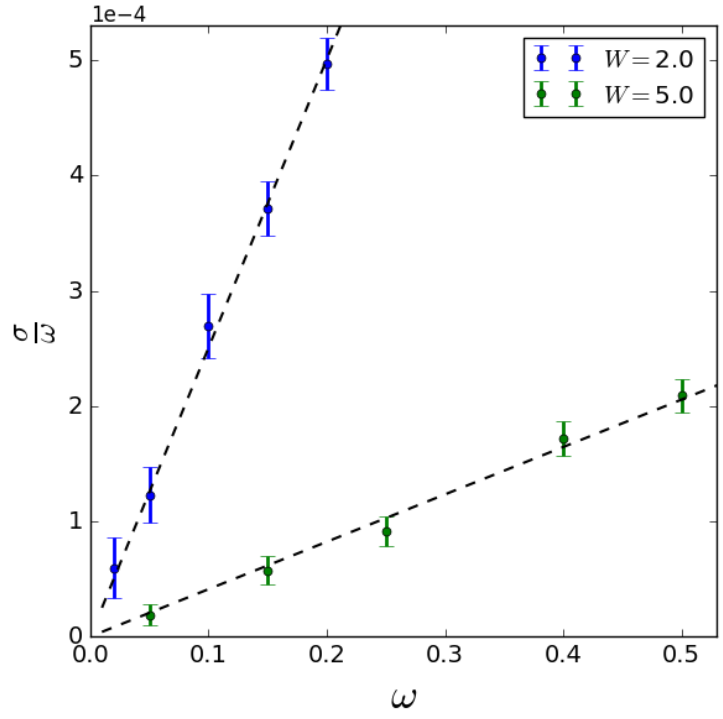

Figure 11.3: **(Single-site Drive)** Frequency dependence of the heating rate for the single-site drive agrees with the modified Mott prediction of ω^2. Drive strength is $v = 10^{-4}$ and averaging is over $\sim 5 \times 10^5$ disorder realisations.

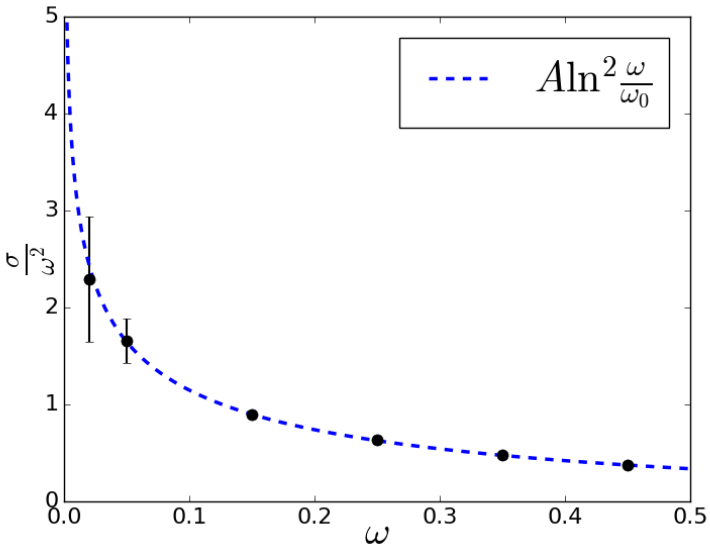

Figure 11.4: **(Global Drive)** AC conductivity is extracted from the heating rate and agrees with the leading frequency dependence of the Mott prediction, $\sigma(\omega) \sim \omega^2 \ln^2 \omega$. Drive strength is $\phi_0 = 10^{-4}$, disorder strength is $W = 5$, averaging is over $\sim 5 \times 10^5$ disorder realisations. The fitting parameters have values $A \approx 0.1$, $\omega_0 \approx 3.3$.

proportional to the square of the driving strength. In Fig. 11.2, we demonstrate that there is a wide range of driving strengths for which the rate of absorption is directly proportional to ϕ_0^2. Note that the vertical axis is ΔE divided by ϕ_0^2 and the curves have nearly the same slope when they are linearly dependent on time.

Next we turn to the frequency dependence (in the global drive case, we can extract the Mott conductivity). For the single-site drive, we expect a simple proportionality, $\sim \omega^2$, which can be seen in Fig. 11.3. For the global drive, we also see good agreement with the Mott law, $\sigma(\omega) \sim \omega^2 \ln^2 \omega$ from Fig. 11.4. Note that we have computed the frequency dependence directly from the dynamics of the systems. This is different from the usual approach which assumes the applicability of linear response theory and uses the Kubo formula.

We now examine the change in occupation, $\delta n(\epsilon, t)$, as defined in Eqn. 10.12. In the linear response regime, we expect that the heating is dominated by resonant pairs of states. These states are separated by energy ω. Due to Pauli exclusion,

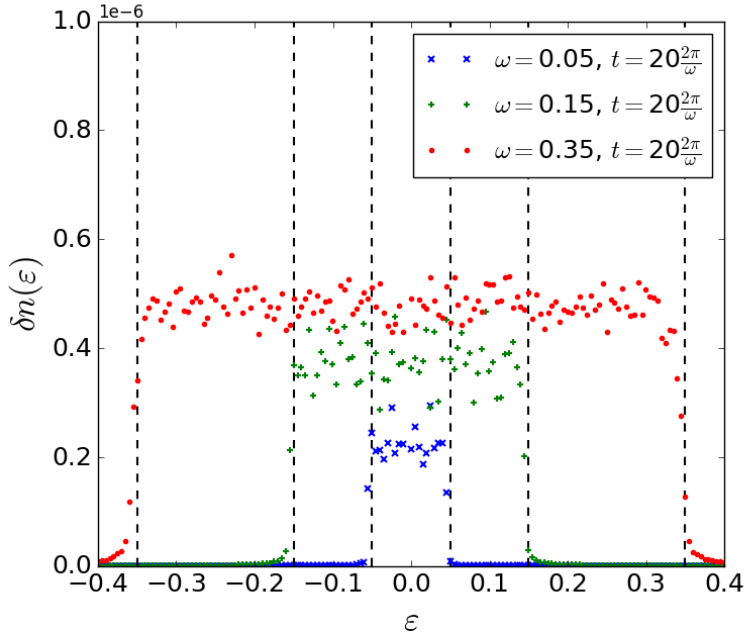

Figure 11.5: **(Global Drive)** Displaced occupation, $\delta n\left(\epsilon, t\right)$, as defined in Eqn. 10.12, shows quantised response. Recall that $\delta n\left(\epsilon, t\right) = n\left(\epsilon, t\right)$ for $\epsilon > 0$ and $\delta n\left(\epsilon, t\right) = 1 - n\left(\epsilon, t\right)$ for $\epsilon < 0$. Steps of width ω are present for a wide range of driving frequencies. Drive strength is $\phi_0 = 10^{-4}$, disorder strength is $W = 5$, over 5×10^5 disorder realisations. This indicates that the primary mechanism of heating is the exciting of particles that comprise resonant pairs which have splitting ω.

only occupied states within ω of the Fermi energy can be excited. In the occupation, therefore, we expect a depletion of states with $-\omega < \epsilon < 0$ and an excess occupation of states with $0 < \epsilon < \omega$ if the resonant pairs are being excited. In Fig. 11.5, we see clear steps. These represent depletion when $-\omega < \epsilon < 0$ and excitation when $0 < \epsilon < \omega$. This physically corresponds to the idea that resonant pairs of splitting ω are dominant contributions and occupied states within ω of the Fermi energy are being excited. We expect further steps of width ω for higher-order processes. These higher-order processes become more prominent when we move away from the weak driving limit.

Given that we expect resonant pairs to dominate, it would be reasonable to assume rare disorder realisations with very-near-resonant pairs contribute strongly and most realisations contribute far less to the absorption. In Fig. 11.6, we plot the absorption

as a function of time for many disorder realisations. We can immediately see that many contribute orders of magnitude less than the few rare, dominant realisations. The inset shows a histogram of the realisations based on the absorption in the long-time limit. This histogram is meant to be illustrative of the fact that there is a long tail here due to the rare resonant pairs that dominate the heating.

The dominant realisations are expected to determine the long-time behaviour of absorption from the Rabi picture. In particular, we expect that ΔE should be proportional to a single power of drive strength from Eq. 11.18, rather than the square of drive strength. In Fig. 11.7, we can see that this is valid for a range of electric field strengths and frequencies.

We will delay discussing the duration of this regime, the crossover to the long-time limit, and other regimes until after the next chapter. In this section, we have presented numerical support for the existence of the linear response regime and have identified key physical aspects of the regime in the numerics. This includes the absorption of energy at a steady rate over a long duration, the Mott form of the a.c. conductivity, and the mechanism of resonant pairs as the key means of heating.

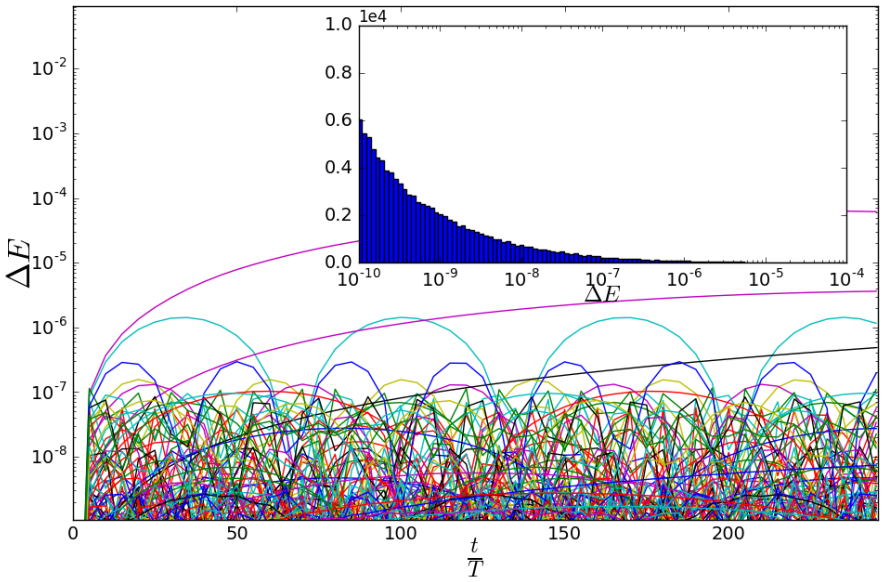

Figure 11.6: **(Single-site Drive)** Absorption of energy shown for individual disorder realisations. Inset: Histogram (over disorder realisations) of energy absorbed in long-time limit. Drive strength is $v = 10^{-2}$, frequency is $\omega = 0.1$, disorder strength is $W = 5$, and we consider 10^4 disorder realisations. There is a long tail in the distribution of energy absorption, which one can see qualitatively in the plot of absorption for many disorder realisations. Most realisations contribute orders of magnitude less than the few rare realisations.

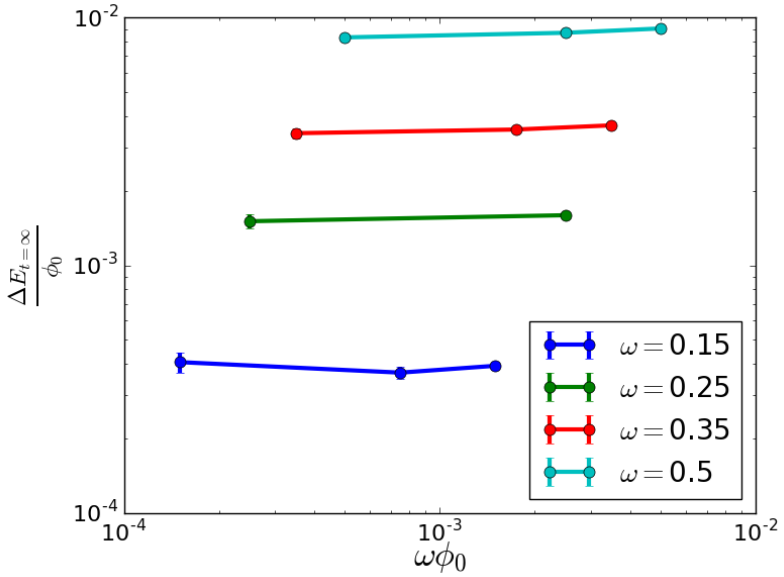

Figure 11.7: **(Global Drive)** Absorption of energy in $t \to \infty$ limit divided by drive strength ϕ_0 is roughly constant as a function of $\omega\phi_0$; lines are visual guide. We expect this proportionality on the field strength from analysing the long-time limit in an ensemble of Rabi problems.

Chapter 12

Strong Driving and Long Times

We now turn to the behaviour of Anderson insulators in the regime of strong driving and long times. To discuss this, we will construct the unitary time-evolution operator for a period, the Floquet operator, $U(T)$, using ideas from the Landau-Zener problem [101].

Generically, we expect to induce avoided energy level crossings in the instantaneous energy levels of $\mathcal{H}(t)$, one of the Floquet-Anderson insulator Hamiltonians in Sec. 10.2, subject to driving. In Fig. 12.1, we plot these energy levels of $\mathcal{H}_{SSD}(t)$ for a half-cycle of the drive to illustrate the type of "spaghetti diagram" that we have in mind.

Within these spaghetti diagrams of the energy levels, we can see many avoided crossings. Our aim will be to consider the evolution as a function of time and develop a treatment for the evolution around avoided crossings. We will introduce the idea of adiabaticity and the Landau-Zener formula to treat these avoided crossings, show that we can focus on single crossings, and understand the behaviour of the system by accounting for the relative number of crossings that have varying levels of adiabaticity.

Specifically, in Sec. 12.1, we will study effective two-level problems again and determine criteria for appropriate treatment within the computation of the evolution operator. In Sec. 12.2, we will use the criteria derived to predict the behaviour of these systems at various values of the parameters $\mathcal{E}, \Omega$ and describe several regimes that arise when we consider strong driving, $\mathcal{E} \gtrsim \Omega$. Notably, we justify the consideration of energy level crossings in a pairwise fashion, which yields significant simplification in the Floquet operator. Lastly, in Sec. 12.3, we present results of numerical simulations

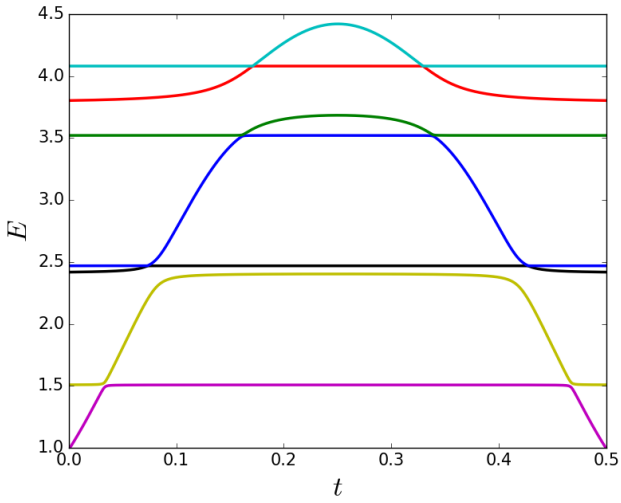

Figure 12.1: **(Single-site Drive)** Evolution of eigenstates under a local driving potential. This qualitatively demonstrates some of the different possibilities for crossings through a half-cycle of the drive. Here we have disorder strength $W = 5$, drive strength $v = 4$, and frequency $\omega = 0.05$

that explore systems at the edge of and just beyond the linear response regime.

12.1 Length Scales and Adiabaticity

We return to the effective two-level problem to be concrete about when the systems can no longer be considered either perturbatively or via the RWA in the Rabi problem. We consider an effective two-level system for localised states based on sites 0 and x,

$$H(t) = \begin{pmatrix} w_0 & \lambda e^{-x/\xi} \\ \lambda e^{-x/\xi} & w_x \end{pmatrix} + \begin{pmatrix} 0 & 0 \\ 0 & V(t) \end{pmatrix}, \tag{12.1}$$

$$V_{SSD}(t) = v \sin(\omega t), \tag{12.2}$$

$$V_{GD}(t) = eE_0 x \sin(\omega t). \tag{12.3}$$

The driving term is small when $v \ll \lambda e^{-x/\xi}$, for the single-site drive, and when $eE_0 x \ll \lambda e^{-x/\xi}$, for the global drive. We now consider these conditions in the continuum picture, and introduce distance in units of the localisation length, $r = x/\xi$.

Recall that $\Delta_\xi = (\rho\xi)^{-1}$ and $\Delta_\xi e^{-r}$ is the effective hopping in the continuum between sites separated by distance $r = x/\xi$. The driving term is small when $v/\xi \ll$

$\Delta_\xi e^{-r}$ in the case of local drive, and $eE_0 r\xi \ll \Delta_\xi e^{-r}$ in the case of uniform electric field. Using these conditions, we can find a length scale, r_L, such that $v/\xi \sim \Delta_\xi e^{-r_L}$ or $eE_0 r_L \xi \sim \Delta_\xi e^{-r_L}$,

$$r_L \equiv \ln\left(\frac{1}{\mathcal{E}}\right), \text{ local drive,} \tag{12.4}$$

$$r_L \equiv Lw\left(\frac{1}{\mathcal{E}}\right), \text{ uniform field,} \tag{12.5}$$

where $Lw\left(g\left(u\right)\right) = u$ for $g\left(u\right) = ue^u$ (Lw is the Lambert-W function) and $\mathcal{E}$ are dimensionless field strengths defined in Chapter 10. The difference between these two conditions, because of the local nature of the drive in the first case, will lead to some differences in the eventual discussion of regimes. Notably, we will see this difference when examining the extent of this regime numerically.

If we can use time-dependent perturbation theory, that is, if $r \ll r_L$, then the two-level problems that contribute most strongly are those which are on-resonance. This requires the energy splitting of the states to be $\hbar\omega$. This implies that sites separated by r_{Mott} (which is defined again below for convenience)

$$r_{\text{Mott}} = \ln\left(\frac{1}{\Omega}\right), \tag{12.6}$$

lead to the dominant contributions to transitions; it was these considerations that led us to the Mott conductivity earlier.

When the distance between two sites is large enough, the driving can no longer be considered perturbatively as the off-diagonal elements in the two-level problem are of the same order or smaller than the driving term. Instead, we need another method for discussing these effective two-level problems.

One approach would be to use higher orders in time-dependent perturbation theory. In this regime, we would expect to see multiple-quanta processes and absorption quantised in steps of width that is a multiple, $n\omega$, corresponding to nth order perturbation theory. We will investigate this possibility numerically and will see clear evidence for the higher-order absorption processes. However, this will break down when the driving becomes strong enough.

12.1.1 Adiabaticity and Landau-Zener Crossings

To provide a framework for discussion of behaviour at strong driving, we now turn to another aspect of evolution for effective two-level problems. In particular, we introduce the idea of adiabatic evolution. Adiabatic processes in a thermodynamic context refer to the absence of exchange of heat or matter between a system and its environment. In quantum mechanics, adiabaticity refers to the notion of remaining in an instantaneous eigenstate of a Hamiltonian which depends on a parameter (e.g. time) as that parameter changes. The criterion for such adiabatic evolution was originally given by Born and Fock [102] and can be stated

$$\hbar \frac{|\langle \alpha | \partial \mathcal{H} / \partial t | \sigma \rangle|}{\left(\epsilon_\alpha - \epsilon_\sigma\right)^2} \ll 1, \tag{12.7}$$

for eigenstates $|\alpha\rangle, |\sigma\rangle$ of $\mathcal{H}(t)$. In the opposite limit, this evolution is sudden and one expects that the evolution has non-zero matrix elements which take an initial state $|\sigma\rangle$ to $|\alpha\rangle$.

The Landau-Zener [101] formula addresses a two-level model of an energy crossing away from the sudden or adiabatic limits. It assumes that the difference between the two energy levels is linear in time and is solvable for arbitrary rate of change, so the Landau-Zener formula can interpolate between the sudden and adiabatic limits. Specifically, consider a two-level problem of the following form

$$\mathcal{H} = \begin{pmatrix} -\alpha t/2 & a \\ a & \alpha t/2 \end{pmatrix}. \tag{12.8}$$

The Landau-Zener formula states that the probability of a diabatic crossing is $P = e^{-2\pi\Gamma}$, $\Gamma = \frac{a^2}{\hbar|\alpha|}$. In other words, if $2\pi a^2 \ll \hbar\alpha$, this crossing is diabatic and if $2\pi a^2 \gg \hbar\alpha$, the crossing is adiabatic.

Using the Landau-Zener approach, we classify all the effective two-level problems as being diabatic, intermediate, or adiabatic. The diabatic crossings are not important to the dynamics of the problem. The adiabatic crossings do not have any net effect over the course of an entire period, but as we will see, they have a significant effect on the transport within a drive cycle, even at long times. The intermediate crossings lead to additional heating and provide a means for the system to thermalise.

Translating our two models into the Landau-Zener framework gives the following values for α

$$\alpha = \omega v, \text{ local drive,} \tag{12.9}$$

$$\alpha = eE_0\omega, \text{ uniform field.} \tag{12.10}$$

We use the condition $2\pi a^2 \sim \hbar\alpha$ to determine the condition for crossings to be intermediate, where here $a = \Delta_\xi e^{-r}$. This leads to another length scale for the two-level picture, r_c. When $r \ll r_c$, a crossing is adiabatic and when $r \gg r_c$, it is diabatic. Only crossings with $r \sim r_c$ are intermediate in nature. For the two models, r_c is given as below

$$r_c = \frac{1}{2}\ln\left(\frac{2\pi}{\Omega\mathcal{E}}\right), \text{ local drive,} \tag{12.11}$$

$$r_c = \frac{1}{2}Lw\left(\frac{4\pi}{\Omega\mathcal{E}}\right), \text{ uniform field.} \tag{12.12}$$

At this stage, there are three dimensionless length scales in the problem. The relationships between these length scales give an indication of what kind of treatment is necessary and what behaviour to expect. In Fig. 12.2, all three length scales are shown. We note that the details depend on the model, but the consistent picture includes a region where crossings are perturbatively described, a region where perturbation theory breaks down, and a region in which crossings are adiabatic and tractable with the Landau-Zener approach. In the next section, we will provide justification for considering crossings in a pairwise fashion, which allows dramatic conceptual simplification in constructing the Floquet operator.

12.2 Strong Driving Regimes

Once we have the criterion for determining the nature of each crossing, we count the number of such crossings and determine regimes of behaviour. We also show that the crossings are well isolated from each other, allowing us to use the Landau-Zener formalism.

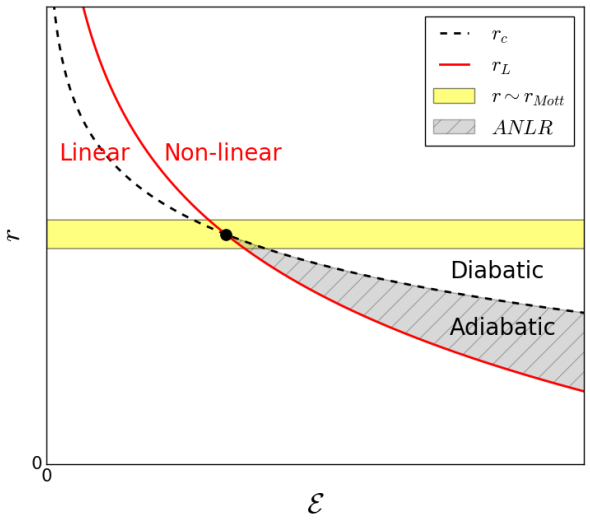

Figure 12.2: Schematic plot showing length scales for effective two-level problems. When $r < r_L$, crossings are tractable with perturbation theory. When $r < r_c$, crossings are adiabatic. The yellow band around r_{Mott} denotes the length scale for resonances. This length scale varies for local drive and uniform field, but not significantly.

The number of intermediate crossings is given by requiring the separation to be within one localisation length of r_c. Thus we have

$$N_{int} = 4\rho\xi v = 4\mathcal{E}, \text{ local drive,} \tag{12.13}$$

$$N_{int} = 4\rho\xi eE_0 \left(r_c\xi\right) = 4\mathcal{E}r_c, \text{ uniform field.} \tag{12.14}$$

The adiabatic crossings are found by integrating separations from those which are first amenable to Landau-Zener treatment ($r > r_L$) to those with separation r_c.

$$N_{ad} = 4\rho\xi v \left(r_c - r_L\right) = 4\mathcal{E}\left(r_c - r_L\right), \text{ local drive,} \tag{12.15}$$

$$N_{ad} = 4\rho \int_{\xi r_L}^{\xi r_c} eE_0 x \mathrm{d}x = 2\mathcal{E}\left(r_c^2 - r_L^2\right), \text{ uniform field.} \tag{12.16}$$

Furthermore, we can estimate the proportion of the driving period that elapses for adiabatic and intermediate crossings. The fraction of the driving period that all the intermediate crossings makes up is proportional to the number of intermediate crossings, N_{int}, multiplied by the time elapsed per crossing, $\frac{\Delta_\xi e^{-r}}{v}$ for the local drive, or $\frac{\Delta_\xi e^{-r}}{eE_0 r_c \xi}$ for the uniform field. For both, the total fraction of the period taken up

Number of crossings	Heating regime
$N_{int} \ll 1, N_{ad} \ll 1$	perturbative non-linear
$N_{int} \ll 1, N_{ad} \gg 1$	adiabatic non-linear
$N_{int} \gg 1, N_{ad} \gg 1$	enhanced dissipation

Table 12.1: Three strong driving ($\mathcal{E} \gtrsim \Omega$) regimes.

by intermediate crossings is then $\propto e^{-r_c}$. As long as r_c is large, this fraction is small and we can consider the intermediate crossings well separated from each other. We therefore have justification for treating the system as a composition of two-level problems.

To describe the dynamics of the system, we consider the possibilities for the number of intermediate and adiabatic crossings. There are three regimes possible for these quantities when considering strong driving, $\mathcal{E} \gtrsim \Omega$. These possibilities are denoted in Table 12.1.

The behaviour in the system varies significantly for the three regimes described. The perturbative non-linear regime can, as in the case of the local driving potential, be understood via higher orders in perturbation theory and with the physical picture of higher quanta absorption. The enhanced dissipative regime leads to systems in which the Floquet modes are delocalised over position-space and energy-space in the limit of long times.

The adiabatic non-linear regime, however, is highly unconventional. For example, consider a system that consists of a single particle initially in an eigenstate of the undriven Hamiltonian. This particle will be driven through many adiabatic crossings that each result in displacements on the order of r_c. Stroboscopically, this will not result in any net displacement, but over a half cycle, one expects a displacement $\propto r_c\sqrt{N_{ad}}$.

For a local potential, this effect is especially dramatic. In Fig. 12.1, we show an example of the time evolution of eigenvalues and crossings. Adjacent energy level crossings typically involve two states, each localised on a different site. These sites are generically distributed uniformly throughout the system. Therefore, we expect

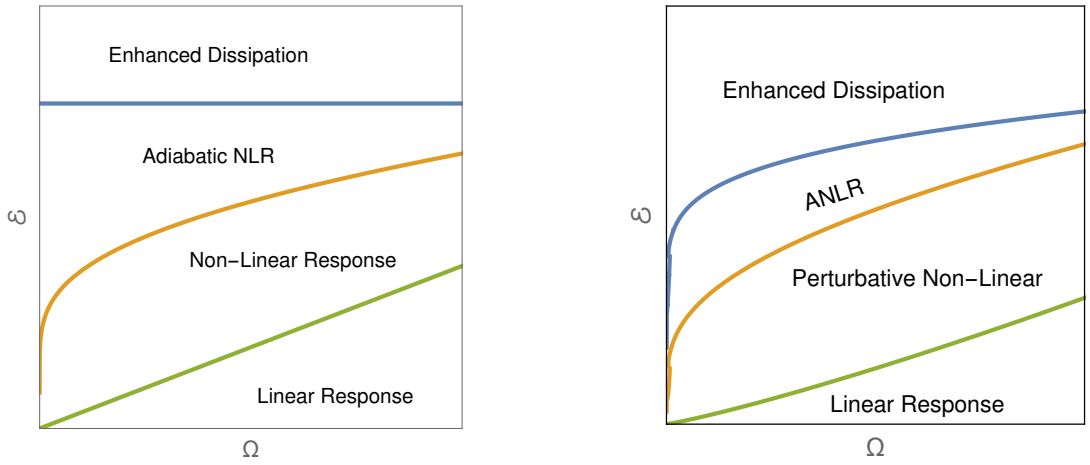

Figure 12.3: Schematic diagrams of dynamical regimes: (left) local driving potential; (right) uniform electric field.

non-local rearrangements of charge. These rearrangements are periodic in the long-time limit and occur over a distance of r_c. In a localised system, one might have expected that driving on a single site can only lead to small disturbances around the localisation site. In the adiabatic non-linear regime, however, we expect a localised state driven through a near-adiabatic crossing to result in a transfer of charge over a distance r_c to another localised state.

The boundaries for these regimes can be derived using the conditions $N_{ad} \sim 1$ and $N_{int} \sim 1$. These regimes are shown in Fig. 12.3. As with the discussion of length scales above, there are differences between the cases of the local potential and the uniform electric field. However, each model has the four regimes that we have described above.

12.3 Numerical Results

We now turn to the numerical results for systems beyond the linear response regime that we have previously addressed. We start by investigating the extent of the linear response regime with respect to the strength of the applied driving. Specifically, we explore boundary of this regime and show that is in good agreement with the predictions above. We then turn to evidence for the non-linear response regimes.

In particular, we demonstrate the breakdown of linear response and study observables that support the descriptions above of the adiabatic non-linear and dissipative regimes.

12.3.1 Breakdown of Linear Response

To better understand the long-time behaviour of these systems, we start by investigating the longevity of the linear response regime. In Fig. 12.4, we demonstrate how $t^\star$ is extracted. In particular, we consider the saturation time, $t^\star$, in units of the period, T, as extracted from the heating rate and the long-time limit of absorption. If the heating is given by $\Delta E = kt$ initially and the long-time limit of the heating is given by constant $\Delta E^\star$, then $t^\star = \frac{\Delta E^\star}{k}$. We must have $t^\star \gg T$ if the linear response regime is to be noticeable when measuring stroboscopically at multiples of the period.

From the discussion in Sec. 12.1 and Sec. 12.2, we have conditions for the applicability of first-order perturbation theory and linear response. In particular, when written in terms of the parameters in our numerics,

$$r_{\text{Mott}} \ll r_L \Longrightarrow \frac{v}{\omega} \ll 1, \text{ local drive,} \tag{12.17}$$

$$r_{\text{Mott}} \ll r_L \Longrightarrow \phi_0 \ln\left(\frac{2W}{\omega}\right) \ll 1, \text{ global drive.} \tag{12.18}$$

When the parameter values (v, ω) or (ϕ_0, ω) obey the above, we expect the linear response regime to be long-lived and the saturation time, $t^\star$, should be many multiples of the period. In Fig. 12.5 and Fig. 12.6, we see that $t^\star$ shows the expected behaviour over several decades of v/ω and $\phi_0 \ln\left(\frac{2W}{\omega}\right)$. We see that when the quantities v/ω and $\phi_0 \ln\left(\frac{2W}{\omega}\right)$ reach $\mathcal{O}(1)$, $t^\star$ is only a few periods at most, so the linear response regime is short-lived. For the global drive, the line of best fit predicts a value of less than one period for $t^\star$ when $\phi_0 \ln\left(\frac{2W}{\omega}\right) = 1$. For the single-site drive, $t^\star$ is just a few periods when $v/\omega = 1$.

As mentioned in Sec. 12.1 and Sec. 12.2, we expect a regime with heating from higher-order processes in perturbation theory that would be characterised, for example, by further quantised "steps" in the change in occupation, $\delta n(\epsilon, t)$ that we

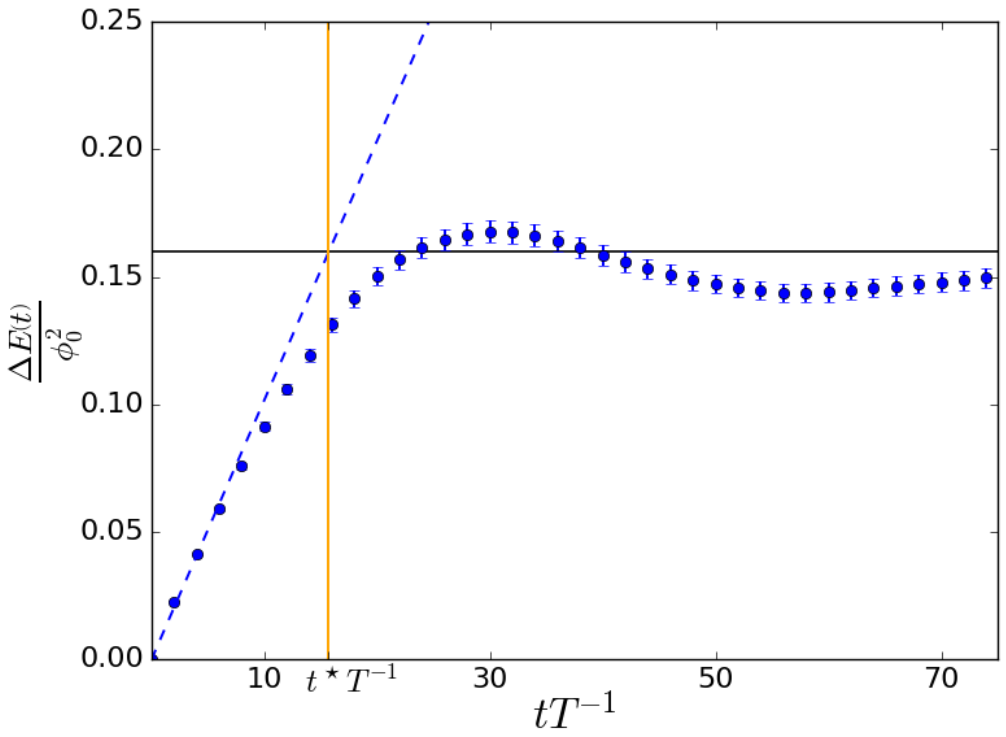

Figure 12.4: **(Global Drive)** Plot of stroboscopic energy absorption (points), diagonal approximation (solid), fit to linear response regime of absorption (dashed). We use the fit to the linear response regime and the long-time limit to extract $t^\star$. Here drive strength is $\phi_0 = 0.01$, frequency is $\omega = 0.25$, disorder strength is $W = 5$, and we consider 7.5×10^4 disorder realisations.

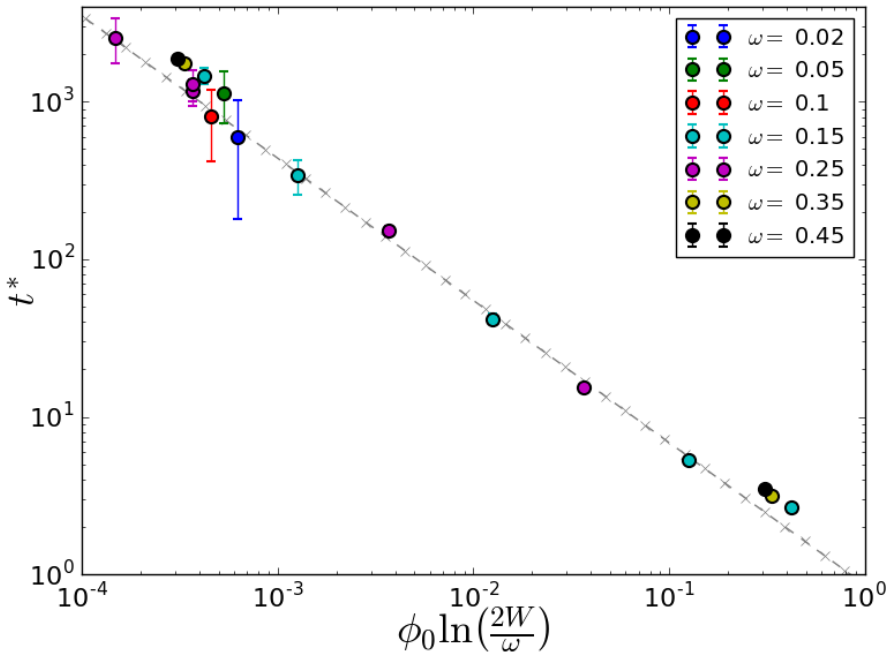

Figure 12.5: **(Global Drive)** $t^\star$ extracted for global drive (t in units of the period, T). There is a collapse of the data when $t^\star$ is plotted against $\phi_0 \ln\left(\frac{2W}{\omega}\right)$. $t^\star$ indicates the extent of the linear response regime for a given choice of ϕ_0, ω.

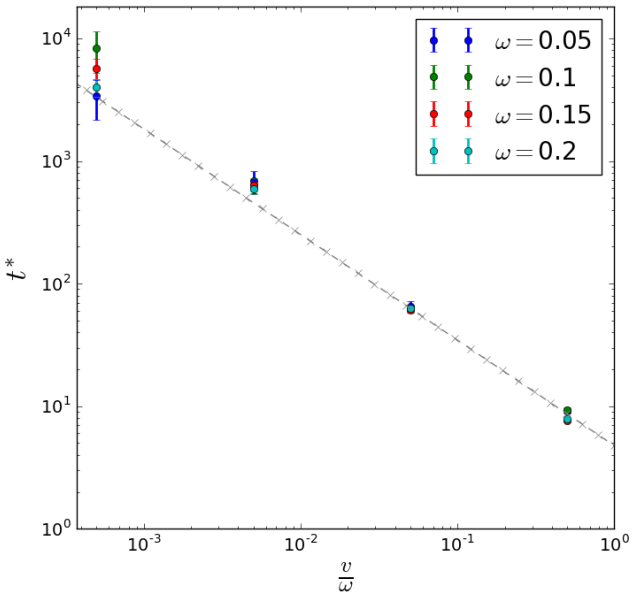

Figure 12.6: **(Single-site Drive)** $t^\star$ extracted for single-site drive (t in units of the period, T). There is a collapse when $t^\star$ is plotted against v/ω. When $t^\star \sim 1$, this indicates the boundary of the linear response regime with respect to v/ω.

considered in Chapter 11. In Fig. 12.7, we can see the presence of these higher order terms. The development of these steps indicates a breakdown of linear response theory. However, this breakdown is conceptually simple and easy to understand in terms of multiphoton absorption and emission processes.

12.3.2 Sample-to-sample and Site-to-site Fluctuations

From the analysis of the linear response regime in terms of resonant pairs and the Rabi problem, we expect that as the system is driven at amplitudes beyond the linear response regime, disorder realisations will contribute more equitably. To quantify this, we consider the ratio of the mean (across different realisations) energy absorbed at long-times to the root-mean-square (again over realisations) energy absorbed,

$$F \equiv \frac{(\Delta E)_{mean}}{(\Delta E)_{RMS}}. \tag{12.19}$$

In the linear-response regime, we expect that fluctuations in the energy absorbed across realisations will be large and the ratio will be small. When this ratio, F, is

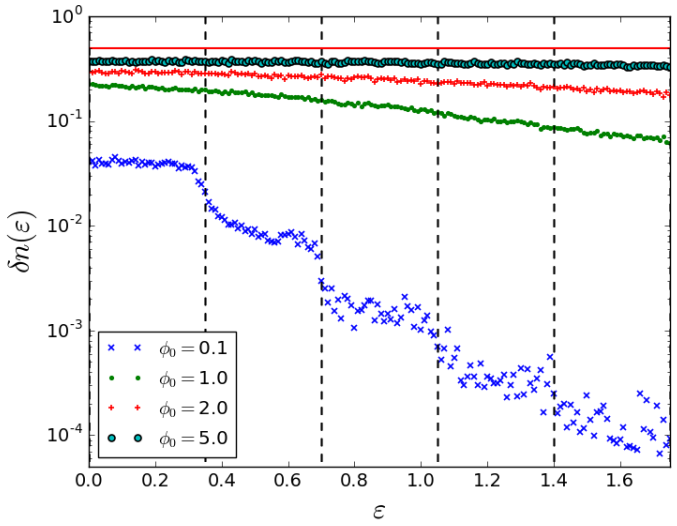

Figure 12.7: **(Global Drive)** Displaced occupation, $\delta n\,(\epsilon, t)$, as defined in Eqn. 10.12, in the long-time limit. This shows quantised response in multiple steps of width ω for driving $\phi_0 = 0.1$ and frequency $\omega = 0.35$. At stronger drive strengths, the occupation is clearly inconsistent with the quantised picture of absorption from resonant processes in perturbation theory.

near 1, it means there are no fluctuations in the energy absorption. See Fig. 12.8 for an illustration of this ratio. We also note that this switch-on behaviour occurs for $v/\omega \approx 1$. We also point out that in the range $\frac{v}{\omega} \leq 10^{-1}$, the value of F is proportional to ω. Considering the ratio, F, for the global drive is problematic because this quantity is self-averaging for large enough systems.

12.3.3 System Activity

We now introduce a new measure because of the failure of F for the global drive. This new measure also gives further insight on the mechanisms for heating. In the Mott-response regime, resonant pairs become excited. These pairs comprise only a small number of sites in the system. Systems in the strong-driving regime have more sites involved in the heating mechanism because of the types of crossings we have described

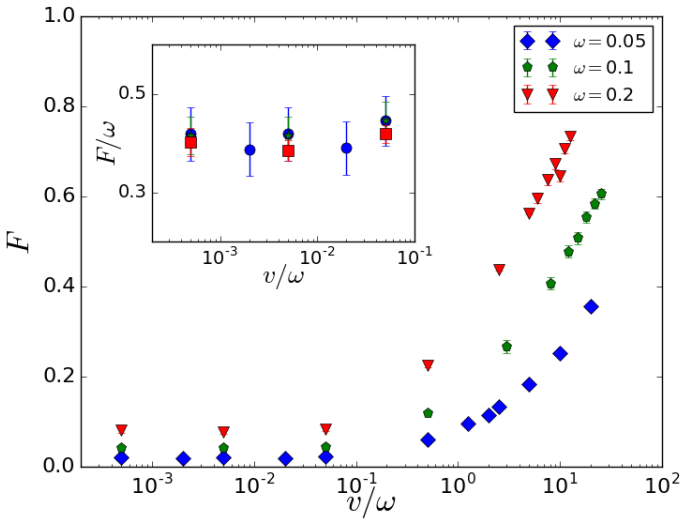

Figure 12.8: **(Single-site Drive)** Plot of the ratio between mean energy absorption to root-mean-square absorption at long times. This shows steep crossover behaviour beyond the linear response regime. This indicates that more heating is driven by all disorder realisations and less by the rare realisations with resonant pairs of states.

above. To see that systems are more active upon stronger driving, we consider

$$\overline{R} = \frac{\langle (\delta n)^2 \rangle_{\text{disorder,position}}}{\langle (\delta n)^4 \rangle^{1/2}_{\text{disorder,position}}}, \tag{12.20}$$

$$\delta n = n(x, t = \infty) - n(x, 0), \tag{12.21}$$

where $n\,(x,t)$ is the average occupation at position x. The average is over both disorder realisations and position. This ratio characterises the fraction of the system that has significant change in occupation. In the Mott-response regime, we expect only resonant pairs will be active. This leads to a small value for the ratio. For strong driving, the system is more uniformly active and so this ratio increases towards one. In Fig. 12.9, we see from the numerics that this expectation is met.

In fact, as a function of $\phi_0\omega$, the active ratio of the sample dramatically increases when driving strengths are large enough to push the system beyond the linear response regime. From this, we conclude that systems become more uniformly active in position-space than in the weak driving regime (where only resonant pairs experienced significant fluctuations).

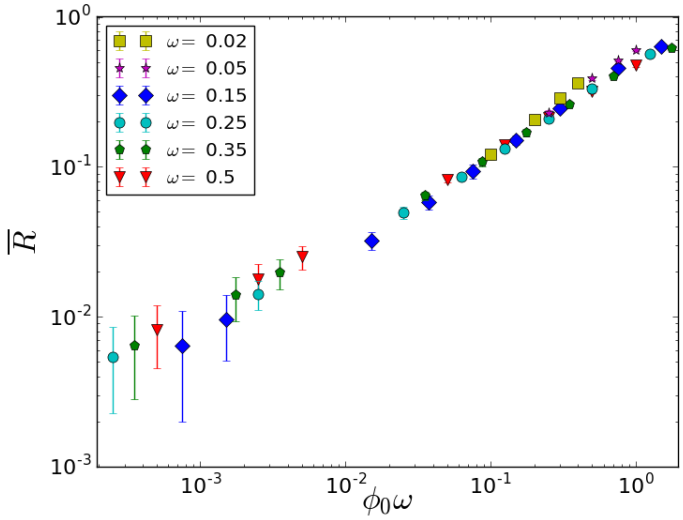

Figure 12.9: **(Global Drive)** We plot $\overline{R}$ for several frequencies over a wide range of $\phi_0\omega$. As this quantity increases, it indicates that the long-time change in occupation throughout the system is becoming more uniform.

12.3.4 Adiabaticity

To identify the adiabatic non-linear response regime, we introduce additional observables. We will attempt to measure the adiabaticity of crossings directly for these systems. In particular, we are interested in the behaviour of the systems within the drive period. In this subsection, we introduce two measures that quantify the proportions of sudden, adiabatic, and intermediate energy level crossings.

We imagine the spaghetti diagrams for the single-site drive model, or the global drive model with the electric field represented using a scalar potential. Over an entire drive period, we expect many avoided energy level crossings. The crossings which are traversed suddenly or adiabatically both effectively "un-do" themselves over a period, but they have different consequences within the period.

To probe the presence of both diabatic and adiabatic crossings, we consider the evolution of single energy eigenstates through a full period. In the strongly-localised regime, when a single particle starts in an eigenstate $|m\,(0)\rangle$, localised at r_m, we consider two extreme limits for traversing an avoided energy level crossing with instan-

taneous eigenstate $|n(t)\rangle$ at time t. Note that we label the instantaneous eigenstates in order by increasing instantaneous energy eigenvalue.

If the avoided crossing is traversed suddenly, the particle remains in the instantaneous eigenstate, still localised at r_m. At the other extreme, if the crossing is traversed adiabatically, then the state of the particle evolves into $|n(t)\rangle$, localised at some other position, r_n. Finally, if the crossing is neither sudden nor adiabatic, we expect that the particle will evolve into a superposition of the two instantaneous eigenstates involved.

Within the drive period, in the limit of only sudden or adiabatic crossings, we expect the time-evolution operator to be a permutation matrix in the basis of the instantaneous eigenstates multiplied by a diagonal phase matrix. For time-evolution which includes intermediate crossings, we will generically expect weight on more than one instantaneous eigenstate.

To investigate these possibilities concretely, we will study the following observables

$$f(t) \equiv \frac{1}{L} \sum_m \mathcal{O}_m(t), \tag{12.22}$$

$$g(t) \equiv \frac{1}{L} \sum_m \max_n \{|\langle n(t) \mid U(t,0) \mid m(0)\rangle|^2\}, \tag{12.23}$$

$$\mathcal{O}_m(t) \equiv |\langle m(t) | U(t,0) | m(0)\rangle|^2. \tag{12.24}$$

$\mathcal{O}_m(t)$ is the probability of finding a particle which is initially in the state $|m(0)\rangle$ in the instantaneous eigenstate, $|m(t)\rangle$, after evolving through time t. If the time-evolution is perfectly adiabatic, this probability is 1. If the time-evolution from 0 to t includes a crossing which is sudden, this probability is 0 just after the crossing. $f(t)$ is the average of this probability over the instantaneous eigenstates.

In $g(t)$, we can detect the possibility of permutations. In particular, if there is a crossing in the time-evolution between 0 and t which is traversed suddenly,

$$\max_n \{|\langle n(t) \mid U(t,0) \mid m(0)\rangle|^2\} = 1. \tag{12.25}$$

If the evolution is purely sudden or adiabatic, we expect $g(t)$ to remain 1. However, if there are intermediate crossings, $g(t)$ may exhibit a decay away from 1 when

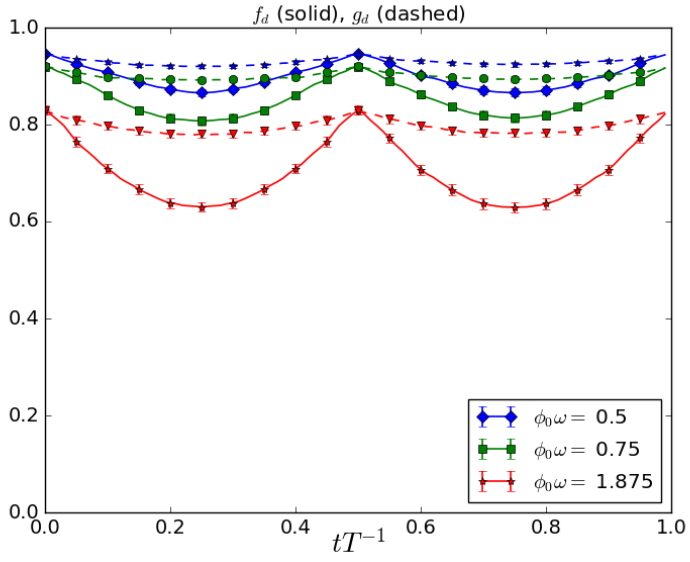

Figure 12.10: **(Global Drive)** We plot $f_d(t), g_d(t)$ as defined in the text for several values of field strength $\phi_0\omega$, frequency $\omega = 2.5 \times 10^{-4}$, and disorder strength $W = 20$. At sufficiently strong driving, the systems include intermediate crossings that prevent ideal revivals. However, $g_d(t)$ remains near the stroboscopic value, indicating that most crossings correspond to evolution that is nearly a permutation matrix.

a state evolves into a superposition of two instantaneous eigenstates.

We will consider these quantities over a full drive period in our systems. We point out that because the periodic drive included has a sinusoidal time-dependence, we expect a system with only sudden or adiabatic crossings will return to its starting state when $t = T/2$. We will consider the long-time limit of $f(t)$ and $g(t)$, denoted by $f_d(t)$ and $g_d(t)$.

In the limit of purely sudden or adiabatic crossings, we expect $f_d(t)$ to decay significantly from 1 during the time-evolution for $0 < t \mod T < T/2$. However, in the finite systems we consider, there are very few crossings at weak drive. In this limit, we expect $g_d(t)$ will remain 1. When there are intermediate crossings, though, $g_d(t), f_d(t)$ decay from values less than 1. However, if $g_d(t)$ remains $\mathcal{O}(1)$, we can infer that the intermediate crossings are near-adiabatic.

Now we review the scheme for computing the time-evolution of these quantities and then briefly present some results from numerical simulations. We recall the

expression from Chapter 9 for time-evolution of the expectation of an observable, $\hat{o}(t)$, with initial state, $|\psi_0\rangle$.

$$\langle\psi_0|\hat{o}(nT+s)|\psi_0\rangle = \sum_{\alpha,\beta} e^{i\left(\epsilon_\alpha-\epsilon_\beta\right)nT}\langle\varphi_\alpha|U^\dagger(s)\,\hat{o}(t)\,U(s)|\varphi_\beta\rangle\langle\psi_0 \mid \varphi_\alpha\rangle\langle\varphi_\beta \mid \psi_0\rangle, \tag{12.26}$$

where $|\varphi_\alpha\rangle$ are the eigenstates of the Floquet unitary, $U(T)$, and $s \in [0,T)$. We can pick $\hat{o}(t) = |m(t)\rangle\langle m(t)|$ where $|m(t)\rangle$ is an instantaneous eigenstate of $\mathcal{H}(t)$ and $|\psi_0\rangle = |n(0)\rangle$. We can also compute this in the long-time limit, as discussed in Chapter 9,

$$f_d(t) = \frac{1}{L}\sum_{n,\alpha}|\langle n(t)\,|U(s,0)|\varphi_\alpha\rangle|^2|\langle\varphi_\alpha \mid n(0)\rangle|^2. \tag{12.27}$$

First, in Fig. 12.10, we point out that the dearth of crossings for finite-sized systems accounts for the lack of decay in $f_d(t)$ over a period for weak drives. Then, for increasing values of $\phi_0\omega$, we see a substantial decrease in the quantity $f_d(t)$ during the drive cycle, with the maximal decrease around $t = T/4$. This indicates that there have been many crossings through this part of the drive cycle. However, because $g_d(t)$ varies less strongly than $f_d(t)$ throughout the drive period, the crossings that contribute this decrease are either diabatic or near-adiabatic, as we expect in the non-linear adiabatic regime.

12.4 Outlook and Further Questions

There are several open questions regarding the regimes beyond linear response. Finding a clear, definitive signature of the non-linear adiabatic regime is likely to be difficult because of two compounding issues. First, we predict the regime exists for relatively small driving frequency and relatively large driving amplitude. However, to remain in the universal regime, we also require large disorder strength. These constraints present independent needs for finer discretisation in the calculation of the Floquet operator.

Nonetheless, we can still make observations about behaviour of the systems near the non-linear adiabatic regime. On one hand, if there are only diabatic level crossings,

we would not expect much activity within the system as states which are occupied remain spatially localised throughout the driving. On the other hand, if we have near-adiabatic crossings, it is possible there will be some displacement of particles within the system through the period. By measuring observables within the drive period, one can probe this movement of charge. More concretely, current measured within the drive period should develop fluctuations in the non-linear adiabatic regime.

In this section, we have presented evidence indicating the breakdown of linear response at long times and strong driving. We have identified the boundary of the linear response regime in numerical simulations and checked that it matches the predictions given in Sec. 12.1. Additionally, we have observed the perturbative non-linearities contributed from multiphoton processes. Lastly, we have proposed some observables for characterising the non-linear adiabatic regime more carefully and presented an illustrative example of one of these quantities in that regime.

Chapter 13

Summary

We have studied periodically driven Anderson insulators with two types of driving. We revisited the Mott argument for the frequency dependence of heating and conductivity. We used numerical simulations to extract the a.c. conductivity $\sigma(\omega) \sim \omega^2 \ln^2 \omega$ for a monochromatic, uniform electric field and the analogous quantity for a single-site drive, $\sigma(\omega) \sim \omega^2$, by studying the dynamical response of the systems directly.

We have also studied periodically driven Anderson insulators beyond linear response. This included both at long times and strong driving. We presented a framework for analysing the time-evolution beyond linear response. We used arguments about adiabaticity and Landau-Zener crossings to make simplifications to the Floquet operator. From this framework, we suggested that there is a variety of behaviour that can exist in the Floquet limit, including systems in the near-adiabatic non-linear response regime which exhibit periodic, non-local rearrangements of charge.

We have provided results from numerical simulations to illustrate the breakdown of linear response and characterise the Floquet regimes. In particular, we have identified the boundary of the linear response regime from numerics. We have shown that the main contributions to heating beyond linear response no longer come from resonant pairs, but instead from multiphoton processes and Landau-Zener avoided energy level crossings. In simulations, we have seen that systems heat up in an active manner when driven beyond linear response and a significant fraction of avoided energy level crossings are traversed near-adiabatically. Lastly, we have made predictions for other observables to characterise the long-time behaviour of the non-linear response regimes and it would be interesting to test these predictions numerically in future work.

Bibliography

[1] D. T. Liu, F. J. Burnell, L. D. C. Jaubert, and J. T. Chalker, Phys. Rev. B **94**, 224413 (2016).

[2] D. T. Liu, V. Khemani, J. T. Chalker, and S. L. Sondhi, in preparation.

[3] F. J. Burnell and J. T. Chalker, Phys. Rev. **92**, 220417 (2015).

[4] A. P. Ramirez, Annu. Rev. Mater. Sci. **24**, 453 (1994).

[5] P. Chandra, B. Doucot, Phys. Rev. B **38**, 9335 (1988).

[6] *Highly Frustrated Magnetism*, edited by C. Lacriox, P. Mendels, and F. Mila (Springer, 2010).

[7] R. Moessner, J. T. Chalker, Phys. Rev. Lett. **80**, 2929 (1998); R. Moessner, J. T. Chalker, Phys. Rev. B **58**, 12049 (1998).

[8] M. Elhajal, et al., J. Phys.: Condens. Matter **16**, S917 (2004).

[9] G. Wannier, Phys. Rev. **79**, 357 (1950).

[10] R. M. F. Houtappel, Physica, **16**, 425 (1950).

[11] J. Stephenson, J. Math. Phys. **5**, 1009 (1964); *ibid.* **11**, 413 (1970).

[12] P. W. Kasteleyn, J. Math. Phys. **4**, 287 (1963).

[13] E. W. Montroll, R. B. Potts, and J. C. Ward, J. Math. Phys. **4**, 308 (1963).

[14] O. A. Petrenko and M. F. Collins, Can. J. Phys. **75**, 605 (1997).

[15] J. Villain, Z. Phys. B **33**, 31 (1979).

[16] L. Balents, Nature **464**, 199 (2010).

[17] C. Castelnovo, R. Moessner, and S. L. Sondhi, Nature **451**, 42-45 (2008).

[18] T. Fennell, S. T. Bramwell, D. F. McMorrow, P. Manuel, Nature Physics **3**, 566 (2007).

[19] L. D. C. Jaubert, P. C. W. Holdsworth, Nature Phys. **5**, 258261 (2009).

[20] S. T. Bramwell, et al., Nature **461**, 956-959 (2009).

[21] S. R. Dunsiger, et al., Phys. Rev. Lett. **107**, 207207 (2011).

[22] S. J. Blundell, Phys. Rev. Lett. **108**, 147601 (2012).

[23] L. Savary, L. Balents, Rep. Prog. Phys. **80**, 016502 (2017).

[24] C. Nayak, S. H. Simon, A. Stern, M. Freedman, and S. D. Sarma, Rev. Mod. Phys. **80**, 1083 (2008).

[25] J. T. Chalker, P. C. W. Holdsworth and E. F. Shender, Phys. Rev. Lett. **68**, 855 (1992).

[26] J. N. Reimers, A. J. Berlinsky, and A.-C. Shi, Phys. Rev. B **43**, 865 (1991).

[27] D. Bergman, J. Alicea, E. Gull, S. Trebst and L. Balents, Nature Phys. **3**, 487 (2007).

[28] E. Rastelli, A. Reatto and A. Tassi, J. Phys C **16**, L331 (1983).

[29] H. W. J. Blöte and H. J. Hilhorst, J. Phys. A **15**, L631 (1982); B. Nienhuis, H. J. Hilhorst, and H. W. Blöte, *ibid.* **17**, 3559 (1984); B. Nienhuis, Phys. Rev. Lett. **49**, 1062 (1982).

[30] C. Zeng and C. L. Henley, Phys. Rev. B **55**, 14935 (1997).

[31] Y. Yamada, K. Kitsuda, S. Nohdo, and N. Ikeda, Phys. Rev. B **62**, 12167 (2000), and J. Phys. Soc. Jpn. **66**, 3733 (1997).

[32] A. J. Hearmon, D. Prabhakaran, H. Nowell, F. Fabrizi, M. J. Gutmann, and P. G. Radaelli, Phys. Rev. B **85**, 014115 (2012).

[33] A. B. Harris, and T. Yildirim, Phys. Rev. B **81**, 134417 (2010). See also erratum: Phys. Rev. B **82**, 029902 (2010).

[34] For a recent review, see: N. Ikeda, T. Nagata, J. Kano, and S. Mori, J. Phys. Cond. Matt. **27**, 053201 (2015).

[35] A. Nagano, M. Naka, J. Nasu, and S. Ishihara, Phys. Rev. Lett. **99**, 217202 (2007); A. Nagano and S. Ishihara, J. Phys. Cond. Matt. **19** (2007) 145263.

[36] D. Auerbach, E. Domany, and J. E. Gubernatis, Phys. Rev. B **37**, 1719 (1988).

[37] D. S. Zimmerman, C. Kallin, and A. J. Berlinsky, Phys. Rev. B **37**, 7766 (1988).

[38] D.-T Hoang and H. T. Diep, Phys. Rev. E **85**, 041107 (2012).

[39] A. Bunker, B. D. Gaulin, and C. Kallin, Phys. Rev. B **48**, 15861 (1993).

[40] S. N. Coppersmith, Phys. Rev. B **32**, 1584 (1985).

[41] D. Blankschtein, M. Ma, A. N. Berker, G. S. Grest, and C. M. Soukoulis, Phys. Rev. B **29**, 5250 (1984).

[42] R. Moessner and S. L. Sondhi, Phys. Rev. B **63**, 224401 (2001).

[43] S. E. Nagler, W. J. L. Buyers, R. L. Armstrong, and B. Briat, Phys. Rev. B **27**, 1784 (1983).

[44] B. Canals and D. A. Garanin, Can. J. Phys, **79**, 1323 (2001).

[45] R.L. Stratonovich, Sov. Phys. Dokl. **2**, 416 (1958); J. Hubbard, Phys. Rev. Letters **3**, 77 (1959).

[46] S.V. Isakov, K. Gregor, R. Moessner and S. L. Sondhi, Phys. Rev. Lett. **93**, 167204 (2004).

[47] M. E. J. Newman and G. T. Barkema, Monte Carlo Methods in Statistical Physics (Oxford University Press, Oxford, 1999).

[48] M. K. Phani, J. L. Lebowitz, and M. H. Kalos, Phys. Rev. B **21**, 4027 (1980).

[49] A. D. Beath and D. H. Ryan, Phys. Rev. B **73**, 174416 (2006).

[50] A. O. Gogolin, A. A. Nersesyan, A. M. Tsvelik, Bosonization and Strongly Correlated Systems (Cambridge University Press, 2004).

[51] P. W. Anderson, Phys. Rev. **109**, 1492 (1958).

[52] J. T. Edwards, D. J. Thouless, J. Phys. C: Solid State Phys., **5**, 1572 (1972).

[53] E. Abrahams, P. W. Anderson, D. C. Licciardello, and T. V. Ramakrishnan, Phys. Rev. Lett. **42**, 673 (1979).

[54] H. Furstenberg, H. Kesten, Ann. Math. Statist. **31**, 457 (1960).

[55] H. Furstenberg, Trans. Amer. Math. Soc. **108**, 377 (1963).

[56] V. I. Oseledec, Trans. Moscow Math. Soc. **19**, 197 (1968).

[57] J. Kemp, University of Oxford, MPhys project (2015).

[58] D. M. Basko, I. L. Aleiner and B. L. Altshuler, Annals of Physics **321**, 1126 (2006).

[59] A. Pal and D. A. Huse, Phys. Rev. B **82**, 174411 (2010).

[60] M. Znidaric, T. Prosen, and P. Prelovsek, Phys. Rev. B **77**, 064426 (2008).

[61] V. Oganesyan and D. A. Huse, Phys. Rev. B **75**, 155111 (2007).

[62] D. A. Huse, R. Nandkishore, and V. Oganesyan, Phys. Rev. B **90**, 174202 (2014).

[63] M. Schreiber, S. S. Hodgman, P. Bordia, H. P. Lüschen, M. H. Fischer, R. Vosk, E. Altman, U. Schneider, and I. Bloch., Science, **349**, 6250 (2015).

[64] T. F. Rosenbaum, R. F. Milligan, M. A. Paalanen, G. A. Thomas, and R. N. Bhatt, Phys. Rev. B **27**, 7509 (1983).

[65] G. Roati, et al., Nature **453**, 895-898 (2008).

[66] M. Kappus, F. Wegner, Z. Phys. B **45**, 15-21 (1981).

[67] G. Czycholl, B. Kramer, A. MacKinnon, Z. Phys. B **43**, 5 (1981).

[68] J. H. Bardarson, F. Pollmann, J. E. Moore, Phys. Rev. Lett. **109**, 017202 (2012).

[69] M.P. Van Albada, A. Lagendijk, Phys. Rev. Lett. **55**, 2692 (1985).

[70] D. S. Wiersma, et al., Nature **390**, 671-673 (1997).

[71] J. Choi, et al., Science **352**, 6293 (2016).

[72] P. Bordia, H. Lschen, U. Schneider, M. Knap, and I. Bloch, Nature Physics **13**, 460464 (2017).

[73] G. Floquet, Ann. Sci. É.N.S. **12**, 47 (1883).

[74] F. Bloch, Z. Phys. **52**, 555 (1928).

[75] Y. Gefen and D. J. Thouless, Phys. Rev. Lett. **59**, 1752 (1987).

[76] D. M. Basko, M. A. Skvortsov, and V. E. Kravtsov, Phys. Rev. Lett. **90**, 096801 (2003).

[77] V. Khemani, R. Nandkishore, and S. L. Sondhi, Nat. Phys. **11**, 560 (2015).

[78] P. A. M. Dirac, Proc. Roy. Soc. A. **114**, 767 (1927);

[79] N. F. Mott, Phil. Mag. **17**, 1259 (1968).

[80] J. P. Joule, Proc. R. Soc. Lond. **4**, 280 (1837).

[81] T. Saso, J. Phys. C: Solid State Phys. **17**, 2905 (1984).

[82] V. Berezinskii, Sov. J. Exp. Th. Phys. **38**, 620 (1974).

[83] M. Wilkinson, J. Phys. A **21**, 4021 (1988).

[84] M. Machida, K. Saito, S. Miyashita, J. Phys. Soc. Jap., **71**, 2427 (2002).

[85] M. Wilkinson, E. J. Austin, J. Phys. A: Math. Gen. **23**, L957 (1990).

[86] D. Cohen, T. Kottos, Phys. Rev. Lett. **85**, 4839 (2000).

[87] S. Gopalakrishnan, M. Muller, V. Khemani, M. Knap, E. Demler, Phys. Rev. B **92**, 104202 (2015).

[88] S. Gopalakrishnan, M. Knap, E. Demler, Phys. Rev. B **94**, 094201 (2016).

[89] J. H. Shirley, Phys. Rev. **138**, B979 (1965).

[90] J. Sakurai, Modern Quantum Mechanics (Addison-Wesley 1994).

[91] M. Reitter, J. Näger, K. Wintersperger, C. Sträter, I. Bloch, A. Eckardt, U. Schneider, arXiv:1706.04819 [cond-mat.quant-gas] (2017).

[92] F. Wilczek, Phys. Rev. Lett. **111**, 250402 (2013).

[93] P. Bruno, Phys. Rev. Lett. **111**, 070402 (2013); H. Watanabe, M. Oshikawa, Phys. Rev. Lett. 114, 251603 (2015).

[94] J. Zhang, et al., Nature **543**, 217-220 (2017).

[95] S. Choi, et al., Nature **543**, 221-225 (2017).

[96] R. E. Peierls, Z. Phys. **80**, 763 (1933).

[97] E. Jones, T. Oliphant, P. Peterson, et al., SciPy: Open source scientific tools for Python, "http://www.scipy.org/" (2001).

[98] A. H. Al-Mohy, N. J. Higham, SIAM J. Mat. Anal. Appl. **3**, 970 (2009).

[99] Bruus, H. and K. Flensberg, Many-Body Quantum Theory in Condensed Matter Physics: An Introduction (Oxford University, Oxford, 2004).

[100] R. Kubo, J. Phys. Soc. Jpn. **12**, 570-586 (1957).

[101] L. Landau, Phys. Z. **2**, 46 (1932); C. Zener, Proc. Roy. Soc. A. **6**, 696 (1932); E. C. G. Stueckelberg, Hel. Phys. Acta. **5**, 369 (1932); E. Majorana, Nuo. Cim. **2** 43 (1932).

[102] M. Born, V. Fock, Z. Phys. **51**, 165 (1928).